Kinoshita, M., Tobin, H., Ashi, J., Kimura, G., Lallemant, S., Screaton, E.J., Curewitz, D., Masago, H., Moe, K.T., and the Expedition 314/315/316 Scientists
Proceedings of the Integrated Ocean Drilling Program, Volume 314/315/316

Expedition 315 Site C0002[1]

Expedition 315 Scientists[2]

Chapter contents

Introduction

Integrated Ocean Drilling Program (IODP) Site C0002 (proposed Site NT3-01B) targeted the uppermost 1400 meters below seafloor (mbsf) at the seaward flank of the Kumano Basin (Figs. F1, F2). The uppermost 1400 m to be drilled during this expedition provides an opportunity to penetrate the Kumano Basin sedimentary sequence and the underlying accretionary prism materials, the nature of which are unknown. Acoustic features characterized by irregular discontinuous horizons of this section suggest that it may be composed of chaotically deformed accretionary wedge sedimentary mélange transported from significantly greater depths. It shows a good contrast with the overlying well-ordered Kumano Basin sediments. This site also provides an opportunity to compare trench-to-basin transition ages on both sides of the outer arc high.

The principal objective during IODP Expedition 315 was to reveal the stratigraphic, physical, structural, and chemical features of materials obtained from the accretionary prism and the overlying forearc basin. An integrated interpretation is proposed based on these findings combined with seismic and log data obtained during IODP Expedition 314. Coring at this site also provides critical pilot hole information for future riser drilling. To achieve the ~6000 m total depth objective using riser and weighted drilling mud involves setting multiple casing strings, with the depth of each depending on the least principal stress, the fracture strength of the formation, and the pore fluid pressure gradient. The key part of this casing plan is the "top-hole" portion, where tolerances on mud weight are tight. Planning the casing program, therefore, requires excellent information on physical properties in the uppermost 1000 m. Additionally, the upper ~50 m of mechanical strength is critically important to the deployment of the riser blowout preventer. In light of this, our strategy is to utilize riserless coring for this section during a future stage of the Nankai Trough Seismogenic Zone Experiment (NanTroSEIZE). Furthermore, downhole (in situ) temperature measurements were conducted as deeply as possible, which will enable estimation of deeper temperatures by extrapolation. These measurements will provide critical information for well planning of the 6 km riser hole and will aid in the design of sensors and telemetry of the long-term borehole observatory planned for a future NanTroSEIZE stage.

[1] Expedition 315 Scientists, 2009. Expedition 315 Site C0002. *In* Kinoshita, M., Tobin, H., Ashi, J., Kimura, G., Lallemant, S., Screaton, E.J., Curewitz, D., Masago, H., Moe, K.T., and the Expedition 314/315/316 Scientists, *Proc. IODP,* 314/315/316: Washington, DC (Integrated Ocean Drilling Program Management International, Inc.). doi:10.2204/iodp.proc.314315316.124.2009
[2] **Expedition 314/315/316 Scientists' addresses.**

doi:10.2204/iodp.proc.314315316.124.2009

Operations

Locations of holes drilled during Expedition 315 are shown in Figure F3.

Transit from Site C0001 to Site C0002

The D/V *Chikyu* departed IODP Site C0001 at 0230 h on 8 December 2007. The 7 nmi transit was covered at an average speed of 2.8 kt. We arrived at Site C0002 at 0530 h on the same day.

Hole C0002B

The vessel was on location at 0530 h on 8 December 2007 (Table T1). Deployment and calibration of four transponders occurred from 0530 to 1930 h. The vessel moved 4 nmi upcurrent from 1930 to 2215 h at an average speed of 1.6 kt. We started making up and running a 10⅝ inch rotary core barrel (RCB) assembly at 2215 h. In the meantime, we carried out minor troubleshooting of the dynamic positioning system. We spudded Hole C0002B at 0600 h on 9 December. After jetting to 50 mbsf, we started drilling with an RCB coring assembly with a center bit at 0745 h. While drilling to 181 mbsf, a problem with the top drive was found at 1300 h. We checked it and made repairs to the changing bolt. We started running in the hole at 1815 h, and we restarted drilling from 181 mbsf at 1830 h. We reached the starting coring depth (475 mbsf) at 0215 h on 10 December and installed an RCB core barrel and a sinker bar. We retrieved the center bit on the second run and then dropped an inner barrel and started coring at 0530 h. We continued coring until 0700 h on 11 December and cut 22 cores in the interval from 475 to 675 m core depth below seafloor (CSF). Leaking was found on a crown-mounted heave compensator booster line at 0700 h, and we spotted 10 m^3 of Hi-Vis mud and retrieved an inner barrel and a sinker bar. Repairs were completed by 1530 h. After washing and reaming from 634 to 669 m drillers depth below seafloor, we installed a sinker bar and restarted coring at 1730 h. After cutting Core 315-C0002B-23R, we could not recover the inner barrel. We redressed the running tool with a new shear pin. An inner barrel swivel assembly shaft was left down the hole. We ran a fishing tool (core catcher) in the hole with the coring line and were able to retrieve the assembly at 2230 h. We restarted coring at 2315 h and cut 39 cores by 1645 h on 13 December. The drill pipe became stuck twice, once at 1029 m CSF at 1650 h and again at 1030 m CSF at 1715 h, but came free with 300 kN of overpull each time. After cutting four more cores, hole conditions became worse below 1057 m CSF at 2230 h. The drill pipe was packed off, and weight on bit increased to 200 kN. The pipe was freed with 300 kN of overpull. We washed and reamed the hole repeatedly by sweeping Hi-Vis mud until the next morning; however, hole conditions did not improve. We finally decided to stop RCB coring and abandon the hole at 1345 h on 14 December. We displaced the hole with 1.3 specific gravity kill mud and pulled out of the hole by 2100 h. The remotely operated vehicle (ROV) was recovered at 1835 h on 15 December. We moved the vessel 6 nmi upcurrent at 2100 h, at an average speed of 1.5 kt.

Hole C0002C

The vessel was on location at 0130 h on 16 December 2007 (Table T2). We made up an 11⅞₁₆ inch hydraulic piston coring system (HPCS) assembly at 0630 h and started running in the hole at 0830 h. We installed a sinker bar and an inner barrel at 1530 h and cut two HPCS cores by 1815 h. We moved the vessel 10 m away from the hole to core the next hole.

Hole C0002D

The vessel was on location at 1830 h on 16 December 2007, and we continued HPCS coring at 1930 h (Table T3). We cut 13 cores with the HPCS until 0830 h the next morning. With 450 kN of overpull on Core 315-C0002D-13H at 120 m CSF, we overdrilled from 110 to 113 m CSF. We pulled the core line winch to the surface and found that we had not recovered the inner barrel (the sinker bar pin was sheared). We installed a new latch head and ran back in and latched. After another 2 m of overdrill, we attempted to pull free and released the inner barrel with 400 kN of overpull. We changed the latch head and replaced shear pins and V-packings on the inner barrel. We continued HPCS coring from 114 to 120 m CSF. We had high overpull (450 kN) again and overdrilled 5 m; the barrel came free with 400 kN of overpull. After recovering this core, we dropped the extended shoe coring system (ESCS) bottom-hole assembly for drilling. Having verified its landing, we started drilling at 1600 h at 120 m CSF. We ran a sinker bar assembly in the hole and recovered the ESCS. We then ran the advanced piston coring temperature tool (APCT3) in the hole and performed HPCS coring at 150 m CSF. To free the barrel, 200 kN of overpull was needed. We recovered the HPCS core and dropped the ESCS again. We verified its landing and started drilling at 159 m CSF at 2015 h. We ran the sinker bar assembly in the hole and recovered the ESCS at 2300 h. The final HPCS core was taken at 200 m CSF at 0110 h on 18 December. A total of 18 cores were cut in this hole. In situ temperature measurement with the APCT3 was attempted on Cores 315-C0002D-2H, 4H, 6H, 8H, 10H, 12H, 16H, and

18H; six attempts were successful. We displaced the hole with 26 m^3 of 1.3 specific gravity kill mud and pulled up to the surface from 0215 to 0545 h. We moved the vessel and then launched the ROV at 0730 h and retrieved four transponders by 1345 h. The vessel left for IODP Expedition 316 Site C0006 at 1345 h on 18 December.

Lithology

We recognized four lithologic units during examination of cores from Site C0002 (Fig. **F4;** Table **T4**). Units are differentiated based on persistent contrasts in grain size, layer thickness, sedimentary structures, trace fossils, and mineralogy. Because shipboard examination of split cores began at a coring depth of 479.40 m CSF, we also considered seismic reflection data and facies interpretations of logging-while-drilling (LWD) data to provide a broader stratigraphic context (see the **"Expedition 314 Site C0002"** chapter). Core recovery was generally poor to moderate and was particularly bad within intervals in which the log character is indicative of high sand content. Thus, we believe that LWD data provide a more accurate picture of facies character.

Unit I

Interval: Sections 315-C0002D-1H-1 through 15X-CC
Depth: 0–135.85 m CSF
Age: Quaternary
Lithology: silty clay to clayey silt, sand and silt turbidites, volcanic ash

Beginning at the seafloor, lithologic Unit I was sampled only for interstitial water and microbiology and was imaged using the multisensor core logger (MSCL) and X-ray computerized tomography. The cores were split and described at the Kochi Core Center after the expedition had concluded. The lithologic boundary is located at the bottom of Section 315-C0002D-15X-CC. The correlative boundary between logging Units I and II was placed at 135.5 m LWD depth below seafloor (LSF). The dominant lithology of Unit I is dark olive-gray and greenish gray to grayish green mud (silty clay to clayey silt) (Fig. **F4;** Table **T4**). Locally, mud is enriched in foraminifers and there are local dark color bands. Secondary lithologies include thin interbeds and irregular patches of dark greenish gray medium to fine sand, silty sand, sandy silt, and silt. Thin layers of light gray volcanic ash are also common. The coarser interbeds are typically 1 to 15 cm thick, with sharp bases, and many such beds display normal size grading and diffuse tops. Cross-laminae occur in some silt beds. These sedimentary structures are characteristic of turbidites. The thickest sand bed is ~1.86 m. Overall, the vertical trend for the unit thins and fines upward.

Interpretation of Unit I

Deposition of Unit I occurred in the distal reaches of the Kumano Basin, as did the deposition of Unit II below. The facies character is typical of a basin-plain type environment, with rhythmic interlaying of fine-grained turbidites and hemipelagic mud. Turbidity currents entered the basin frequently via submarine canyons and gullies along the upper slope and shelf. After examining the cores, we conclude that the differences in log character between logging Units I and II are related more to consolidation state than changes in lithology.

Unit II (forearc basin facies)

Interval: Sections 315-C0002D-15X-CC through C0002B-39R-CC
Depth: 135.5 m LSF to ~826.34 m CSF (830.4 m LSF)
Age: Quaternary
Lithology: silty clay to clayey silt with sand, silty sand, silt, and volcanic ash

After a coring gap of ~15 m, Unit II begins at a depth of 150.00 m CSF at the top of Section 315-C0002D-16H-1. There is a substantial gap in coring between 203.52 m CSF and the first core from Hole C0002B at 479.40 m CSF. The lower unit boundary based on coring data is located between the bottom of Section 315-C0002B-39R-CC (826.34 m CSF) and the top of Section 315-C0002B-40R-1 (834.00 m CSF). This pick is based on the occurrence of silty beds with plane-parallel laminae above the boundary. During LWD data interpretation, the equivalent contact between logging Units II and III was placed at 830.4 m LSF. The dominant lithology recovered from Unit II is greenish gray to grayish green mud (silty clay to clayey silt) (Fig. **F4;** Table **T4**). Secondary lithologies include thin interbeds and irregular patches of sand, sandy silt, and silt. Volcanic ash is rare. Zones of contorted bedding and soft-sediment folding occur locally. Logs show a much higher proportion of sandy layers than what was recovered by coring. Direct comparisons between core and log intervals indicate that recovery of sand and silt beds was <10%. Unfortunately, we were unable to recognize depositional cycles in the cores or systematic changes in the frequency of occurrence of turbidites.

In general, the mud in this unit is noticeably coarser than comparable deposits at greater depth. Mud is locally structureless but more commonly shows plane-parallel laminae and incipient fissility. Orien-

tation of this fabric is horizontal to gently inclined. Calcareous nannofossils are sparse in the clayey silt intervals. Bioturbation is patchy and relatively mild in severity (compared to Unit III). The ichnofauna is dominated by *Chrondrites*.

Dark gray silt, sandy silt, and silty sand are the characteristic interbeds of Unit II (Table **T5**). These beds are typically <5 cm thick and display sharp bases, faint plane-parallel laminae, normal size grading, and diffuse tops. Such features are typical of fine-grained turbidites. Silt and sand grains are composed mostly of quartz, feldspar, sedimentary and metasedimentary rock fragments (shale, argillite, chert, and quartz-mica grains), and a rich diversity of heavy minerals.

Interpretation of Unit II

Deposition of Unit II occurred in the distal reaches of Kumano Basin. The facies character is typical of a basin-plain type environment and does not significantly differ from that of Unit I. This interpretation is consistent with present-day bathymetry and the proxies for abundant silt and sand turbidites in the logs. Nannofossil datums show that sedimentation rates were high (400–800 m/m.y.) throughout the history of Unit II (see **"Biostratigraphy"**). Turbidity currents entered the basin frequently via submarine canyons and gullies along the upper slope and shelf. Arrival of the first turbidites, which began at ~1.6 Ma, depended on incision of through-going erosional conduits and sufficient uplift along the basin's seaward edge to form a deep depocenter.

Unit III (basal forearc basin)

Interval: Sections 315-C0002B-40R-1 through 49R-2
Depth: 834.00 (830.4 m LSF) to 921.73 m CSF
Age: Pleistocene to late Miocene
Lithology: greenish gray, gray, and gray-brown silty claystone

The boundary between lithologic Units II and III is defined by a shift in lithofacies from turbidites above to condensed mudstone below. As defined by log character, the unit boundary is positioned at 830.4 m LSF, which coincides with a coring interval of no recovery between Section 315-C0002B-39R-CC and the top of Section 315-C0002B-40R-1 (834.0 m CSF). Strata below the boundary are Pleistocene to late Miocene in age, and rates of sedimentation within that interval slowed to 18–30 m/m.y. (see **"Biostratigraphy"**). Lithologic variations in the cores are not distinctive enough to warrant further subdivision on the basis of texture, composition, or sedimentary structures. However, on the basis of lithology and nannofossil events, we recognize a pronounced unconformity at the base of Unit III at a depth of ~923 m CSF; the hiatus spans from ~3.8 to 5.0 Ma (see **"Biostratigraphy"**). A second possible hiatus occurs within lithologic Unit III at ~865 m CSF. The base of logging Unit III occurs at 935.6 m LSF. Fine-tuning of the biostratigraphy will be needed to pinpoint the position and duration of the hiatus. Our provisional pick for the unconformity is 921.73 m CSF, where a sharp color change signals a shift in carbonate and nannofossil abundance.

The dominant lithology of Unit III is greenish gray, gray, and gray-brown mudstone (silty claystone). Calcareous nannofossils are abundant in the mudstone. The mud texture is finer grained than equivalent deposits in Unit II, and bioturbation is more widespread and diverse. The ichnofauna is dominated by *Chrondrites,* with lesser *Zoophycos*. Secondary lithologies are limited to sparse beds and irregular lenses of volcanic ash. Locally, zones of intense green mineralization display gradational bases and sharp tops. Green particles, which range in size from sand to gravel, are widely dispersed through these intervals. Smear slide analysis indicates that the green particles are composed of glauconite. Sharp-topped zones may be firmgrounds, with evidence of scouring and reworking of compacted clay-rich sediment. Another striking feature within Unit III is subvertical sigmoidal clay-filled "vein structure" (see **"Structural geology"**). Development of these dewatering structures is clearly affected by lithology and firmness; veins are spaced more widely in the softer gray and gray-brown mudstone and are more closely spaced within the harder mineralized green intervals.

Interpretation of Unit III

We regard Unit III as a product of forearc or trench-slope deposition above the carbonate compensation depth (CCD), both prior to and during the early stages of formation of the Kumano Basin. Sediment-starved conditions were accompanied by a diverse assemblage of infauna. Localized cementation of the sediment surface (by glauconite and possibly phosphates and carbonates) was fostered by slow sedimentation and exposure to oxygenated seawater circulation. The stratigraphic occurrence of clay-filled vein structures seems to be uniquely tied to this facies. Rapid dewatering of firm mud may have been induced by shaking during earthquakes within an environment that was modulated by unusually slow rates of sedimentation. Similar structures have been documented on land and at several Ocean Drilling Program (ODP) sites (e.g., Ogawa and Miyata, 1985; Pickering et al., 1990; Lindsley-Griffin et al., 1990; Ogawa et al., 1992; Brothers et al., 1996).

As discussed below, we suggest that the base of Unit III (921.73 m CSF; 935.6 m LSF) is a depositional contact between accreted trench-wedge sediment and the initial deposits of hemipelagic mud on the lowermost trench slope. Seismic reflection profiles show complicated geometries with angular discordance and contrasts in structural style across the boundary. We regard the dramatic unconformity at ~922 m CSF as a manifestation of uplift along a system of out-of-sequence (splay) faults at ~5 Ma. Whether the uplift triggered erosion of accreted strata or just very slow sedimentation above the prism cannot be resolved without higher resolution biostratigraphy. This phase of tectonic activity led to bathymetric blockage along the seaward edge of an incipient Kumano Basin, creating a large depocenter. It is noteworthy that the depositional environment remained starved of significant terrigenous influx for >3 m.y. As discussed above, delivery of silt and sand turbidites into the basin began at ~1.6 Ma, signaling the arrival of Unit II deposition.

Unit IV (upper accretionary prism)

Interval: Sections 315-C0002B-49R-2 through 66R-CC
Depth: 921.73–1052.50 m CSF
Age: Miocene
Lithology: silty claystone to clayey siltstone with siltstone and sandstone

The boundary between Units III and IV is defined by a sharp change in structural style and a shift in lithofacies from condensed mudstone above to interbeds of mudstone, siltstone, and sandstone below. As defined by log character, the unit boundary is positioned at a depth of 935.6 m LSF. Beginning with Section 315-C0002B-50R-1 (929.0 m CSF), the mudstone is highly fractured. Strata below the boundary are Miocene in age and extend to the bottom of Hole C0002B at 1052.50 m CSF (Fig. **F4;** Table **T4**). Lithologic variations in the cores are not distinctive enough to warrant subdivision on the basis of texture, composition, or sedimentary structures.

The dominant lithology of Unit IV is gray to greenish gray and dark gray mudstone (silty claystone to clayey siltstone). Mudstone contains local wavy laminae or bands, as defined by darker green color and higher clay content. Concentrations of calcareous nannofossils are significantly lower here than within comparable mud deposits in Unit III. Bioturbation, as characterized by *Chondrites,* is moderate. More typically, mudstone takes on a mottled appearance. Thin layers of siltstone are rare. Sandstone also occurs locally, and in some cases sand is cemented by calcium carbonate (Table **T5**). Silt and sand grains are composed mostly of quartz, feldspar, sedimentary and metasedimentary rock fragments (shale, argillite, chert, and quartz-mica grains), and a rich diversity of heavy minerals (zircon, green and yellow tourmaline, epidote, green amphiole, and blue amphibole).

Interpretation of Unit IV

The depositional environment of Unit IV is difficult to interpret because of poor core recovery and a strong tectonic overprint characterized by intense fracturing, scaly fabric in mudstone, and fragmentation of sandstone beds (see **"Structural geology"**). Seismic reflection data indicate that the contact between Units III and IV is a boundary between the forearc basin and the accretionary prism, which means that the most likely depositional environment for Unit IV is trench wedge. Low concentrations of calcareous nannofossils point to a depositional environment below the CCD, probably near the base of the trench slope. The Quaternary trench-wedge environment of the Nankai Trough is sandy (Pickering et al., 1993; Moore, Taira, Klaus, et al., 2001). As another possibility farther outboard, the upper Shikoku Basin facies contains numerous beds of volcanic ash and virtually no sand or silt beds—at least where it has been cored in the Muroto and Ashizuri transects (Moore, Taira, Klaus, et al., 2001). We regard the top of Unit IV as a boundary between accreted trench turbidites and muddy slope-apron deposits. Resolution of biostratigraphy is not precise enough to tell whether or not the lower slope sedimentation began immediately after frontal accretion. Unlike the kindred boundary at Site C0001, the facies change from accretionary prism to muddy slope apron is sharp, but this does not necessarily require erosion along the contact.

X-ray diffraction mineralogy

Bulk powder X-ray diffraction (XRD) results provide useful constraints on the relative abundances of total clay minerals, quartz, plagioclase, and calcite. Hole C0002B data are shown in Figure **F5** and tabulated in Table **T6.** As a measure of how accurate these estimates are relative to absolute percentages, we completed regression analysis of percent calcite from XRD versus percent calcium carbonate from coulometric analysis (see **"Organic geochemistry"**). This comparison shows a shift in the coulometric data above values of ~10%, which is to be expected if the concentration of $CaCO_3$ is expressed as a percentage of the total solid mass (weight percent) (Fig. **F6**). The correlation coefficient is lower than that for a comparable regression for Site C0001. Two data points on

the regression plot show unusually large discrepancies, which we suspect are due to operator errors in recording sample codes for XRD.

Among the major minerals, values of calcite (XRD) show the greatest amount of variation at Site C0002, ranging from 0.1% (trace) to 28.2%. Average values are 2.1% for Unit II, 16.5% for Unit III, and 1.9% for Unit IV. The abrupt compositional shift across the Unit III/IV boundary is noteworthy (Fig. F5) and consistent with rapid uplift of the depositional site from below the CCD (Unit IV) to above the CCD (Unit III). The same compositional trend is evident, but more gradual, at ODP Sites 1175 and 1176 (Shipboard Scientific Party, 2001a, 2001b; Underwood et al., 2003). The relatively low concentration of calcite within Unit II is probably a consequence of dilution of biogenic carbonate by high influxes of terrigenous silt and clay into the Kumano Basin. Percentages of plagioclase at Site C0002 vary between 13.4% and 34.9%. Unit II contains an average of 23.2% plagioclase, whereas Unit III contains an average of 18.1% and Unit IV contains 17.3%. Relative concentrations of total clay minerals are between 30.9% and 65.3%, with a significant decrease in Unit III. Quartz content varies between 13.2% and 32.7%. Unit II contains an average of 27.8% quartz. Units III and IV average 20.6% and 21.5% quartz, respectively.

Structural geology

The overall objective of drilling at Site C0002 was to sample the sediments that comprise the lower sections of Tertiary Kumano Basin as well as the more deformed sediments beneath the basal unconformity. These buried sediments are considered to be part of the Shimanto accretionary prism, which is exposed onshore in southwest Japan only a few tens of kilometers from the drill site. With this goal in mind, Expedition 315 scientists cored sediments from 0 to 200 m CSF and 475 to nearly 1100 m CSF and retrieved samples and data from both above and below the unconformity. Structural geologists identified and documented over 500 structural features in the cored sediments, of which nearly 80 were oriented with shipboard paleomagnetic data. The results are consistent with observations and interpretations of LWD data collected during Expedition 314, which indicate north–south extension and suggest that the preliminary conclusions from Site C0001 (i.e., in the slope apron sequence) also extend to Site C0002. Specifically, Site C0002 records an early phase of northeast–southwest extension, similar to the deformation recorded in the slope apron at Site C0001, as well as a later period of north–south extension not recorded at Site C0001.

Types and distribution of structures

Structural geologists working at Site C0002 identified five main structural features and one relatively minor feature (Fig. F7). The main features observed were steepened bedding, faults, breccia, shear zones, and vein structures (Figs. F7, F8, F9). In Hole C0002D, bedding was the only observed structure, and no deformational structures were observed in Hole C0002C. Fissility occurred only in the upper sections of Hole C0002B and was consistently oriented parallel to bedding; thus, it was grouped with bedding. All of these features, except fissility, were also identified and described at Site C0001; therefore, only differences in textures and distributions of structures at this site are noted here.

Steepened bedding

Bedding is subhorizontal to 80 m CSF, dipping mostly <5° (Fig. F9) in Hole C0002D. From 80 to 160 m CSF the range of bedding dip increases to as much as 10°, and the range increases as much as 17° at 203 m CSF close to the bottom of the hole (Fig. F9). It is uncertain whether this relatively high dip at 203 m CSF is meaningful or not, because no cores were recovered between 160 and 203 m CSF. Combined with data in Hole C0002B from 475 to 1057 m CSF, the dip at 203 m CSF may be exceptional because dip is generally <10° from 475 to 600 m CSF (Fig. F9). In Hole C0002B, the mean dip of bedding increases progressively from near 0° at 500 m CSF to an average of 45° in the accretionary prism at the bottom of the hole (bedding, Fig. F7A). The range in bedding dip also increases with depth such that near the bottom of the hole bedding ranges from 20° to 80°. This wide range in dip with depth and the absence of clear peaks in dip magnitude limits correlation of specific changes in bedding dip with other features. However, subtle peaks in bedding dips occur at 750, 850, 950, and 1025 m CSF.

Faults

Faults (Fig. F7B) are relatively rare in the upper 400 m of Hole C0002B. Although a small cluster of moderately dipping faults occurs at ~700 m CSF, most of the observed faults are present in two clusters below 900 m CSF (Fig. F8). One cluster ranges from 920 to 950 m CSF, whereas the other cluster shows more scatter in terms of depth distribution and ranges from 1000 to 1050 m CSF. These two clusters of faults also record the greatest range in dip as well as the highest dip magnitude (i.e., 90° at 920 m CSF) of all of the faults at this site. The upper cluster of faults is just below the top of Unit IV, although a few faults are also present above the boundary. LWD data (i.e.,

resistivity) and shipboard physical properties show that this boundary records the largest contrast in physical properties and probably represents the top of the accretionary prism. Cores also show well-developed stratal disruption below this boundary (Fig. F7C). The lower cluster of faults occurs deeper within Unit IV. Although much of the deformation represented by faulting at Site C0002 occurs below the Unit III/IV boundary, faults are also present above the boundary. Normal faults are particularly well organized close to and just above the boundary, consistent with core observations indicating that they are the youngest structures. Systematic analyses of the fault geometries, histories, and kinematics of the faults just above and below the boundary at 920 m CSF, however, have not been completed.

Shear zones

Shear zones (Fig. F7D) are less common than faults but show a similar distribution with depth, although only three shear zones were recognized above 900 m CSF (Fig. F8). Shear zones occur in two clusters, one between 920 and 940 m CSF and the second between 1025 and 1050 m CSF, similar to the distribution of faults.

Breccia

Breccia (Fig. F7B) is particularly well developed in the lower sections of Hole C0002B, especially near the top and bottom of Unit III and in the accretionary prism beneath the unconformity. The extent of brecciated zones was probably larger than indicated by core-based observations, as recovery was generally poor in these intervals.

Vein structures

Vein structures are particularly well developed between 850 and 920 m CSF (Fig. F8), and a wide variety of forms and shapes are displayed (Fig. F7D). This interval generally correlates with lithostratigraphic Unit III, which is a clay-rich hemipelagic mud sandwiched between accreted sediments below and silty-clay hemipelagic sediments above. Unit III also has higher $CaCO_3$ content than the overlying and underlying units (see **"Lithology"** and **"Organic geochemistry"**). Vein structures, although similar to vein structures observed at Site C0001, are generally larger in both height and width, often extending parallel to the core axis for tens of centimeters. S-shaped (or sigmoidal) vein structures are also present but are more elongate in the direction of the core axis. Although many of the vein structures appear perpendicular to bedding, they are more widely spaced than those observed at Site C0001. These more widely spaced veins are also generally thicker, suggesting that the width, or size, of the vein structures is a function of the availability of vein-filling material in the wall rock.

Crosscutting relations and kinematics

Three phases of deformation are suggested by the textures and crosscutting relations observed in the cores. An early phase of thrust faulting (and possibly strike-slip faulting) is followed by two phases of normal faulting with the first recorded by shear zone formation and associated with northeast–southwest extension and the second recorded in normal fault formation and associated with north–south extension concentrated in Unit II at ~750 m CSF. Importantly, because of the limited time spent at this site and the limited number of structural geologists on board at the time of Site C0002 coring, this progressive history is based on only a few observations; thus, future work on the cores may refine the various relations or substantially change the progressive history. The proposed history, however, is consistent with the known or inferred geologic history of the region and with the interpretation of seismic reflection profiles that show late-stage normal faults associated with north–south extension.

Of the planar and linear features observed in the cores, ~20% (i.e., 80 of the over 450 features recorded) were reoriented to true north using nearly 50 individual paleomagnetic poles obtained from the shipboard paleomagnetic laboratory. Of these features, ~30 were bedding and 20 were vein structures with the remainder comprising faults, shear zones, fissility, and breccia. The remaining data could not be reoriented because of extensive whole-round sampling, magnetic overprint related to the magnetic properties of the mud used and/or generated during drilling, and drilling-related disturbances. Reoriented data provide key insights into the kinematics and the state of stress in sediments cored at Site C0002.

Bedding orientations corrected for drilling-related rotations provide a fundamental guide to the degree of deformation at Site C0002 (Fig. F10). Bedding is generally horizontal at this site, although a few poles trend west–southwest, suggesting east–northeast tilting.

The geometries and kinematics of the structural features observed in the two intervals of deformation at Site C0002 vary significantly. The upper interval, at the top of Unit IV, contains both shear zones and faults with normal offset, whereas the lower interval contains faults and shear zones with a variety of offsets, including thrust, normal, and strike slip. When corrected for drilling-related rotations, the normal faults and shear zones in the upper interval define two populations. The youngest population, based on

limited crosscutting relations, is a set of variably oriented normal faults. Although there are relatively few data, the available reoriented slickenlines generally trend north–south (Fig. F11). Two additional reoriented faults with normal offset also have geometries consistent with north–south extension, whereas a third fault dips west, suggesting east–west extension. Shear zones represent the older populations of structures from this interval, and although they also record normal displacements, they display a different geometry than normal faults. Shear zones generally strike northwest and dip steeply west or gently east (Fig. F12). Although slip lineations were not observed for these structures, five of the eight shear zones have normal displacements, suggesting northeast–southwest extension.

The lower interval of deformation (i.e., below ~1000 m CSF) records a variety of structures, although only a few have been reoriented. Reoriented structures with known kinematics include two thrust faults, two strike slip faults, and two zones of relatively intense brecciation (Fig. F13). Visual inspection of these limited data indicates that they are all consistent with northwest–southeast shortening, suggesting that they are kinematically related. Kinematics for the group as a whole show north–south shortening (Fig. F13).

Discussion

Drilling at Site C0002 successfully penetrated and sampled the lower Kumano Basin sequence, as well as the underlying accretionary sequences considered to be part of the Tertiary Shimanto belt. Note that fossils retrieved from this site (see **"Biostratigraphy"**) are younger than the Shimanto belt exposed on land. Structural data collected from this site show three phases of deformation that are consistent with

1. Northwest–southeast shortening concentrated primarily in Unit IV and interpreted to be the accretionary prism;
2. A middle phase of northeast–southwest extension along the margin, which is similar to results obtained from Site C0001; and
3. A final, and still ongoing, phase of generally north–south extension recorded primarily in structures in Unit II from the Kumano forearc basin.

The kinematics of the last phase of deformation are consistent with LWD borehole breakout data obtained during Expedition 314. Additional data obtained at the Kochi Core Center or through future drilling programs are necessary, however, to support these preliminary results.

These preliminary results also provide new data for developing and testing hypotheses related to the early history of the accretionary prism and to better understanding the transition from accretion to extension as is seen across the Kumano Basin transect. For example, do the similarities in progressive deformation histories we have identified in Sites C0001 and C0002 represent the advection of the accreted rocks through a steady strain field, or has the strain field changed through time? Also, both sites record extensional deformation near the basin/prism contact where unconformities appear to be present. Is it possible that the time gaps indicated by unconformities are due to the structural removal of the section (e.g., through regional scale sliding or slumping)? These questions, among others, will be investigated in collaboration with Expedition 314 and 315 shipboard parties as NantroSEIZE experiments continue.

Biostratigraphy

Preliminary biostratigraphy for Site C0002 is based on calcareous nannofossils and planktonic foraminifers. The complete nannofossil stratigraphy was established during the expedition, but ship-board planktonic foraminiferal biostratigraphic results were only generated for the upper 773 m CSF of Hole C0002B because of the early scheduled departure of the foraminifer biostratigrapher before the end of Expedition 315. The remaining examination of planktonic foraminifers was shore-based. Biostratigraphy for Holes C0002C and C0002D is exclusively based on calcareous nannofossils.

Preservation and abundance of calcareous microfossils vary throughout the sequence. Despite differential preservation of nannofossil and foraminifers in the studied samples, a general common preservational pattern of well- to moderately preserved microfossil assemblages in the upper part of the site (478.28–930.10 m CSF) and moderate to poor preservation below 930.10 m CSF is observed. Microfossil abundances vary strongly. Nannofossil and foraminifer age estimates are in good agreement for Site C0002 (Fig. F14). Retrieved sediments provide a discontinuous sedimentary record from the Pleistocene to the late Miocene. The succession of calcareous microfossil events delineates intervals of different sedimentation rates. Assemblages recovered from the upper 848.38 m CSF (lithologic Units I and II) are Pleistocene in age. The spacing of biostratigraphic events is wide, revealing high sedimentation rates between 400 and 800 m/m.y. In contrast, the sequence belonging to lithologic Unit III comprises a suite of Pliocene biostratigraphic events within a

short depth interval (848.38–923.71 m CSF). Here, sedimentation rates are much lower, ranging from 18 to 30 m/m.y. Some samples even contain several events of different age. These horizons can be interpreted as results of low sediment rates or tectonic processes. In sediments of lithologic Unit IV only one nannofossil event was recognized, assigning this unit a late Miocene age.

Calcareous nannofossils

Shipboard nannofossil stratigraphy for this site is based on the recognition of the 22 events reported in Table **T7.** Nannofossils are continuously present throughout the sequence (Tables **T8, T9**). Although nannofossils significantly decrease in abundance downhole, a good biostratigraphic framework was established for the entire succession. In samples from the uppermost 923.71 m CSF of Site C0002, nannofossils are abundant to common with moderately to well-preserved assemblages, with the exception of an interval from 555.27 to 613.76 m CSF where nannofossil abundances are low and specimens are moderately preserved. Below 923.71 m CSF, nannofossil content of samples mainly belonging to lithologic Unit IV decreases drastically with only poorly or moderately preserved specimens.

Core catcher samples recovered from the upper 158.90 m of Holes C0002C and C0002D (Table **T9**) provide the biostratigraphic framework of the uppermost 203.57 m CSF for this site. Spot-coring started from Core 315-C0002D-15X. For these cores only minimum or maximum age datums can be provided.

The only sample recovered from Hole C0002C (Sample 315-C0002C-1H-CC, 0–5 cm) contains dominant *Emiliania huxleyi* over *Gephyrocapsa* spp. (>3.5 µm). Therefore, cored material from 6.47 m CSF is younger than 0.063 Ma. However, the uppermost core catcher sample from Hole C0002D (Sample 315-C0002D-1H-CC, 27–32 cm) at 5.85 m CSF yields dominant *Gephyrocapsa* spp. (>3.5 µm) over *E. huxleyi,* indicating a minimum age of 0.063 Ma for the retrieved sediment. It is also possible that differences in abundance of the species mentioned are ecologically controlled. The first occurrence (FO) of *E. huxleyi,* which also defines the base of Zone NN21, is found between Samples 315-C0002D-4H-CC, 0–5 cm, and 5H-CC, 0–5 cm, at a mean depth of 38.81 m CSF. Within the same interval, the last occurrence (LO) of *Pseudoemiliania lacunosa* in Sample 315-C0002D-5H-CC, 0–5 cm, at 43.52 m CSF is recorded. This event marks the base of Zone NN20 and provides a minimum age of 0.436 Ma. None of the studied samples could be placed in nannofossil Zone NN20. Either Zone NN20 lies in the core sections above the core catcher or it is not present because of a hiatus. Sample 315-C0002D-11H-CC, 0–5 cm (100.70 m CSF), contains *Reticulofenestra asanoi*. The last consistent occurrence (LCO) of this species indicates a minimum age for this sample of 0.9 Ma. The presence of *R. asanoi* along with common *Gephyrocapsa* spp. (≥4 µm) provides a maximum age of 1.04 Ma for Sample 315-C0002D-15X-CC, 19–24 cm, based on their reentrance. *R. asanoi* is commonly present in the lowermost sample, 315-C0002D-18H-CC, 0–5 cm, at 203.57 m CSF. The bottom sediments of Hole C0002D are younger than 1.078 Ma based on the first consistent occurrence of this species.

Cores retrieved from the upper part of Hole C0002B from 470 to 848.38 m CSF yield abundant and very well preserved calcareous nannofossils, assigning lithologic Unit II a Pleistocene age (Table **T8**). Within the Pleistocene assemblages several events could be identified. The uppermost core catcher sample from Hole C0002B contains *Gephyrocapsa* spp. (>5.5 µm). Hence, their LO indicates an age of at least 1.24 Ma for Sample 315-C0002B-1R-CC, 0–23.5 cm (478.28 m CSF). The LO of *Helicosphaera sellii* was found between Samples 315-C0002B-2R-CC, 0–5 cm, and 3R-CC, 11.5–16.5 cm (485.98–495.37 m CSF). The LCO of *Gephyrocapsa* spp. (>5.5 µm) is recorded between Samples 315-C0002B-2R-CC, 0–5 cm, and 3R-CC, 11.5–16.5 cm (485.98–495.37 m CSF). Low sedimentation rates are assumed for the interval between Samples 315-C0002B-40R-CC, 0–5 cm, and 48R-CC, 0–5 cm (837.56–916.77 m CSF). They are delineated by several nannofossil events. The Pliocene/Pleistocene boundary is placed between Samples 315-C0002B-40R-CC, 0–5 cm, and 42R-CC, 0–5 cm (837.56–859.11 m CSF), based on two nannofossil events occurring above and below the epoch boundary. In cores above the boundary, the FO of *Gephyrocapsa* spp. (>3.5 µm) is detected at 842.97 m CSF, indicating an age of 1.67 Ma between Samples 315-C0002B-40R-CC, 0–5 cm, and 41R-CC, 0–5 cm (837.56–848.38 m CSF). The LO of *Discoaster brouweri* (2.06 Ma), which defines the base of nannofossil Zone NN19 that approximates the Pliocene/Pleistocene boundary, is recorded at 853.75 m CSF between Samples 315-C0002B-41R-CC, 0–5 cm, and 42R-CC, 0–5 cm. The base of Zone NN18 is determined by the LO of *Discoaster pentaradiatus* between 2.39 and 2.51 Ma. This event is located between Samples 315-C0002B-42R-CC, 0–5 cm (859.11 m CSF), and 43R-CC, 0–5 cm (870.52 m CSF). In the same interval, the LO of *Discoaster tamalis,* which provides an age datum of 2.87 Ma, is recorded. The LO of *Discoaster surculus,* which marks the base of Zone NN17 at 2.52 Ma, is found at a mean depth of 891.78 m CSF, between Samples 315-C0002B-45R-CC, 0–5 cm, and

46R-CC, 0–5 cm. The LO of *Sphenolithus* spp. at 3.65 Ma is placed between Samples 315-C0002B-47R-CC, 0–5 cm, and 48R-CC, 0–5 cm, at a mean depth of 911.84 m CSF. The interval between Samples 315-C0002B-48R-CC, 0–5 cm (916.77 m CSF), and 49R-CC, 0–5 cm (923.71 m CSF), contains several nannofossil events, suggesting either sediment starvation or an unconformity. Here the LO of *Reticulofenestra pseudoumbilicus* (>7 µm), the LO of *Ceratolithus acutus,* and the FO of *Ceratolithus rugosus,* which marks the base of Zone NN13, are detected, spanning a maximum time interval of 3.79–5.12 m.y. The LO of *Ceratolithus acutus* at 5.04 Ma, which approximates the Miocene/Pliocene boundary, was not discovered in the studied samples. The LO of *Discoaster quinqueramus* at 5.59 Ma is located between Samples 315-C0002B-49R-CC, 13–18 cm (923.71 m CSF), and 50R-CC, 0–5 cm (930.10 m CSF). This event is assigned to the uppermost Miocene. Here, a marked change in nannofossil abundance and preservation is observed. Below 930.10 m CSF, nannofossil abundance varies from rare to few with mostly poorly preserved specimens. The lowermost event detected, the LO of *Nicklithus amplificus,* provides an additional datum level of 5.9 Ma between Samples 315-C0002B-65R-CC, 0–5 cm (1049.38 m CSF), and 66R-CC, 6–11 cm (1052.40 m CSF). This observation indicates an age of at least 5.9 Ma for the bottom of the hole. The concomitant presence of *R. pseudoumbilicus* (>7 µm) further constrains the time window for this interval to a maximum age of 7.1 Ma.

Planktonic foraminifers

All Hole C0002B core catcher samples from 478.28 to 1052.40 m CSF were examined in onboard and shore-based studies. Fossil preservation of planktonic foraminifers shows changes from poor (or even barren) to good throughout the examined sequence. Besides changes in foraminiferal preservation and abundance, there is also a prominent shift in assemblage composition observable. It occurs at the Unit III/IV boundary. Assemblages within Units II and III are mainly composed of temperate to cosmopolitan genera (*Neogloboquadrina, Globigerina,* and *Globoconella*) associated with tropical to subtropical genera (*Globigerinoides, Globorotalia,* and *Pulleniatina*). In contrast, the lower assemblage from Unit IV is characterized by cold-temperate to cosmopolitan taxa, including *Neogloboquadrina pachyderma* and *Globigerina bulloides*.

Fourteen biohorizons are recognized from Hole C0002B (Table **T10**). Because of the sparse and patchy occurrence of a number of biostratigraphically important key species, the exact positioning of datum events remains questionable and requires the postcruise analysis of additional samples. Stratigraphic distribution of selected species is shown in Table **T11.** *Globoturborotalita obliquus* sporadically appears in the sequence. Its uppermost occurrence is recorded in Sample 315-C0002B-2R-CC, 0–5 cm. Therefore, the LO of the species (1.30 Ma) should be located above 485.98 m CSF. *Neogloboquadrina asanoi* exhibits a relatively high abundance in Sample 315-C0002B-42R-CC, 0–5 cm. The LO of the species (1.8 Ma) is placed between Samples 315-C0002B-41R-CC, 0–5cm, and 42R-CC, 0–5cm (848.38–859.11 m CSF). *Truncorotalia truncatulinoides* yields sparsely in the upper part of the sequence, and the FO of this species (1.93 Ma) is suggested between Samples 315-C0002B-31R-CC, 0–5 cm, and 315-C0002B-32R-CC, 0–5 cm (753.86–767.20 m CSF). This biohorizon defines the lower boundary of Zone N.22. The FO of *T. truncatulinoides* is placed >100 m above the LO of *N. asanoi* at the present site. The reverse occurrence of these biohorizons was also observed at Site C0001. The delay of this event in the study area may be caused by ecological factors.

The FO of *Globoconella inflata* modern form (2.3–2.5 Ma) is clearly recognized between Samples 315-C0002B-42R-CC, 0–5 cm, and 43R-CC, 0–5 cm (859.11–870.52 m CSF). The FO of *Truncorotalia tosaensis* (3.35 Ma) defining the base of Zone N.21 is observed in the same interval as *G. inflata*. However, the precise position of the biohorizon could be located further downhole because of the sporadic occurrence of the species. Three samples from Unit IV contain *Dentoglobigerina altispira*, and the LO of this species (3.47 Ma) is supposed to be above Sample 315-C0002B-49R-CC, 13–18 cm (923.71 m CSF). The LO of *Sphaeroidinellopsis seminulina* sensu Gradstein et al. (2004) (*S. seminulina* and *S. subdehiscens* of the present author) (3.59 Ma) is detected between Samples 315-C0002B-47R-CC, 0–5 cm, and 48R-CC, 0–5 cm (906.91–916.77 m CSF). *Hirsutella margaritae* occurs only in two samples from Unit IV. The LO of this species (3.85 Ma) is located above Sample 315-C0002B-52R-CC, 0–5 cm (949.06 m CSF). *Pulleniatina* spp., consisting of *Pulleniatina primalis* and *Pulleniatina obliquiloculata*, show the change in coiling direction from sinistral to dextral (SD) between Samples 315-C0002B-46R-CC, 0–5 cm, and 49R-CC, 13–18 cm (897.36–923.71 m CSF). This coiling change corresponds to the older event SD1 (4.08 Ma). The younger event SD2 (1.7–1.8 Ma) cannot be identified in the present site, probably because of the sparse occurrence of *Pulleniatina* spp. around the lower part of Unit II. The FO of *Truncorotalia crassaformis* (4.31 Ma) is recognized between Samples 315-C0002B-48R-CC, 0–5 cm, and 49R-CC, 13–18 cm (916.77–923.71 m CSF). The LO of *Globoturborotalita*

nepenthes (4.37 Ma) is found between Sample 315-C0002B-51R-CC, 0–5 cm, and 52R-CC, 0–5 cm (946.24–949.06 m CSF). Because of the sparse occurrence of *Globorotalia tumida* and *Globigerinoides conglobatus* in the studied samples, their FO datum levels are tentatively placed. The FO of *G. tumida* is suggested between Samples 315-C0002B-49R-CC, 13–18 cm, and 50R-CC, 0–5 cm, at a mean depth of 926.90 m CSF, providing a datum level of 5.57 Ma. The FO of *G. conglobatus* at 6.2 Ma is recorded between Samples 315-C0002B-57R-CC, 0–5 cm, and 58R-CC, 0–5 cm (996.35–1007.50 m CSF). The lowermost sample of the present site (315-C0002B-66R-CC, 6–11 cm; 1052.40 m CSF) yields *P. primalis*. The presence of the species indicates the maximum age of the bottom of the hole to be 6.6 Ma based on its FO, which determines the base of Subzone N.17b.

Paleomagnetism

Paleomagnetic directions

Remanent magnetization of Holes C0002B and C0002D was measured in order to construct a paleomagnetostratigraphy. Different procedures described below were employed for measurement on two holes.

Hole C0002B

Remanent magnetization of archive-half core sections from Hole C0002B was measured at 5 cm intervals. We measured natural remanent magnetization (NRM) demagnetized directions and intensities at 0, 5, 10, 15, 20, 25, and 30 mT peak fields to identify characteristic remanent magnetization (ChRM). Profiles of declination, inclination, and intensity after demagnetization at 30 mT with depth are shown in Figure **F15.** Distribution of declination on samples taken with the RCB should be randomly scattered, as can be observed below 620 m CSF; however, declination in the interval above 620 m CSF shows highly clustered directions. We doubt that those directions are a natural signal. Although the mechanism is not clear so far, the quality of cores taken with the RCB is inadequate in the interval above 642 m CSF (above Core 315-C0002-20R). Apart from this problematic issue, magnetization in the other intervals is relatively stable (Fig. **F16A, F16B**), despite numerous biscuits induced by the RCB. Paleomagnetic directions are grouped by continuous coherent pieces, and mean directions are calculated to provide orientation for structure data (Table **T12**).

Hole C0002D

Remanent magnetization of Hole C0002D was measured using discrete samples at the Kochi Core Center. One discrete sample was carefully collected from an undisturbed part of each working half. NRM demagnetizated directions and intensities at 0, 5, 10, 15, 20, 25, 30, 40, 50, and 60 mT peak fields were measured to identify ChRM using the magnetometer (2G Enterprises, model 755R). A typical demagnetization behavior of magnetic vectors is shown in Figure **F16C.** The steeper NRM inclination in the diagram between 0 and 5 mT levels is probably due to drilling-induced overprints, and this character is recognized in the most samples of Hole C0002D.

Magnetic reversal stratigraphy

Inclination after alternating-field (AF) demagnetization at 30 mT was used to determine the polarity pattern for Holes C0002B and C0002D. The magnetic polarity record was then identified by referring to biostratigraphic datum (see **"Biostratigraphy"**) and correlated with the geomagnetic polarity timescale of Gradstein et al. (2004). The result is summarized in Table **T13.** An inclination profile of Hole C0002D after demagnetization at 30 mT with depth is shown in Figure **F17.** The inclination of the interval between Sections 315-C0002D-1H-1, 110 cm, and 10H-3, 125 cm (1.20–85.625 m CSF), can be correlated to the Brunhes Chron. Although the polarity in the interval between Sections 315-C0002D-10H-4, 108 cm, and 13H-7, 115 cm (86.853–118.09 m CSF), is not clear, we interpret that the interval which is dominant in negative inclination is correlated to C1r Chron (0.781–0.988 Ma) in reference to the biostratigraphic datum (see **"Biostratigraphy"**). The top of the normal polarity at Section 315-C0002D-13H-8, 130 cm (119.58 m CSF), can be correlated to the top of the Jaramilo event (0.988 Ma). Because the depth recovered by Core 315-C0002D-15X (129.15 m CSF) is uncertain (see **"Operations"**), the correlation below this depth in Hole C0002D is unknown.

Inclination after AF demagnetization at 30 mT was used to determine the polarity pattern for Hole C0002B. The interval between 533 and 620 m CSF is excluded from the interpretation. Clear polarity change from positive to negative inclinations upward is observed between Cores 315-C0002B-40R-4, 20.0 cm (837.02 m CSF), and 41R-4, 85.0 cm (847.59 m CSF). Referring to biostratigraphic datum, this reversal can be correlated to the top of the Olduvai Subchron (1.778 Ma) and reversed polarity above this horizon can be correlated to the Matuyama Chron (Fig. **F18**).

Inclination and bedding dipping

Inclination value in the interval from 605 to 840 m CSF in Hole C0002B is close to the expected inclination (52°), which can be calculated from the site lati-

tude (33°N) (Fig. F19). The interval of Unit III, however, reveals a significantly steeper inclination (mean inclination = 65°) than expected. Unit IV inclination shows large variation. Structural data obtained by logging at this site and bedding dip observed by core inspection (see **"Structural geology"**) show that Unit III has an inclined bedding plane and the degree of bedding dip in Unit IV becomes scattered. Inclination variation is obviously in conjunction with bedding dip variation. The steeper inclination observed in Unit III, especially, has a constraint for the dip direction. Steepening inclination requires that dip direction is subparallel to the direction of sample magnetization, based on the assumption that the sample was magnetized during normal polarity. In the case of Unit III, northward bed dipping (from northwest to northeast) is accountable for steeper inclination. Interestingly, Unit IV inclination shows a wider distribution in the shallower and steeper sides. If the original magnetic inclination of Unit IV is positive, shallower inclination can be explained by dipping either south, east, or west. Because of this, the azimuth of bedding of Unit IV may not be constant.

Inorganic geochemistry

Interstitial water geochemistry

A total of 54 whole-round sections were collected for interstitial water analyses from Site C0002 (31 samples from Hole C0002B; 23 samples from Hole C0002D) (Table T14). Routine samples were collected at a frequency of approximately one whole-round sample per core according to core condition except for the first two cores just below the seafloor (2 samples each from Cores 315-C0002D-1H and 2H). To obtain enough interstitial water for onboard and shore-based analyses, 20 to 40 cm long sections were squeezed.

Sulfate, alkalinity, phosphate, and ammonium

Sulfate concentration decreases linearly with depth from a near seawater value to nearly 0 mM at 9 m CSF. This sulfate gradient of ~3.4 mM/m results in a flux of 1.6×10^{-3} mmol/cm^2/y using Fick's first law of diffusion with a diffusion coefficient of sulfate of 5.8×10^{-6} cm^2/s at 5°C and sediment porosity of 0.65 (Reeburgh, 1976; Borowski et al., 1996) (Fig. F20). This flux of sulfate should be equal to the flux of dissolved methane from below, similar to the case at Site C0001. However, the flux at Site C0002 is ~1.3 times higher than that at Site C0001. Sulfate concentrations in general are between 1.0 and 4.0 mM in Unit II in samples from Hole C0002B, well above the analytical detection limit (Fig. F20) and concentrations in interstitial water samples from Hole C0002D (generally <0.6 mM) that were retrieved from below the sulfate-methane transition (SMT). Although the potential contamination of drilling fluid during core recovery cannot be precluded because of very low water content in the whole-round core sections from Hole C0002B, observations of high-sulfate fluids in greater sections from previous studies (e.g., ODP Sites 1173 and 1174 and Hole 1176A) may suggest input of such sulfate-rich deep fluids into the cored interval.

Alkalinity and ammonium concentrations reach higher values than those observed at Site C0001. Although these concentrations steeply decrease in Unit II, levels are much higher than those at Site C0001 throughout the entire interval with the exception of one sample at 160 m CSF. Phosphate concentrations are also higher at Site C0002 than at Site C0001. There is a local phosphate maxima associated with the alkalinity maxima, yet there is a deeper more concentrated maximum near the bottom of Unit I. Below this maxima, phosphate concentrations decrease, reaching levels that are below the detection limit of shipboard analyses, ~3.3 µM, at ~600 m CSF (Table T14). Clearly the products of organic matter degradation show a substantial difference between diagenetic processes at Sites C0001 and C0002. These products remain deep within the cored section. For example, alkalinity and ammonium concentrations are 10 and 3.5 mM, respectively, at the bottom layer of Unit II between 800 and 830 m CSF. This lithologic boundary may represent a change in diagenetic rates.

Halogens (salinity, Cl, and Br)

Salinity and chlorine concentrations consistently decrease downhole in Unit I with some samples with substantially lower values in the depth interval between 120 and 200 m CSF. These lower values or dilutions are ascribed to the dissociation of gas hydrate during core recovery (e.g., Hesse, 2003), which are consistent with resistivity logs collected during Expedition 314. Br concentrations are diluted at the same depths as the chlorine data; however, they exceed 1200 µM at 86 m CSF. Given the biophilic nature of bromine, this profile indicates strong inputs from organic sources, probably associated in part with a gas hydrate. Salinity and concentrations of Cl and Br consistently increase downhole in the lower part of Unit II (Hole C0002D), reaching 480 mM for Cl and 950 mM for Br at ~810 m CSF. Below this depth, values slightly decrease toward the bottom of the hole (Fig. F20). At the base of the hole, Cl concentration is 456 mM, which is well below the seawater value (559 mM). In contrast, Br concentration at the base

of the hole remains larger than the seawater value (840 µM), reflecting sources from organic matter degradation at depth (Fig. F20).

Major cations

Interstitial water sodium concentrations in Unit I are relatively constant at seawater values (480 mM) in Hole C0002D, except in gas hydrate–bearing sediments. Concentrations drop from the base of Hole C0002D to the first sampled depth in Hole C0002B. Here, there is a slight increase in Na concentrations with depth in the lower part of Unit II, reaching almost steady values around 430 mM at 807 m CSF (Fig. F21). Potassium and calcium concentration profiles are similar to those at Site C0001 in Unit I. Concentrations of these elements in Hole C0002B increase slightly toward ~800 m CSF at the base of Unit II. Below this depth, potassium concentrations decrease to the lowest observed level, ~2 mM. In contrast, calcium concentrations increase to the highest observed level, ~20 mM, at the bottom of Site C0002 (Fig. F21). These changes are attributable to the progressive reaction between interstitial water and clay minerals through Units III and IV or deeper, probably a result of smectite illitization. Similarly, the magnesium concentration profile is very similar to that at Site C0001.

Minor cations

Although silica and boron concentration profiles in Unit I are comparable to those at Site C0001, values are more scattered particularly below Unit II. The silica profile shows a local maxima at ~915 m CSF in Unit III before decreasing in Unit IV (Fig. F21). More pronounced maxima in the same interval are found in the concentration profiles of lithium, strontium, and barium, reflecting the liberation of these minor elements from the clay mineral phase during diagenesis within this interval (Figs. F21, F22). Manganese concentrations are relatively constant with depth, even in Unit III; however, there is a rapid concentration increase within Unit IV below 922 m CSF to >12 µM. In contrast, iron concentration drops to <20 µM in Unit IV (Fig. F22). These distributions may reflect cycling of iron manganese minerals.

Trace elements

As observed at Site C0001, transition metals, except copper, have similar profiles to manganese and iron, depending on the redox condition of host sediments. Molybdenum concentration gradually increases in Unit I with relatively large variation at the boundary between Units I and II and is constant at ~200 nM in Units II and III with manganese and peaks at >830 nM in Unit IV (Fig. F22). Concentrations of vanadium and zinc are largely scattered in Unit I at the same level as observed at Site C0001. Within the deepest Unit IV, Zn and Fe concentrations are depleted relative to the overlying Unit III. In contrast, Mn, Mo, and Cu concentrations are higher in Unit IV relative to Unit III, indicating Zn and Fe removal from and Mn, Mo, and Cu liberation to the interstitial water. Concentrations of rubidium and cesium are well correlated with those of potassium, lithium, and strontium below Unit II (Fig. F22). Maxima of rubidium and cesium are observed at the base of Unit II. Concentrations of these elements decrease in Unit III, resulting from reaction with clay minerals as indicated by other major and minor cation profiles. Lead concentration is constant at greater depths, whereas uranium concentration shows an increase within Unit IV (Fig. F22). Uranium concentrations are sensitive to redox conditions and show a similar trend to that of Mn in this unit.

$\delta^{18}O$ and δD

Although overall variations of $\delta^{18}O$ and δD in Unit I are smaller than those at Site C0001 (Fig. F23), positive excursions are observed at depths where ion concentrations are diluted because of gas hydrate dissociation. Water molecules composing gas hydrates are enriched in ^{18}O and deuterium (D); therefore, more positive $\delta^{18}O$ and δD values are expected when gas hydrates dissociate during core recovery and sample handling. Trends in $\delta^{18}O$ and δD values with depth in Units II–IV are similar to those at Site C0001, likely resulting from pore water reactions with clay minerals.

Organic geochemistry

Hydrocarbon gas composition

Methane was the predominant hydrocarbon present in all Site C0002 cores. Concentrations of methane, ethane, and propane, along with methane to ethane ratios (C_1/C_2), are shown in Table T15. Ethane was detected in all samples, and propane was also detected in the lower part of Hole C0002B. Depth profiles of headspace methane, ethane, and propane are shown in Figure F24. Methane concentrations rapidly increase from 16.7 ppmv in the near-surface sample to 26,449 ppmv at 16.8 m CSF. In the deeper sections of Hole C0002D, concentrations decrease with depth. In Hole C0002B, methane concentrations remain constant from the top of the coring depth (476 m CSF) to 610 m CSF and increase with depth in the deeper part of Unit II. Methane concentrations decrease with depth in Unit III and increase

rapidly in the lower part of Unit IV. Ethane was not detected in Hole C0002D. The depth profile of ethane in Hole C0002B is similar to that of methane (Fig. F24). Below 1000 m CSF, propane is present in four samples, suggesting contribution of thermogenic origin. Thermogenic gas indicates diagenetic production of gas from older, more mature organic matter in the sediments or the migration of gas from greater depths. C_1/C_2 ratios range from 169 to 1868 (Fig. F25). Ratios remain constant at ~1000 above 900 m CSF. Below this depth, ratios gradually decrease with depth to the bottom of the hole. Ratios <1000 below 900 m CSF indicate some contribution of thermogenic hydrocarbons.

Sediment carbon, nitrogen, and sulfur composition

A total of 90 sediment samples were collected from Hole C0002B next to all whole-round samples for interstitial water and geotechnical tests. All samples were analyzed for inorganic carbon, total carbon, nitrogen, and sulfur (see "Organic geochemistry" in the "Expedition 315 methods" chapter for analytical procedures). Values of inorganic carbon, calcium carbonate ($CaCO_3$), total organic carbon (TOC), total nitrogen, organic carbon to total nitrogen (C/N) ratio, and total sulfur in the sediments are listed in Table T16 and presented in Figure F26.

Calcium carbonate content calculated from inorganic carbon content ranges from 0.66 to 22.98 wt% with an average of 7.28 wt%. Calcium carbonate concentrations are significantly higher in Unit III than in Units II and IV. The difference in concentrations between each unit may be related to the position relative to the CCD during deposition and dilution of biogenic carbonate by terrigenous silt and clay within the Kumano Basin.

TOC content ranges from 0.20 to 0.92 wt%. The depth profile of TOC shows scattered values with an average of 0.52 wt%. Total nitrogen content is similar in range to that found at Site C0001. All values for total nitrogen are <0.15 wt% and concentrations are constant throughout Hole C0002B. The depth profile of C/N ratios shows little variation with depth. C/N ratios range from 2.4 to 8.9 with an average of 5.5, suggesting that the organic matter was mainly derived from marine organisms.

Total sulfur content ranges from traceable amounts to 1.8 wt% with an average of 0.42 wt%. In Unit II, concentrations are fairly uniform. Sulfur concentrations increase with depth in Unit III and remain high with scattered values throughout Unit IV.

Microbiology

Sample information

A total of 63 whole-round cores were taken from Holes C0002B and C0002D for microbiological analysis. Table T17 shows the depths of the three types of whole-round cores. Some of the whole-round cores were subsampled on board for cell fixing, deoxyribonucleic acid (DNA) and ribonucleic acid (RNA) extraction, and culturing studies. Onboard work mainly included preserving whole-round cores and subsamples for shore-based work, fixing cells for cell detection, and counting and setting up sulfate-reducing bacteria enrichment cultures.

Cell detection with epifluorescence microscopy

Selected fixed cell samples were stained on board with double-stranded DNA-binding SYBR Green I stain. Cell counting was conducted on shore. Cells were detected in core samples to 1020 m CSF (Fig. F27). The number of cells ranges from 9.9×10^6 to 3.4×10^9 per cubic centimeter (Table T18). Some samples have a lot of matrix, which makes counting difficult. Cell abundance decreases drastically between samples at 58 and 79 m CSF and remains low in the sections below except for three samples at 203, 566, and 1020 m CSF. There is no clear relationship between geology and cell abundance.

Cultivation experiments

Enrichment cultures were established during Expedition 315 with the aim to culture sulfate-reducing microorganisms. Cultures were monitored for sulfate reduction based on the formation of black iron sulfide precipitate, which indicates production of biogenic hydrogen sulfide in the iron-containing medium. During the expedition, no blackening of the growth medium was observed in any of the cultures from Site C0002 because of the short incubation time (up to only 1 week, depending on the sample).

Physical properties

Porosity and density

At Site C0002, a total of 492 discrete samples were analyzed for MAD. Figure F28A shows porosity evolution at Site C0002 versus depth. Porosity from discrete samples decreases with depth in Unit I, and the average is 60.7%. Porosity decreases slightly with depth in Unit II, from ~50% at 480 m CSF to ~40% at 820 m CSF. Porosity increases slightly near the top of Unit III to ~40% and increases slightly with depth

within Unit III to ~42–43% at its base. In the upper ~100 m of Unit IV, porosity decreases with depth from values scattered between 31%–42% at its top to 28%–40% at 1020 m CSF but exhibits a trend of increasing porosity with depth between 1020 m CSF and the bottom of the hole.

Figure F28B shows bulk density on discrete samples and derived from MSCL measurements on whole-round cores (MSCL-W; see the "Expedition 315 methods" chapter for details). Bulk density of the discrete samples scatters between ~1.5 and 2.2 g/cm^3 throughout all the units. The bulk density trend mirrors that of porosity. In Unit I, density increases with depth (average = 1.67 g/cm^3). In Unit II, density increases slightly with depth (average = 1.95 g/cm^3) and then decreases with depth within Unit III (average = 2.00 g/cm^3). In Unit IV, density increases with depth above 1020 m CSF and then decreases with depth below 1020 m CSF. The average bulk density in this unit is 2.05 g/cm^3.

Figure F28C shows grain density at Hole C0002B versus depth. Average grain density in Unit I is 2.68 g/cm^3. Average grain density in Unit II is 2.68 g/cm^3 and increases slightly with depth. Grain densities in Unit III and IV are nearly constant with depth, with average values of 2.70 and 2.68 g/cm^3, respectively.

The observed discontinuities in porosity and bulk density (e.g., at the Unit III/IV boundary), as well as the reversal of the compaction trend within Unit IV (1020–1050 mbsf), may be explained by a variety of processes. As was the case for Site C0001, these fall into two categories, methodological and geological. There are two main methodological effects that can lead to overestimates of porosity: (1) hydrous minerals dehydrate during shipboard oven-drying (105°C for 24 h), leading to overestimates of porosity in zones with abundant opal or hydrous clays, and (2) drilling disturbance and remolding, despite the fact that samples were carefully chosen from relatively undisturbed portions of the core. There are also two geological processes that could affect porosity: (1) Sediment composition (mineralogical composition, grain size distribution, and degree and type of cementation) are known to affect sediment consolidation behavior, which could result in differences in porosity (and density) trends, and (2) tectonic compaction in the accretionary prism (Unit IV) could cause additional compaction consolidation, and therefore lower porosity than in Units II and III.

Shear strength

Results from penetrometer shear strength measurements are shown in Figure F29A. Shear strength data are highly scattered and do not show any significant trend. No reliable correlation with porosity could be found (Fig. F29B). Although sample depths at this site are deeper than those at Site C0001, shear strengths are significantly lower than those at Site C0001. RCB drilling may also induce a high degree of sample disturbance. Taking these possibilities into consideration, we consider all shear strength data from Hole C0002B to be unreliable.

Thermal conductivity

Thermal conductivity measurements were conducted on whole-round cores (<555.06 m CSF) with the needle probe and on split samples from cores from depths >562.27 m CSF with the half-space probe.

Thermal conductivity increases with depth in lithologic Units I and II to 645 m CSF. This increase may be fit with a linear regression:

$$k = 0.954 + (5.78 \times 10^{-4})z$$

with z in meters and k in W(m·K).

Below 645 m CSF, in lithologic Units II, III, and IV, thermal conductivity remains constant at 1.527 ± 0.083 W(m·K). The cause of the transition is unclear, as it does not correlate with a major lithologic change or with a discontinuity in MAD results. However, this depth corresponds to the depth at which it became possible to cut sample cubes for *P*-wave velocity and electrical conductivity measurements.

Color spectroscopy

Results from color reflectance measurements are presented in Figure F30. No significant difference in L*, a*, and b* values were observed throughout all the units. L* ranges from 30 to 50, a* ranges from –3 to 2, and b* ranges from 1 to 4.

Downhole temperature

In Hole C0002D, eight in situ temperature measurements were conducted with the APCT3 and six were successful. Best fit equilibrium temperatures and root mean square misfits are given in Table T19. Based on examination of the misfit function, uncertainty on the extrapolated equilibrium temperature is less than ±0.05°C for all measurements, except the first one (Core 315-C0002D-2H), which has a wider range of acceptable values from 2.6° to 3°C. Linear regression of all temperature data yields a gradient of 40°C/km (Fig. F31). Thermal resistance was computed by depth integration of measurement on cores down to 1047.2 m CSF with thermal conductivity data from Holes C0001B and C0001D. A mean square fit of temperature versus thermal resistance yields a heat

flow of 39.7 mW/m². The thermal conductivity in the data gap between 201.9 and 485 m was interpolated using the linear regression defined in the thermal conductivity subsection and temperatures extrapolated downhole assuming a 39.7 mW/m² constant heat flow (Fig. **F31**).

Discrete sample *P*-wave velocity and electrical conductivity

P-wave velocity and electrical conductivity were measured on discrete samples between 622.89 and 1051.32 m CSF. Measurements were performed in three orthogonal directions on cubes. Data tables are given as a supplementary material (see C0002_DS_VP_EC.XLS in 315_PHYS_PROPS in **"Supplementary material"**). Cubes were generally taken such that cube axes *x, y,* and *z* correspond to the core referential. There were, however, a few exceptions, noted on the log sheets, when dipping beds were recognized (see the **"Expedition 315 methods"** chapter). Overall, electrical conductivity decreases with depth (Fig. **F32A**), but a reversed trend is observed between 987.61 m and 1051.32 m CSF. Porosity also increases in this interval. However, *P*-wave velocity (V_P) increases in this interval (Fig. **F32A**). This suggests that the increase in porosity and conductivity is more likely caused by intrinsic sediment properties than by a reversed consolidation trend. *P*-wave velocity could only be measured on four samples in the uppermost part of lithologic Unit IV, from 930 to 1000 m CSF, and these values are remarkably scattered, ranging from 1840 to 5550 m/s. The 5550 m/s value was measured on a hard sandstone piece, which is not representative of the formation. However, the *P*-wave measurements obtained on these four samples suggests the high reflectivity of the top of the old accretionary complex on the seismic profile may be due to high impedance contrasts at short wavelengths. Electrical conductivity and *P*-wave velocity is systematically lower in the *z*-direction than in the *x*- and *y*-directions in lithologic Units II and III. This anisotropy is presumably caused by compaction in the forearc basin. As was observed at Site C0001, the difference between measurements in *z*- versus *x*- and *y*- directions is relatively smaller in the accretionary wedge (Unit IV). This may result from a more complex strain history in the accretionary wedge than in the slope and forearc basin sediments. Understanding the anisotropy signal requires post-cruise paleomagnetic reorientation of all samples. Samples are currently stored at Kochi core center.

Core-log-seismic integration

Hole C0002B is located 60 m south-southwest of Hole C0002A, a LWD hole drilled during Expedition 314. Three stratigraphic sequences are seen on the seismic profile (Inline 2529) in Figure **F33.** The forearc basin sequence from Hole C0002B toward Hole C0002A has a northwest dip of 6.5° to 7.0° in the lower half of lithologic Unit II, so a stratigraphic offset of 6.0 to 7.5 m is expected between the boreholes. Dips are nearly constant down to an unconformity within lithologic Unit III observed at 890 mbsf (2827 mbsl), well within lithologic Unit III. A strong reflector at ~950 mbsf (2887.5 mbsl) marks the main angular unconformity between sandy accreted sediments below and muddy slope or forearc-basin deposits above. The equivalent boundary between logging Units III and IV is positioned at 935.6 m LSF. Seismic reflectors dipping 30°–40° are observed below the main unconformity. Dips cannot be determined from the seismic image in the interval between the unconformities.

Correlation between natural gamma ray intensity from LWD and MSCL-W is limited by overall poor recovery and core quality in the turbidite sequences constituting lithologic Unit II and around the main unconformity (Fig. **F34**). Intervals where sand layers are thicker and more abundant can be identified from strong short-wavelength cycles in the gamma ray logs and correlate with intervals of very low core recovery at 418–435 and 773–825 m CSF. Oscillation of LWD gamma ray intensity with a wavelength of ~60 m may tentatively be correlated with the core logs, but only broad maxima around 550 and 735 m CSF are well identified in the core data. Lithologic Unit III provides core logs of sufficient quality to allow peak-to-peak correlations of shorter wavelengths, but the proposed solution is not unique (Fig. **F34**). Overall, these observations are consistent with a systematic deepening of forearc basin strata of 5 to 15 m from Hole C0002B to Hole C0002A (Table **T20**).

In Hole C0002B, density, sonic, and resistivity logs can be compared with measurements on samples. In Figure **F35,** LWD bit resistivity is compared with temperature-corrected sample resistivity and LWD gamma ray density is compared with sample density from moisture and density measurements.

For an accurate comparison with LWD bit resistivity, which averages horizontal and vertical conductivities over a rock volume, an average sample resistivity is computed as the geometric average of resistivities measured in horizontal plane and along the vertical axis. Horizontal plane electrical resistivity is computed from the mean of two complex conductivity measurements made in the horizontal plane at a 90° angle. As at Site C0001, a correction for in situ temperature is applied assuming the resistivity of the samples varies in the same way as that of seawater (Bourlange et al., 2003):

$$R\ (T,°C) = R\ (25°C)/[1 + 0.02(T - 25)].$$

The temperature at a given depth is computed based on the heat flow determination (40 mW/m^2) and thermal conductivity measurements on cores made during this expedition (see **"Physical properties"**).

P-wave velocity measured on samples is lower than in situ *P*-wave velocity from LWD but follows the same trends (Fig. **F36**). The same corrections are applied for in situ conditions as at Site C0001; a 2.4% correction is applied to account for the variation of the *P*-wave velocity of seawater between the sea surface and 2200 m depth (Fofonoff, 1985) and an additional empirical correction of 1% per 100 mbsf is applied to account for the effect of confining pressure. Agreement between corrected *P*-wave velocity measured along the core axis and LWD *P*-wave velocity is satisfactory.

The zone around the lower unconformity is characterized by strong heterogeneity of physical properties according to the logs. Two intervals, presumably sand dominant, display both low natural gamma ray intensity and low resistivity on the logs, in part because of hole caving. These inferred sandy intervals were not recovered in cores. Cores 315-C0002B-51R and 52R (938.50–949.24 m CSF) likely correspond to a higher natural gamma ray and resistivity interval between 950 and 960 m LSF. Below this level, Cores 315-C0002X-53R and 54R were empty and, unfortunately, correspond to the depth of the reflector marking the main seismic unconformity (Fig. **F37**). Recovery remained low, with highly fractured and disturbed cores through Core 315-C0002B-59R. Brecciation of lithified materials (one sandstone sample from Core 312-C0002B-57R has a *P*-wave velocity of 5.5 km/s) should cause strong local impedance contrasts and seismic reflectivity.

In the lower part of Unit II, in addition to the correlation of gamma ray values, electrical resistivity and porosity suggest deepening from Hole C0002B to Hole C0002A. Notably, a V-shaped minimum in resistivity and density is found at 914 m CSF in the cores and at 925 m LSF in the logs and is consistent with an 11–12 m offset inferred independently from the gamma ray data alone (Fig. **F35**).

A trend of decreasing density and resistivity with depth is observed on samples from 1010.9 to 1042.7 m CSF (0.0055 Ωm/m). This trend may correlate with a similar trend in LWD resistivity (0.008 Ωm/m) observed between 980 and 1005 m LSF. A stratigraphic offset of 30–40 m between the boreholes would be compatible with the observed dip of reflectors within the accreted sediments, as well as with the dips observed in the cores. No strong arguments against this interpretation can be found in the natural gamma ray intensity data (Fig. **F35**).

References

Borowski, W.S., Paull, C.K., and Ussler, W., III, 1996. Marine pore-water sulfate profiles indicate in situ methane flux from underlying gas hydrate. *Geology,* 24(7):655–658. **doi:10.1130/0091-7613(1996)024<0655:MPWSPI>2.3.CO;2**

Bourlange, S., Henry, P., Moore, J.C., Mikada, H., and Klaus, A., 2003. Fracture porosity in the décollement zone of Nankai accretionary wedge using logging-while-drilling resistivity data. *Earth Planet. Sci. Lett.,* 209(1–2):103–112. **doi:10.1016/S0012-821X(03)00082-7**

Brothers, R.J., Kemp, A.E.S., and Maltman, A.J., 1996. Mechanical development of vein structures due to the passage of earthquake waves through poorly consolidated sediments. *Tectonophysics,* 260(4):227–244. **doi:10.1016/0040-1951(96)00088-1**

Fofonoff, N.P., 1985. Physical properties of seawater: a new salinity scale and equation of state for seawater. *J. Geophys. Res.,* 90(C2):3332–3342. **doi:10.1029/JC090iC02p03332**

Gradstein, F.M., Ogg, J.G., and Smith, A. (Eds.), 2004. *A Geologic Time Scale 2004:* Cambridge (Cambridge Univ. Press). **http://www.stratigraphy.org/**

Hesse, R., 2003. Pore water anomalies of submarine gas-hydrate zones as tool to assess hydrate abundance and distribution in the subsurface—what have we learned in the past decade? *Earth-Sci. Rev.,* 61(1–2):149–179. **doi:10.1016/S0012-8252(02)00117-4**

Ogawa, Y., and Miyata, Y., 1985. Vein structure and its deformational history in the sedimentary rocks of the Middle America Trench slope off Guatemala, Deep Sea Drilling Project Leg 84. *In* von Huene, R., Aubouin, J., et al., *Init. Repts. DSDP,* 84: Washington, DC (U.S. Govt. Printing Office), 811–829. **doi:10.2973/dsdp.proc.84.136.1985**

Ogawa, Y., Ashi, J., and Fujioka, K., 1992. Vein structures and their tectonic implications for the development of the Izu-Bonin forearc, Leg 126. *In* Taylor, B., Fujioka, K., et al., *Proc. ODP, Sci. Results,* 126: College Station, TX (Ocean Drilling Program), 195–207. **doi:10.2973/odp.proc.sr.126.128.1992**

Lindsley-Griffin, N., Kemp, A., and Swartz, J.F., 1990. Vein structures of the Peru margin, Leg 112. *In* Suess, E., von Huene, R., et al., *Proc. ODP, Sci. Results,* 112: College Station, TX (Ocean Drilling Program), 3–16. **doi:10.2973/odp.proc.sr.112.130.1990**

Moore, G.F., Taira, A., Klaus, A., et al., 2001. *Proc. ODP, Init. Repts.,* 190: College Station, TX (Ocean Drilling Program). **doi:10.2973/odp.proc.ir.190.2001**

Pickering, K.T., Agar, S.M., and Prior, D.J., 1990. Vein structure and the role of pore fluids in early wet-sediment deformation, late Miocene volcaniclastic rocks, Miura Group, SE Japan. *In* Knipe, R.J., and Rutter, E.H. (Eds.), *Deformation Mechanisms, Rheology and Tectonics*. Geol.

Soc. Spec. Publ., 54(1):417–430. **doi:10.1144/GSL.SP.1990.054.01.38**

Pickering, K.T., Underwood, M.B., and Taira, A., 1993b. Stratigraphic synthesis of the DSDP-ODP sites in the Shikoku Basin, Nankai Trough, and accretionary prism. *In* Hill, I.A., Taira, A., Firth, J.V., et al., *Proc. ODP, Sci. Results,* 131: College Station, TX (Ocean Drilling Program), 313–330. **doi:10.2973/odp.proc.sr.131.135.1993**

Reeburgh, W.S., 1976. Methane consumption in Cariaco Trench waters and sediments. *Earth Planet. Sci. Lett.,* 28(3):337–344. **doi:10.1016/0012-821X(76)90195-3**

Shipboard Scientific Party, 2001a. Site 1175. *In* Moore, G.F., Taira, A., Klaus, A., et al., *Proc. ODP, Init. Repts.,* 190: College Station, TX (Ocean Drilling Program), 1–92. **doi:10.2973/odp.proc.ir.190.106.2001**

Shipboard Scientific Party, 2001b. Site 1176. *In* Moore, G.F., Taira, A., Klaus, A., et al., *Proc. ODP, Init. Repts.,* 190: College Station, TX (Ocean Drilling Program), 1–80. **doi:10.2973/odp.proc.ir.190.107.2001**

Underwood, M.B., Moore, G.F., Taira, A., Klaus, A., Wilson, M.E.J., Fergusson, C.L., Hirano, S., Steurer, J., and the Leg 190 Shipboard Scientific Party, 2003. Sedimentary and tectonic evolution of a trench-slope basin in the Nankai subduction zone of southwest Japan. *J. Sediment. Res.,* 73(4):589–602. **doi:10.1306/092002730589**

Zijderveld, J.D.A., 1967. AC demagnetization of rocks: analysis of results. *In* Collinson, D.W., Creer, K.M., and Runcorn, S.K. (Eds.), *Methods in Palaeomagnetism:* New York (Elsevier), 254–286.

Publication: 5 March 2009
MS 314315316-124

Figure F1. 3-D seismic inline section showing location of Site C0002. BSR = bottom-simulating reflector. VE = vertical exaggeration.

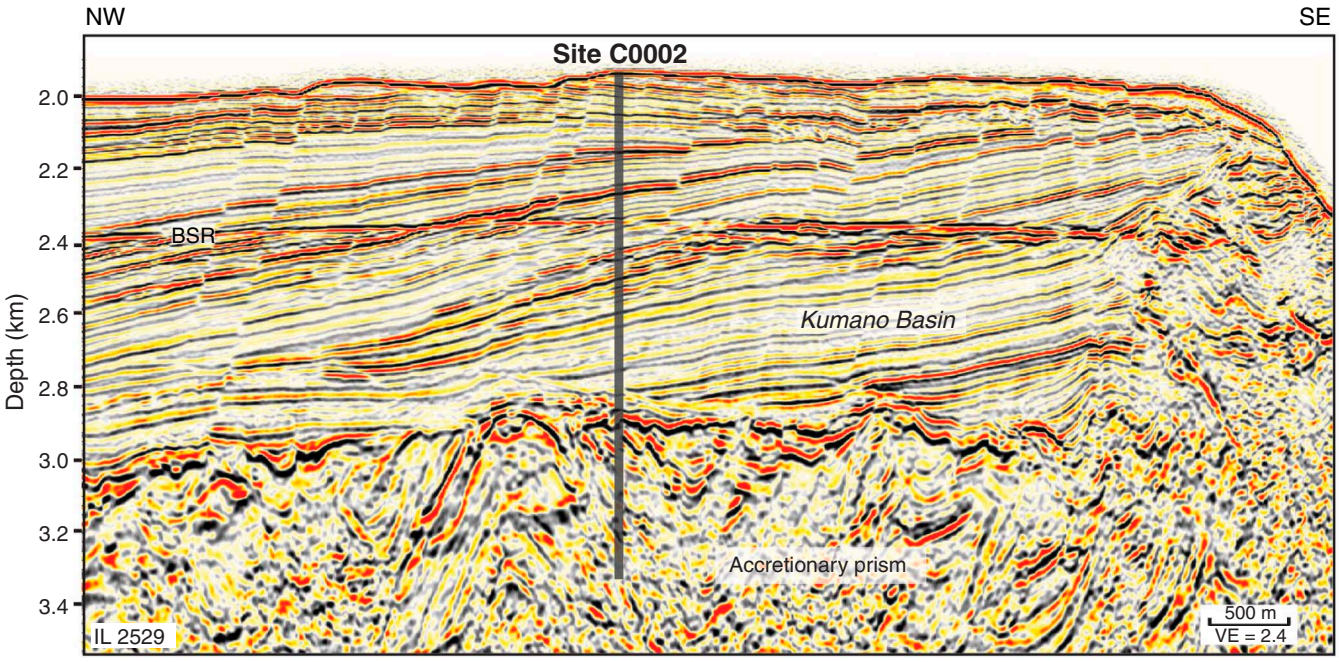

Figure F2. 3-D seismic cross-line section showing location of Site C0002. VE = vertical exaggeration.

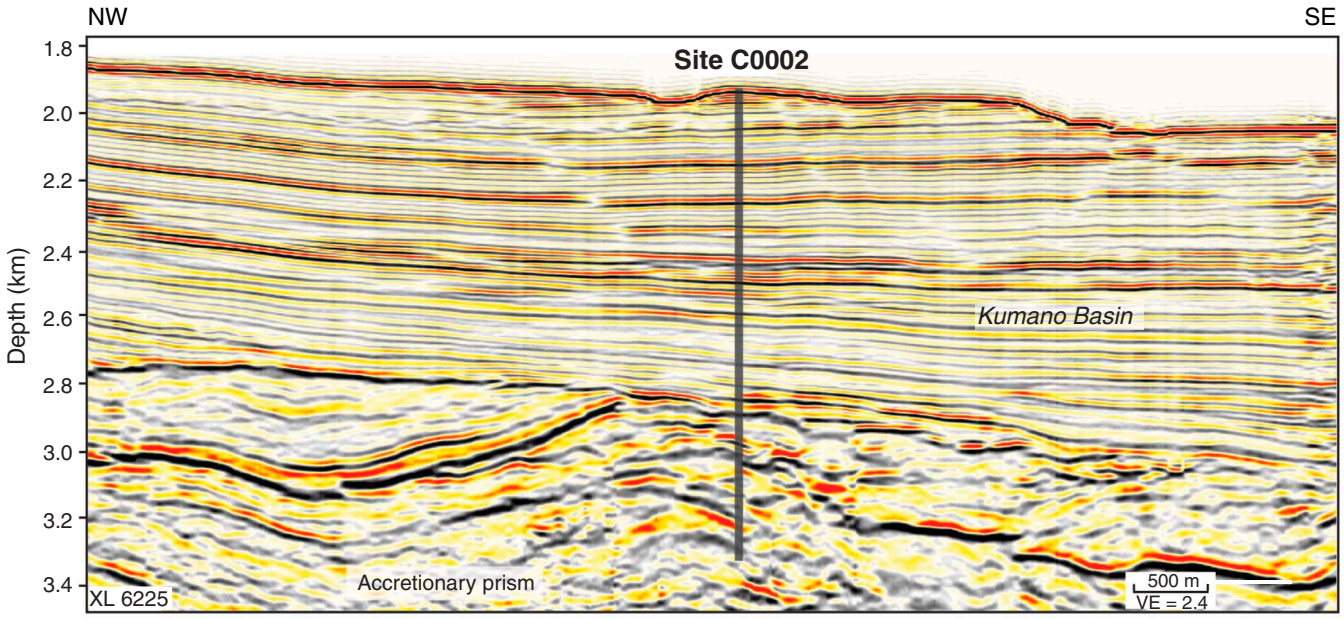

Figure F3. Locations of drill holes, Site C0002. Solid lines = seismic profile coverage.

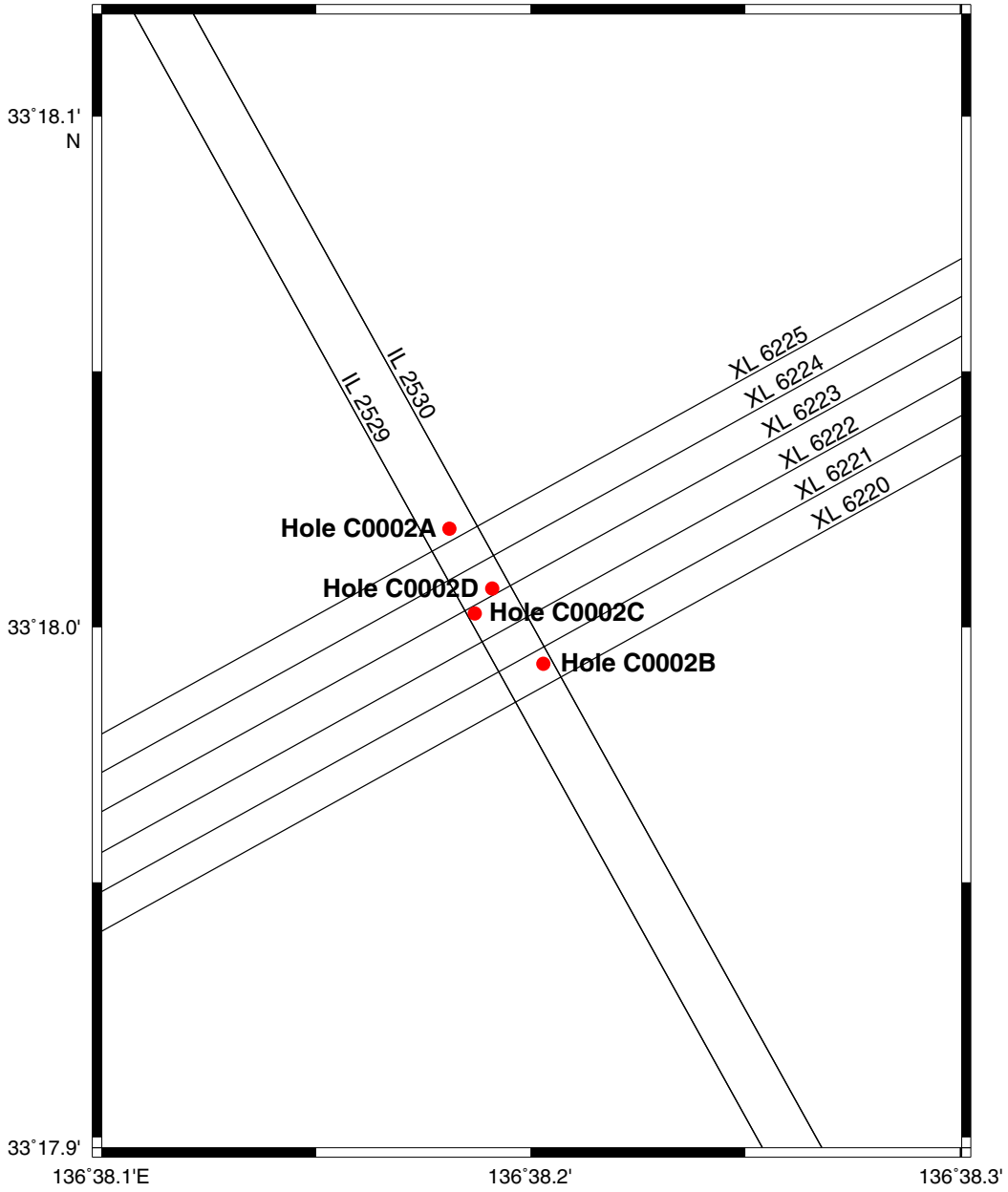

Figure F4. Lithology, Site C0002. CSF = core depth below seafloor.

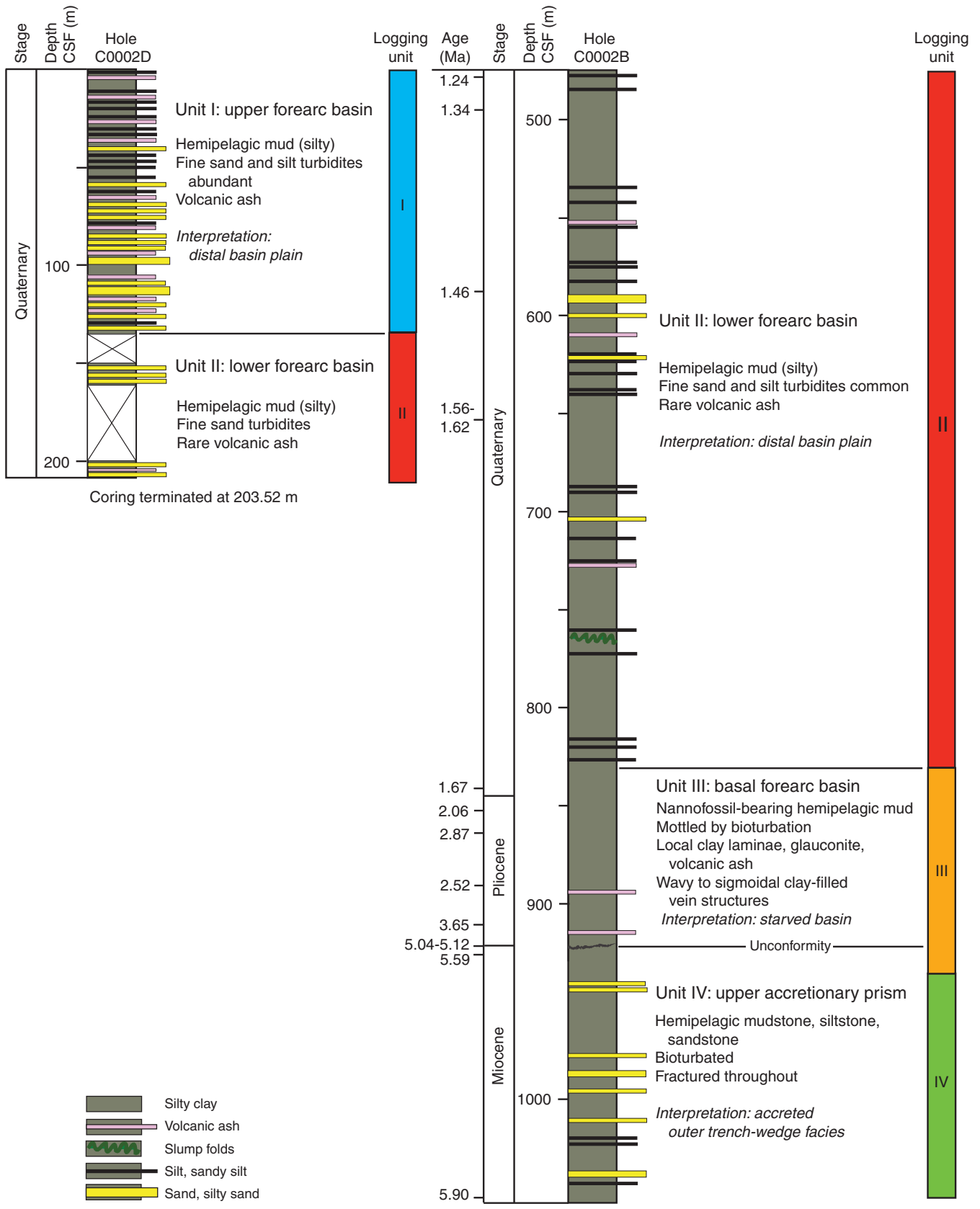

Figure F5. Bulk powder XRD, Site C0002. CSF = core depth below seafloor.

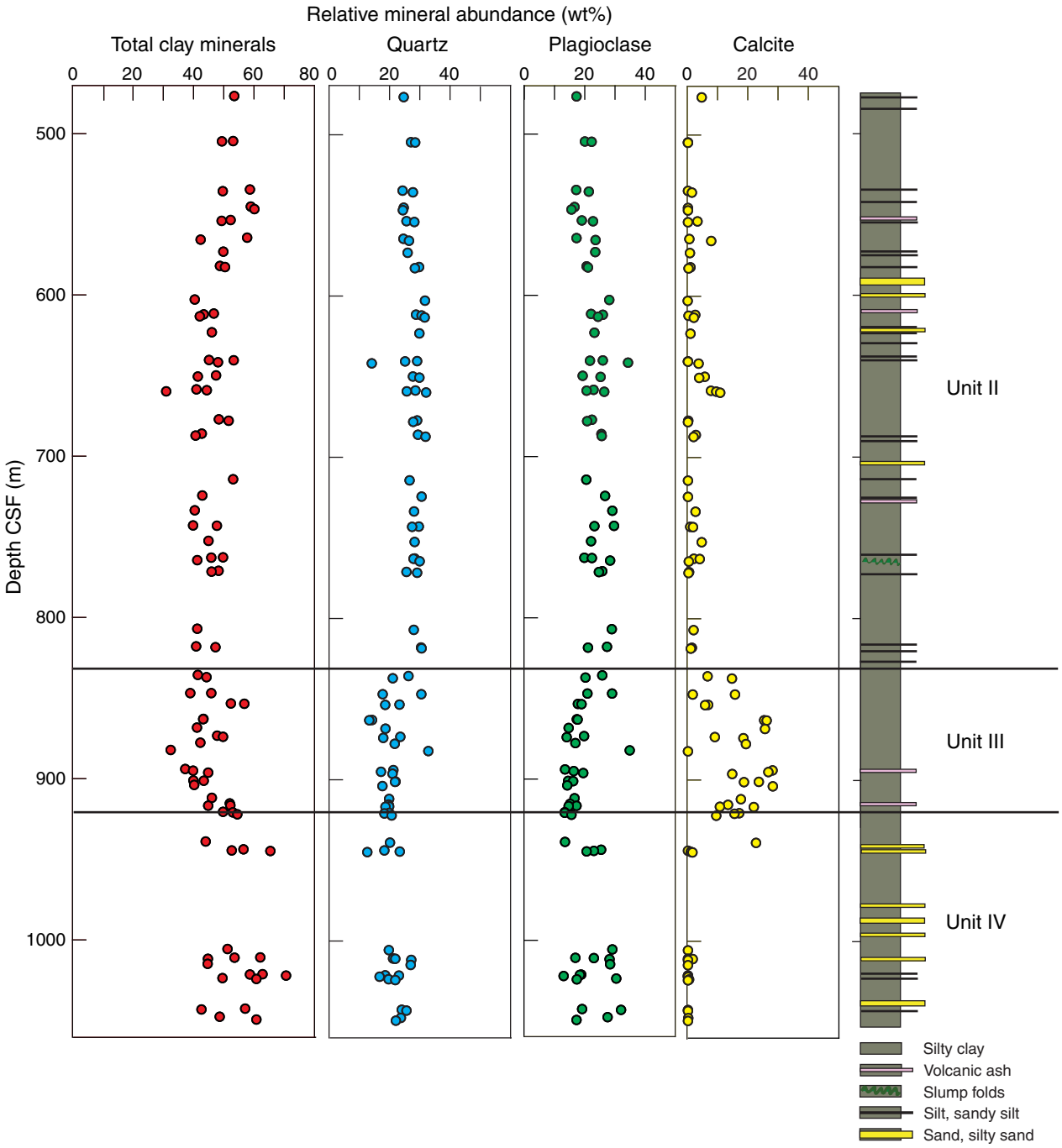

Figure F6. X-ray diffraction (XRD) calcite vs. coulometric carbonate, Site C0002. Dashed line = 1:1 correlation, solid line = best-fit linear regression.

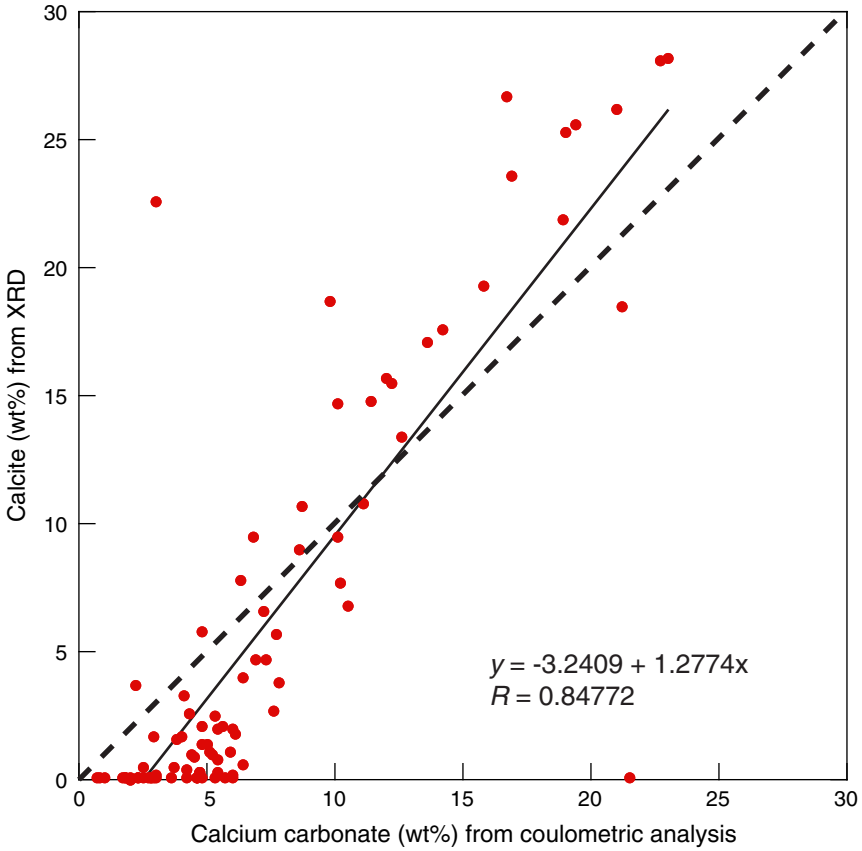

Figure F7. Photographs of deformation structures, Site C0002. **A.** Steeply dipping bedding and a crosscutting shear zone (Sample 315-C0002B-61R-4, 10–17 cm). **B.** Faults and breccia (Sample 315-C0002B-62R-1, 5–25 cm). **C.** Stratal disruption. **D.** Vein structures (right) and a shear zone (Sample 315-C0002B-45R-3, 93–104 cm).

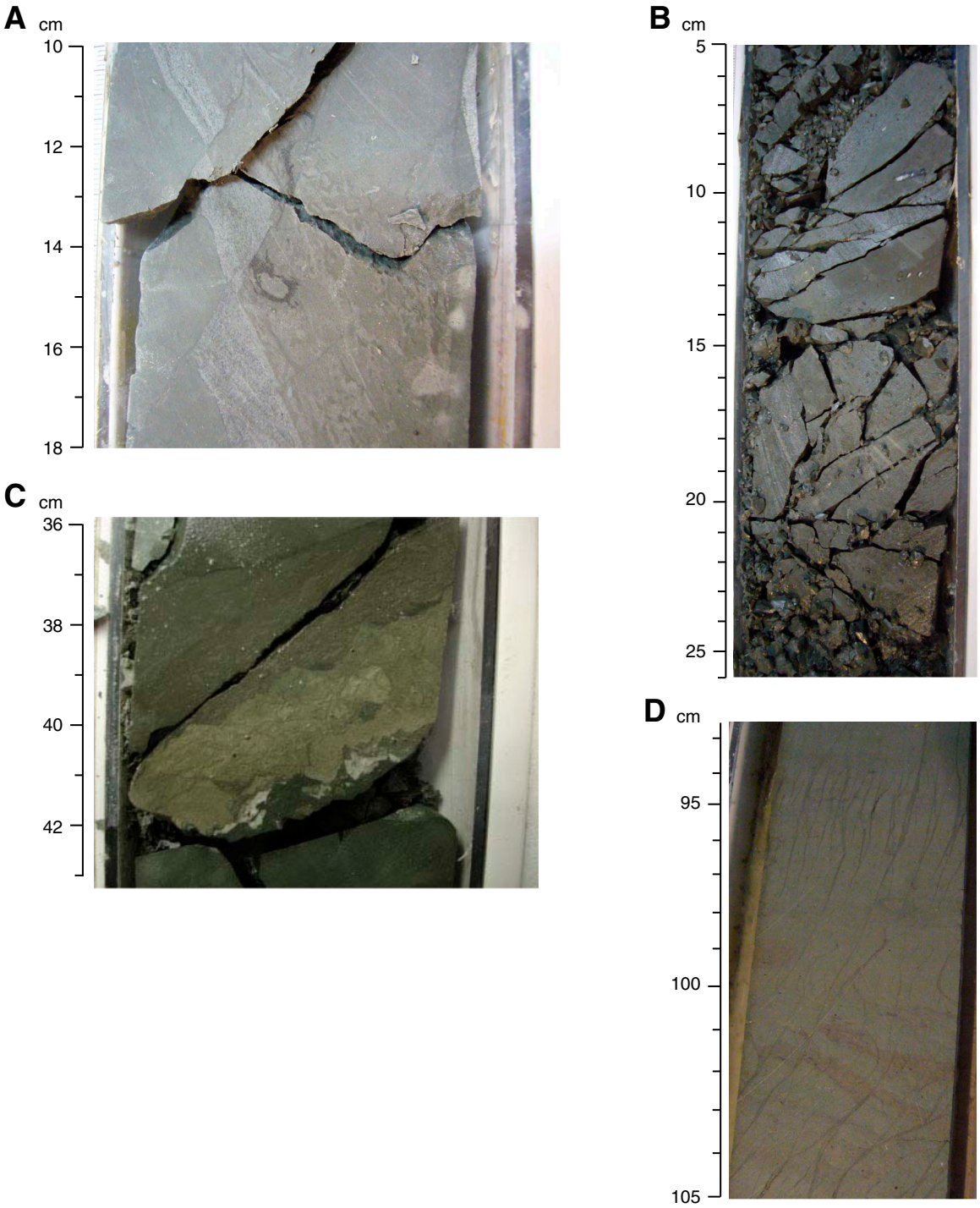

Figure F8. Dip angle of bedding, fissility, faults, and shear zones, Site C0002. Numbers of vein structures with depth are shown per 10 m. CSF = core depth below seafloor.

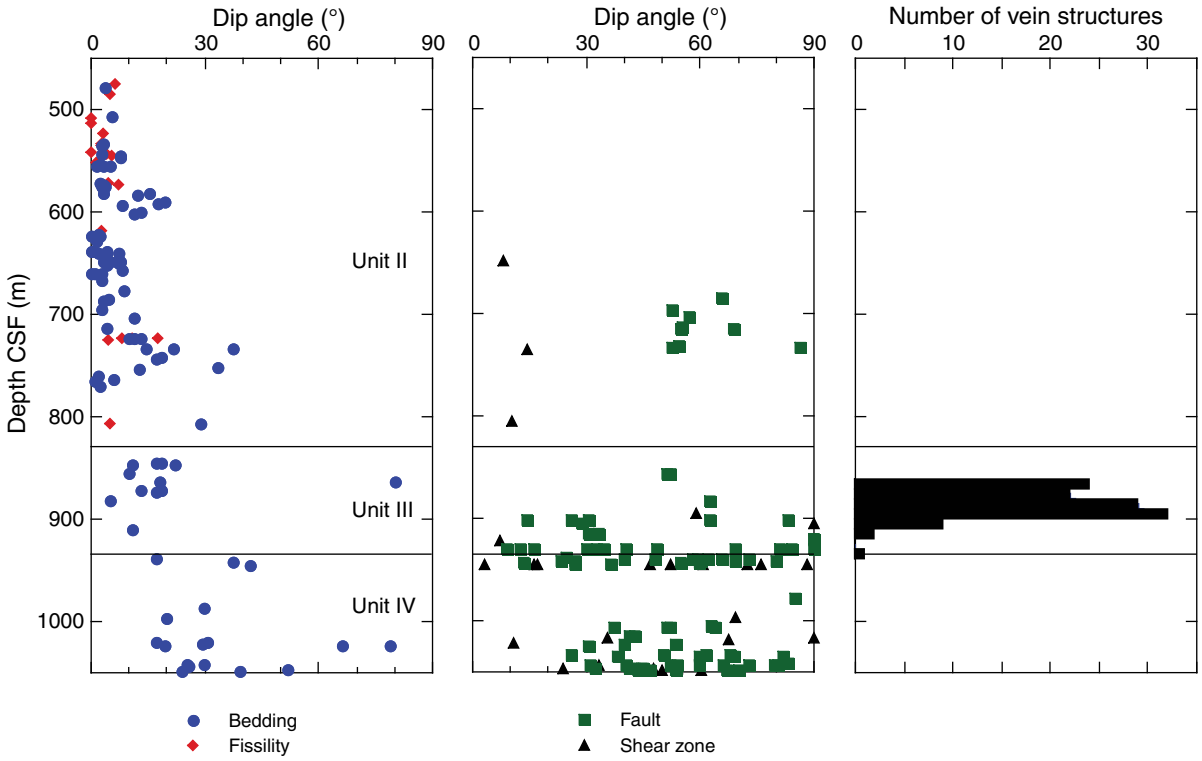

Figure F9. Dip angle of bedding, Site C0002. **A.** Hole C0002D. **B.** Site C0002 (entire section). CSF-B = core depth below seafloor, IODP Method B (see the **"Expedition 315 methods"** chapter).

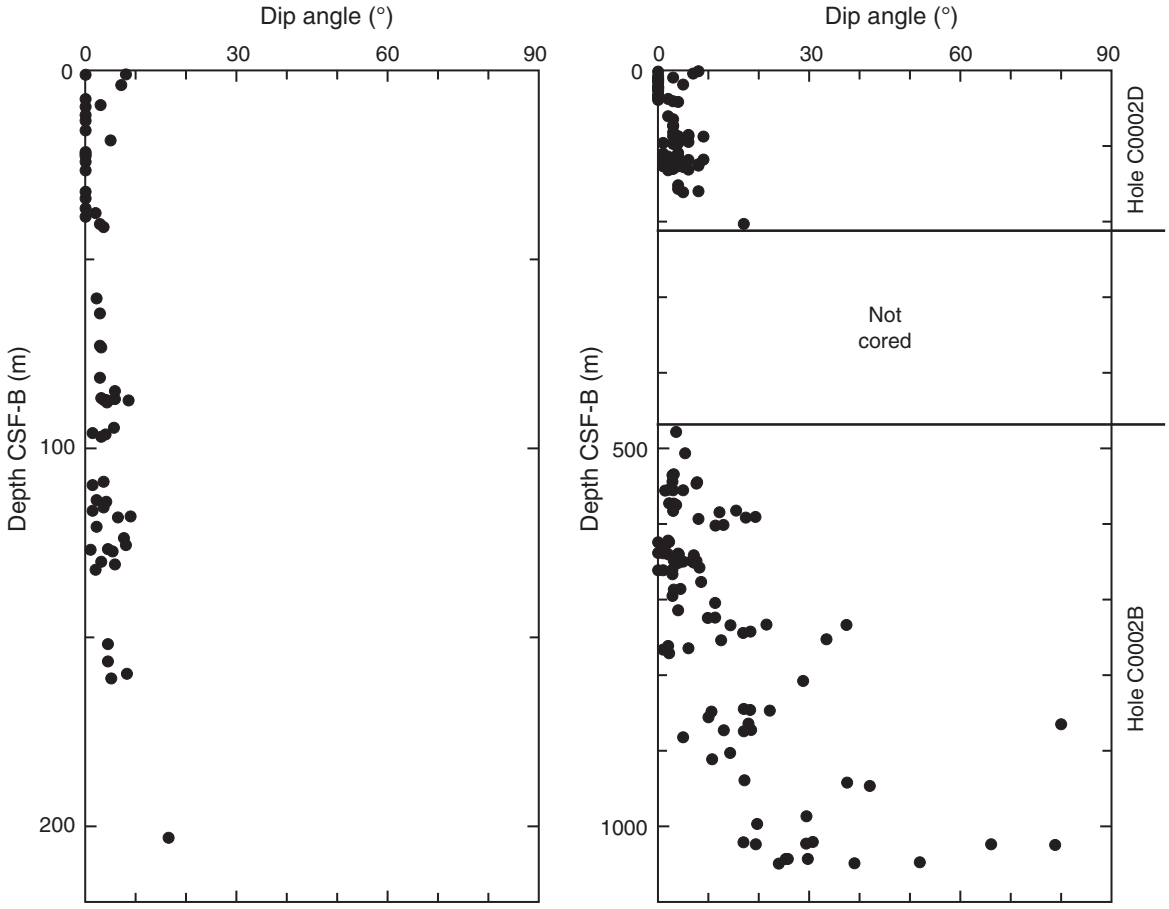

Figure F10. Lower hemisphere, equal area projections of poles to bedding.

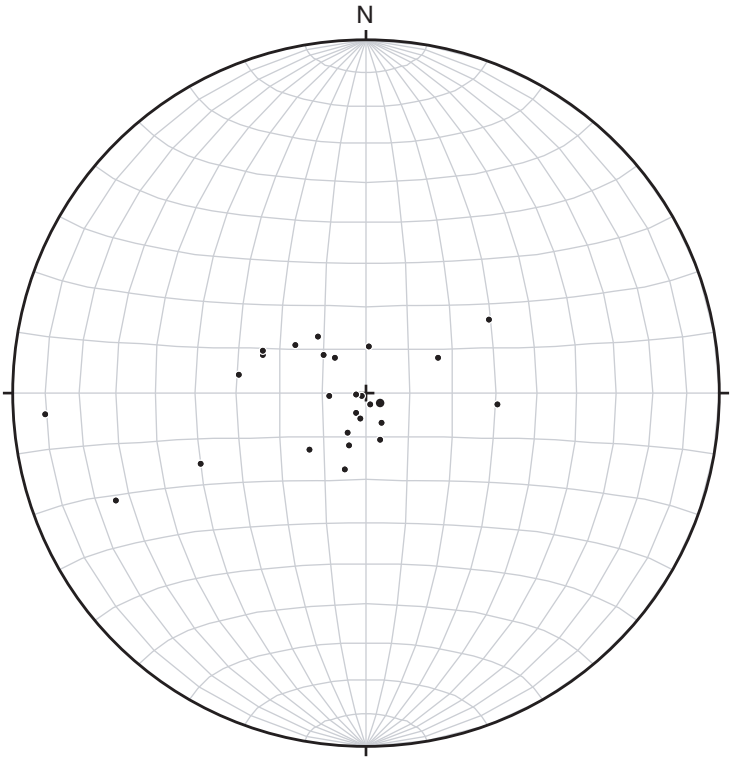

Figure F11. Lower hemisphere, equal area projections of normal faults. **A.** Fault planes (great circles) with striae (dots) and slip vectors (arrows) of hanging walls relative to footwalls. Black dots and arrows = data with slickenlines, red dots and arrows = slip directions assumed in dip directions and slip vectors inferred from offset. **B.** Kinematic solution for populations of normal faults shown in A with compressional (transparent) and associated extensional (gray shaded) quadrants.

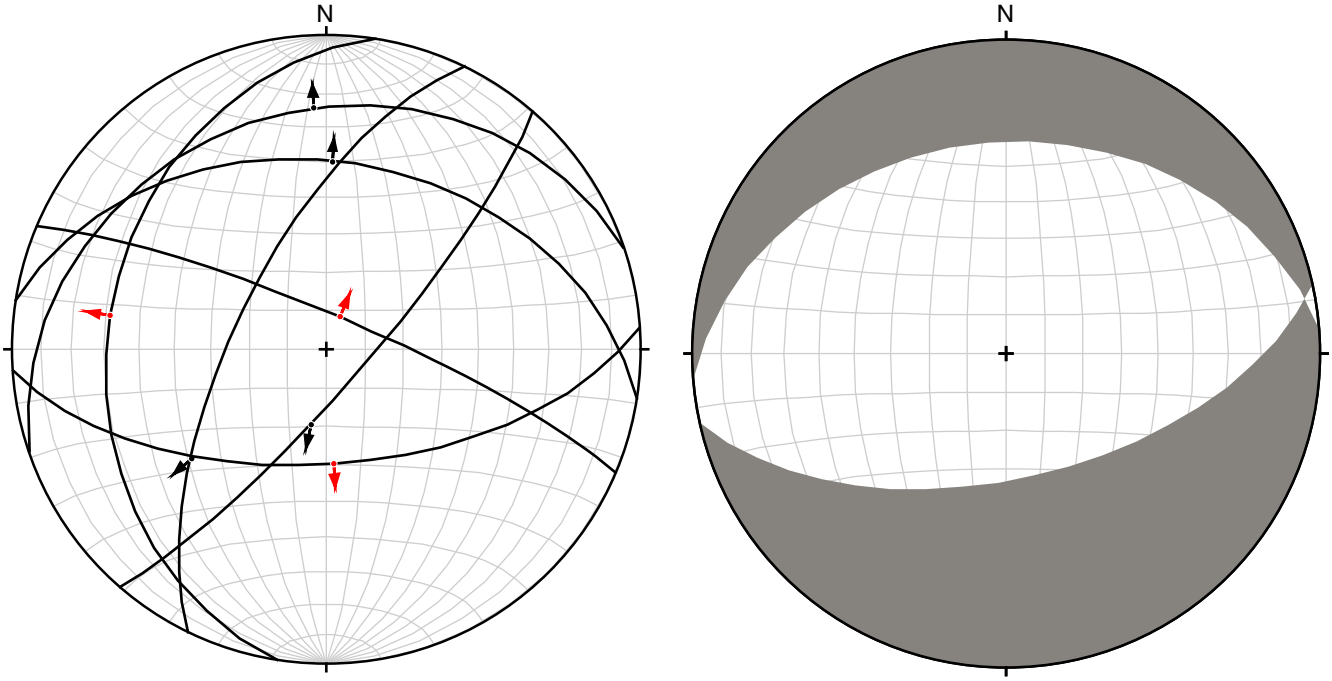

Figure F12. Lower-hemisphere, equal-area projections of shear zone planes. **A.** Red = planes (great circles) with observed normal offsets, black = planes with no observable offset. **B.** Kinematics for shear zones with observed offset in A with compressional (transparent) and associated extensional (gray shaded) quadrants; slip vectors are assumed to be down dip.

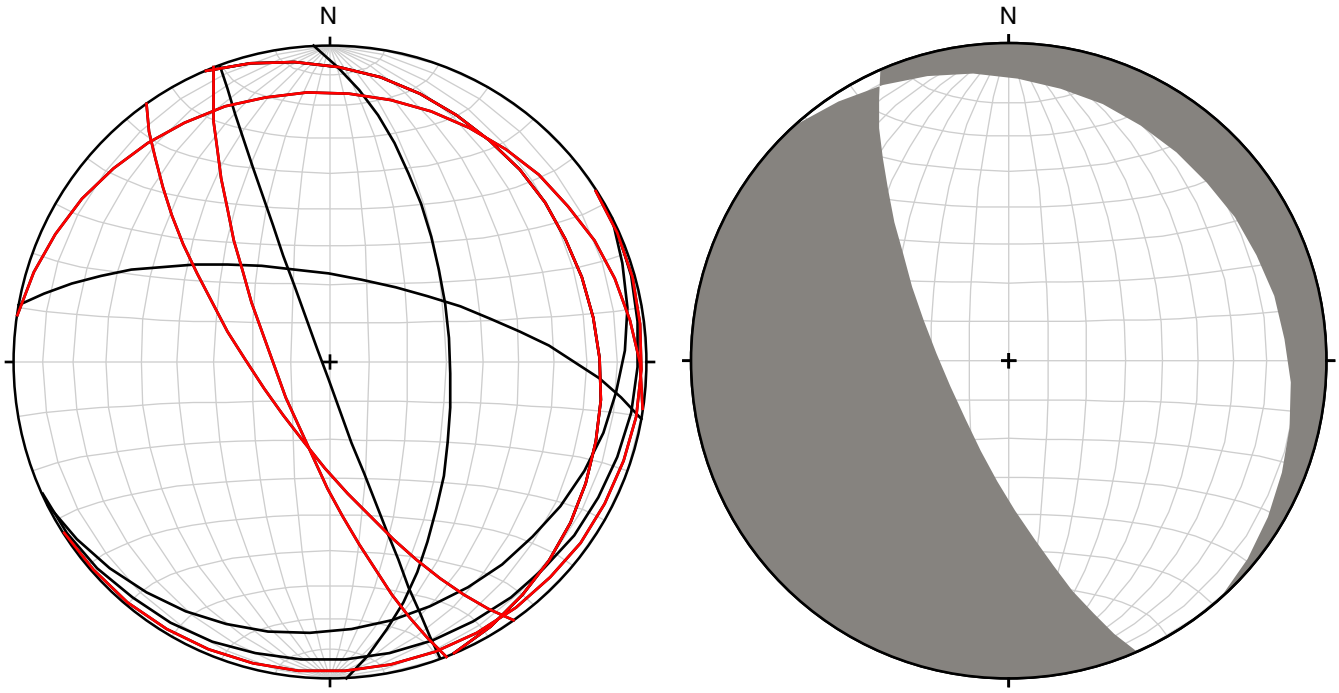

Figure F13. Lower hemisphere, equal area projections of fault planes with thrust and strike-slip displacements. **A.** Fault planes (great circles) with striae (dots) and slip vectors (arrows) of hanging walls relative to footwalls. **B.** Kinematics for populations of faults shown in A with compressional (transparent) and associated extensional (gray shaded) quadrants.

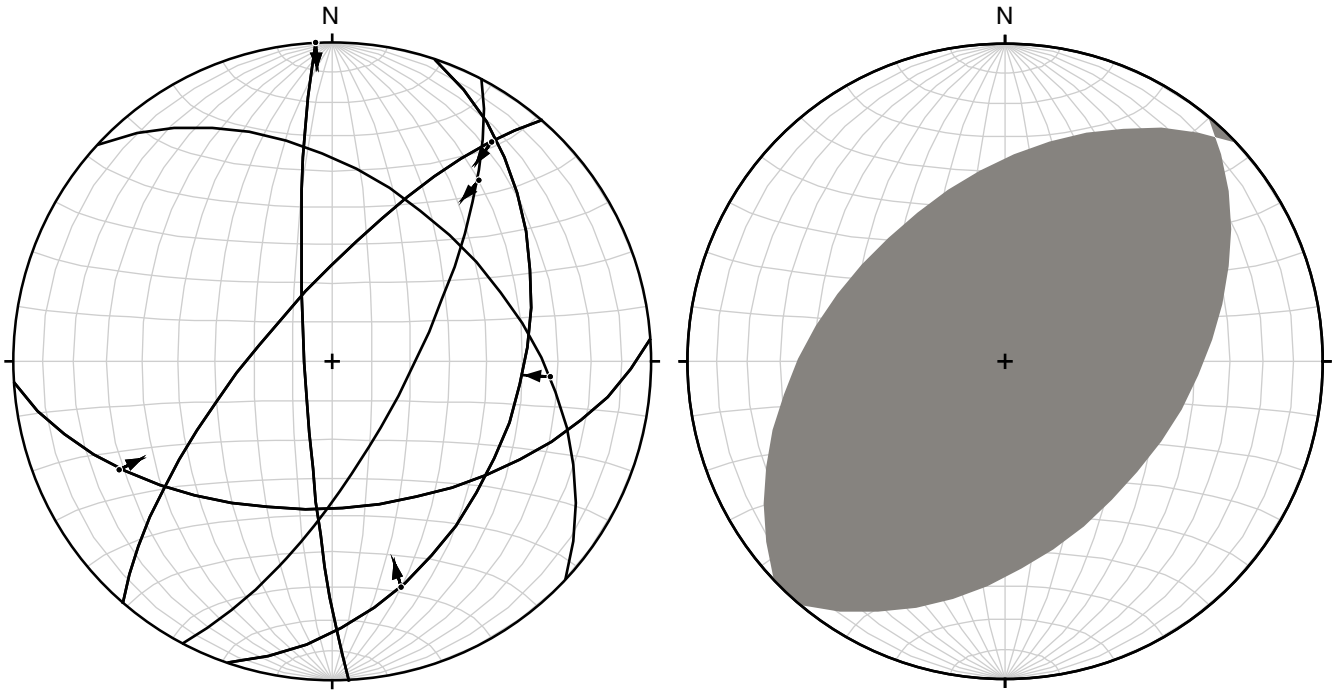

Figure F14. Biostratigraphic age model, Site C0002.

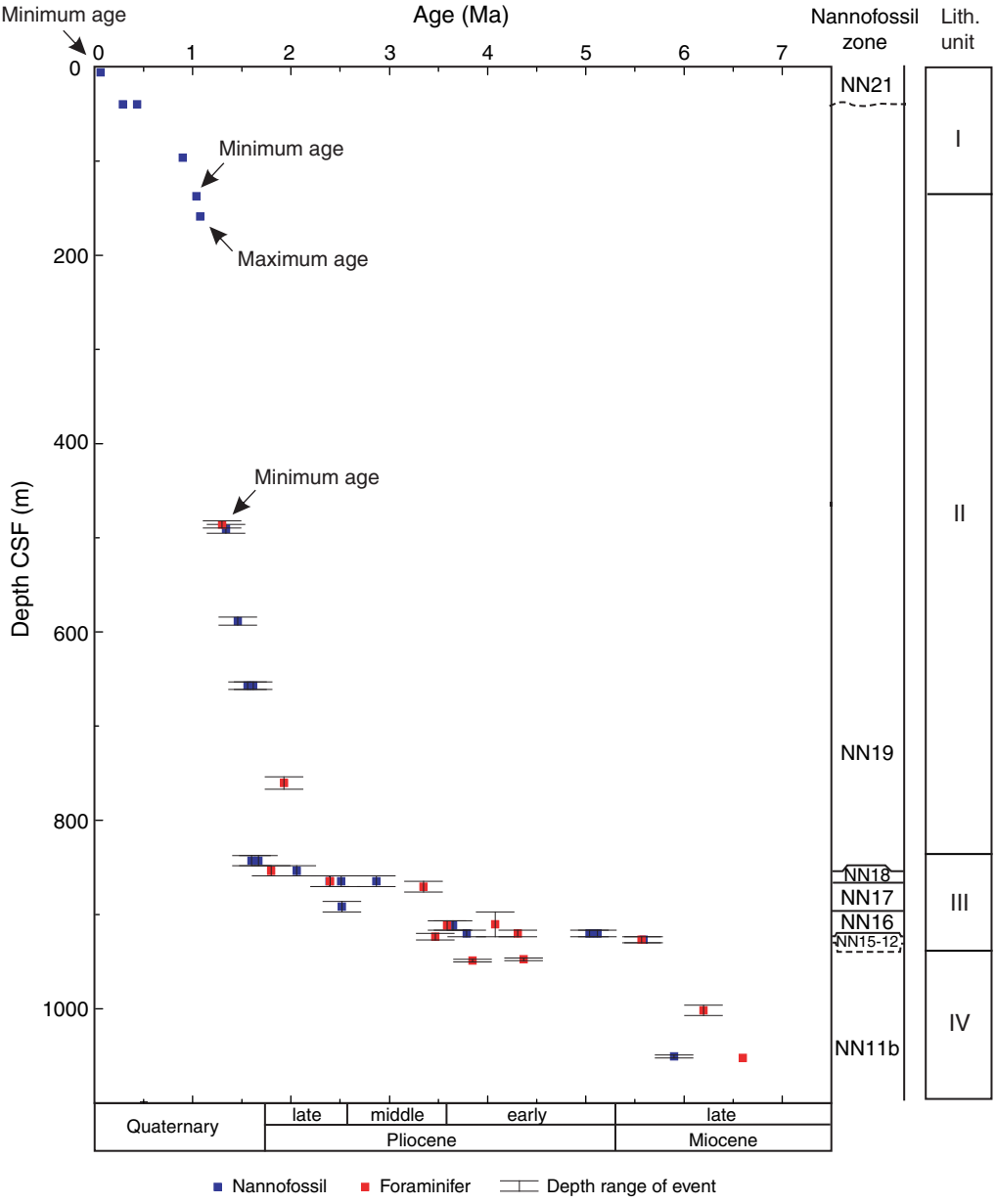

Figure F15. Declination, inclination, and intensity profiles at 30 mT in the demagnetized level of Hole C0002B. CSF = core depth below seafloor.

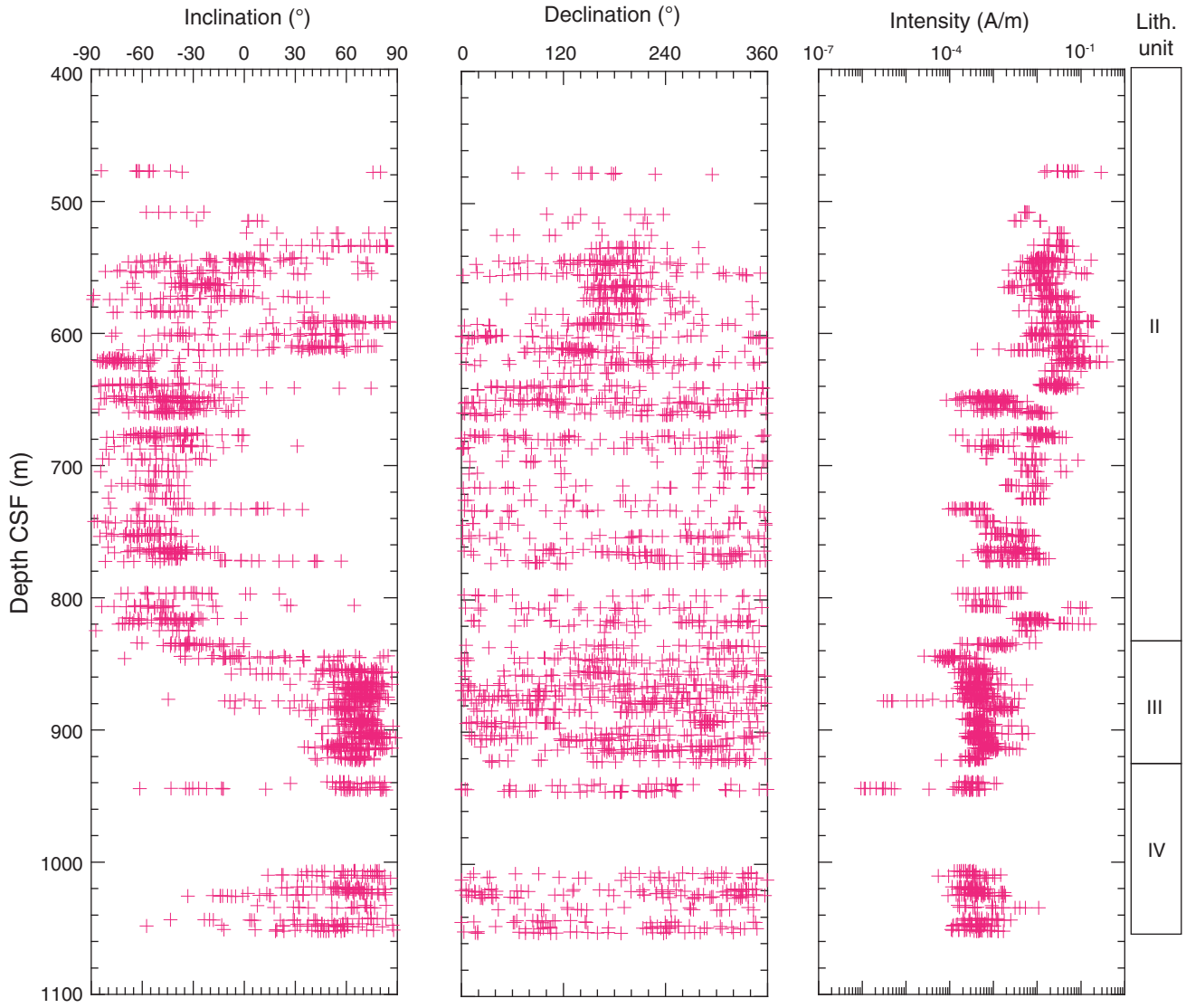

Figure F16. Results of progressive alternating-field demagnetization displayed by vector end-point diagram (Zijderveld, 1967) of representative samples. **A.** Sample 315-C0002B-20R-5, 15 cm. Demagnetization steps = 0, 5, 10, 15, 20, 25, and 30 mT. **B.** Sample 315-C0002B-27R-1, 55 cm. Demagnetization steps = 0, 5, 10, 15, 20, 25, and 30 mT. **C.** Sample 315-C0002D-2H-2, 5–7 cm. Demagnetization steps = 0, 5, 10, 15, 20, 25, 30, 40, 50, and 60 mT. Data points = magnetization vector for individual demagnetization steps projected onto horizontal (solid circle) and vertical (open circle) plane.

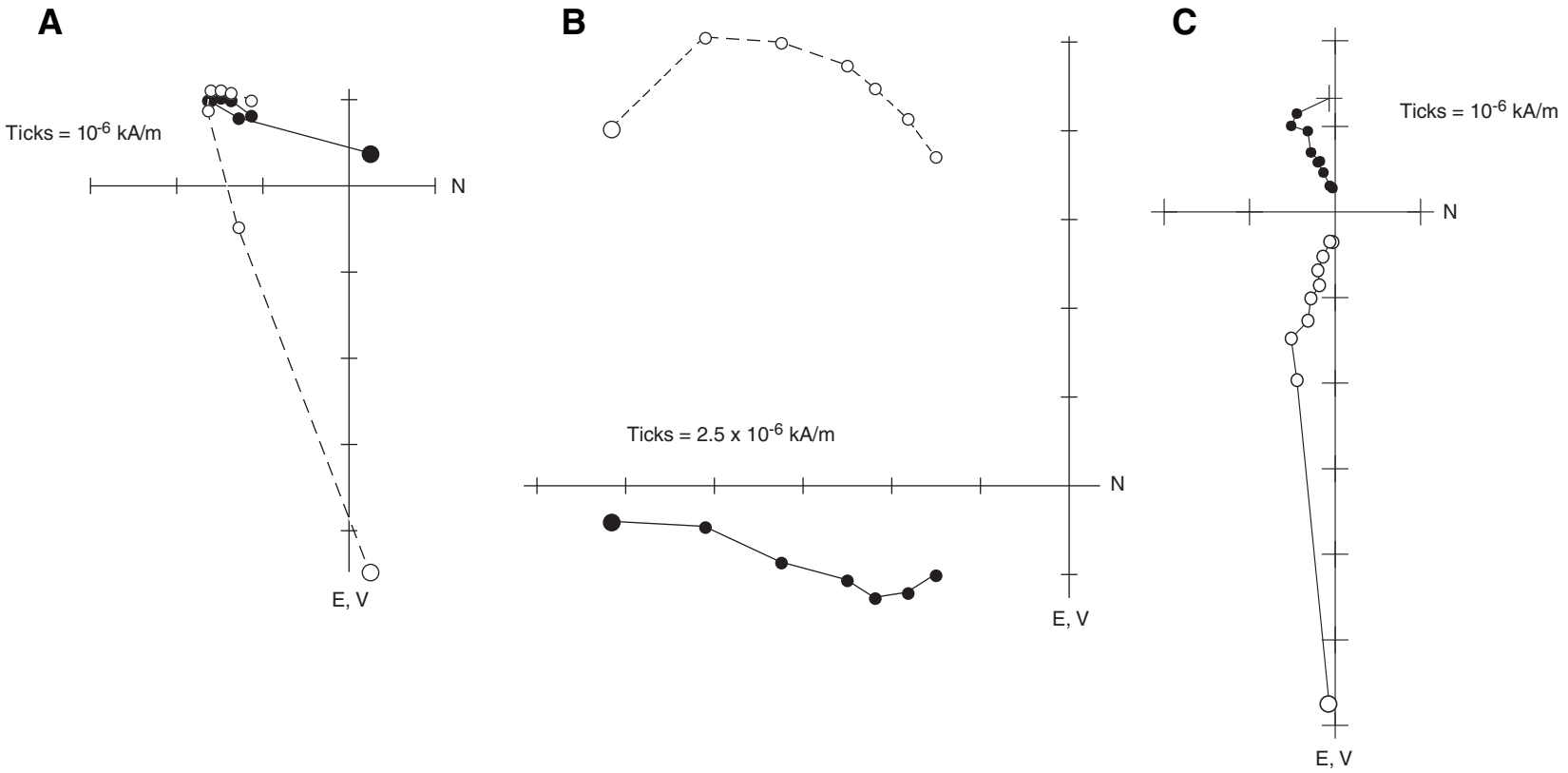

Figure F17. Remanence inclination after 30 mT AF demagnetization in the interval between 0 and 203 m core depth below seafloor (CSF), Hole C0002D.

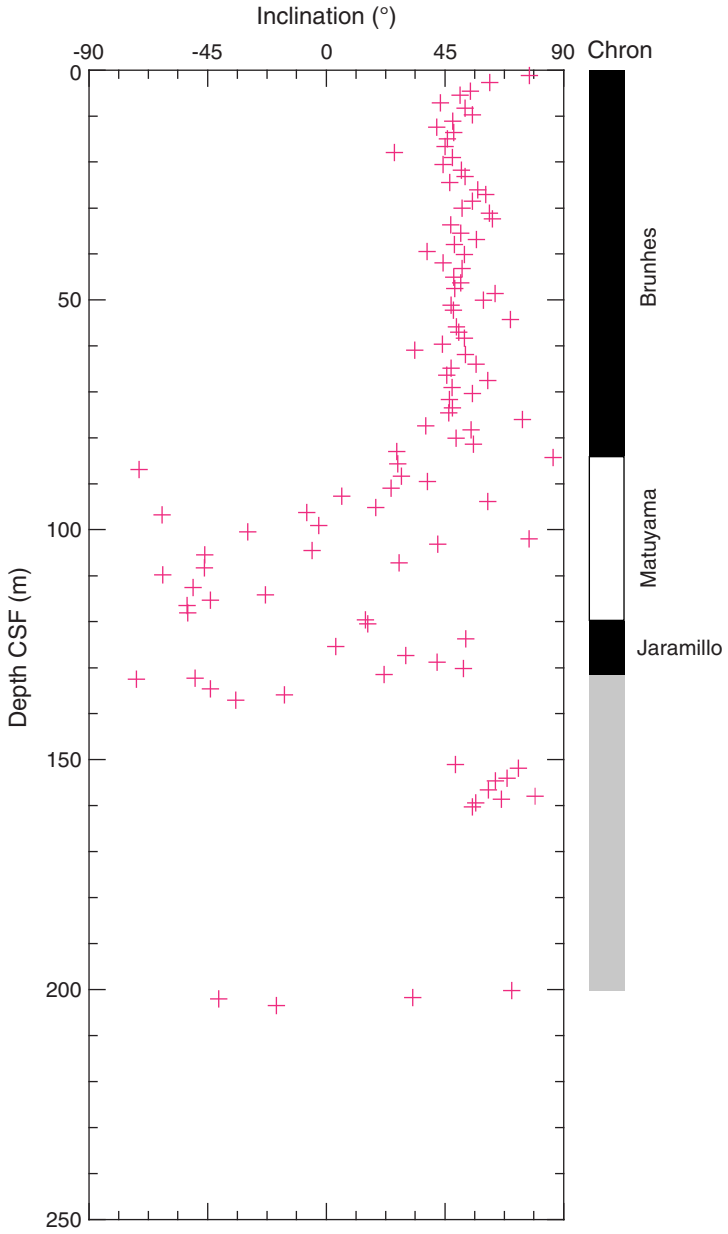

Figure F18. ChRM inclination after 30 mT AF demagnetization, 460–1060 m core depth below seafloor (CSF) (Hole C0001B). Note interval between 460 and 620 m CSF was not interpreted because of anomalous concentrated direction of declination. Black = normal polarity, white = reversed polarity, gray = unknown.

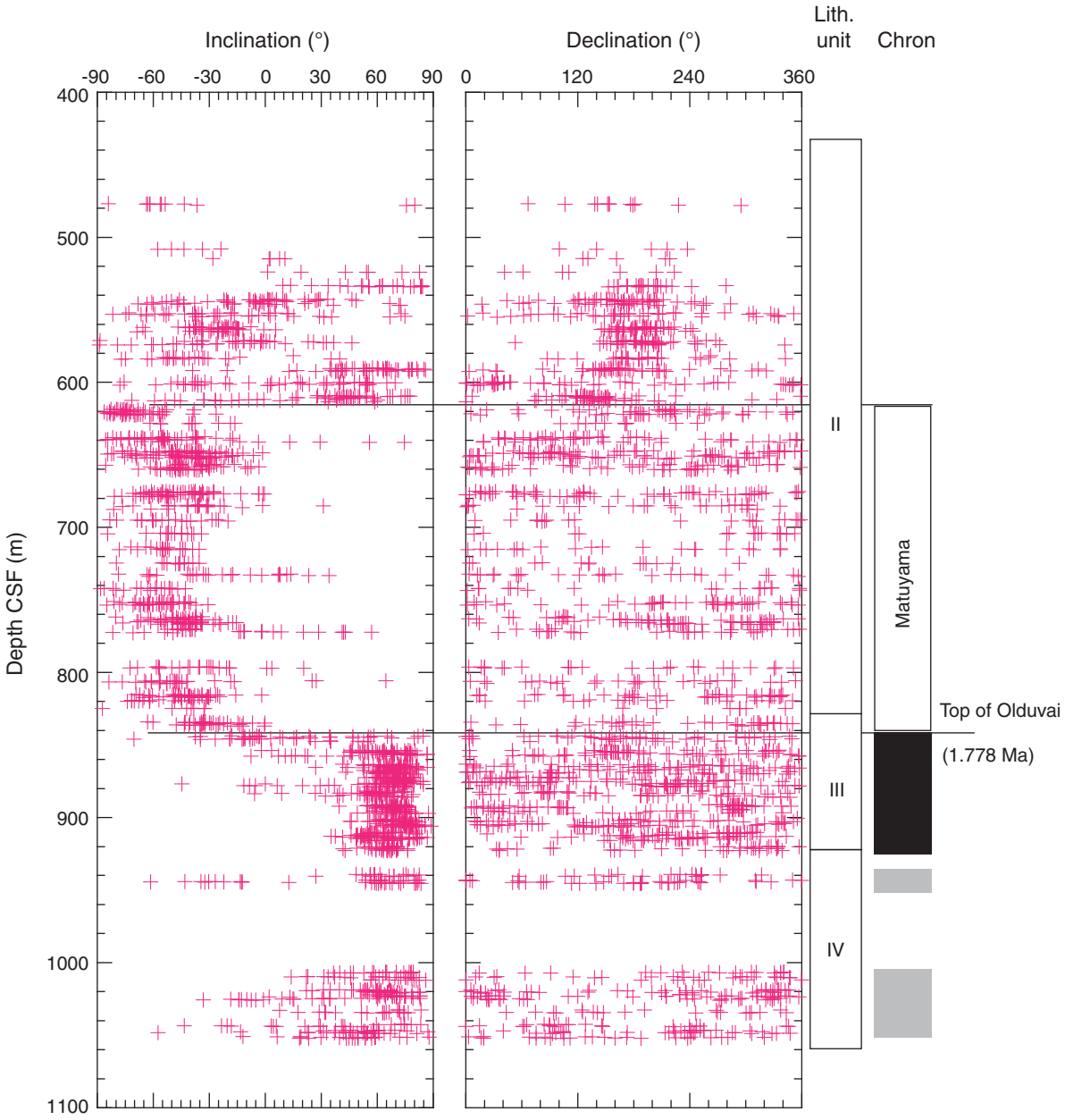

Figure F19. Inclination and bedding dip variation, Hole C0002B. Dashed lines = expected inclination, which can be calculated from the latitude of location. CSF = core depth below seafloor.

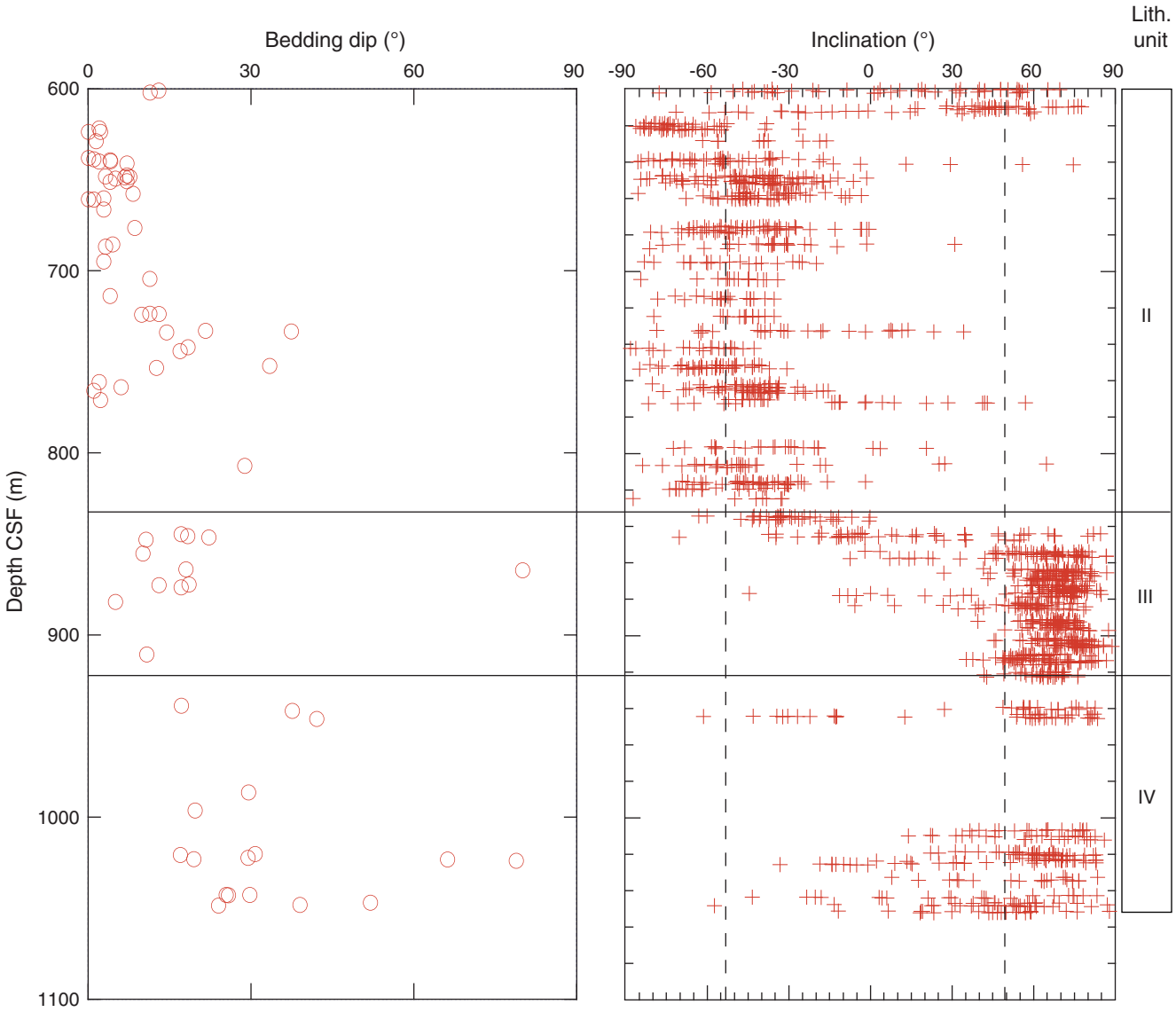

Figure F20. Concentrations of sulfate, phosphate and ammonium, major halogens (Cl and Br), and pH, alkalinity, and salinity in interstitial waters, Site C0002. Salinity is calculated as total dissolved solutes. Star = seawater value. CSF = core depth below seafloor.

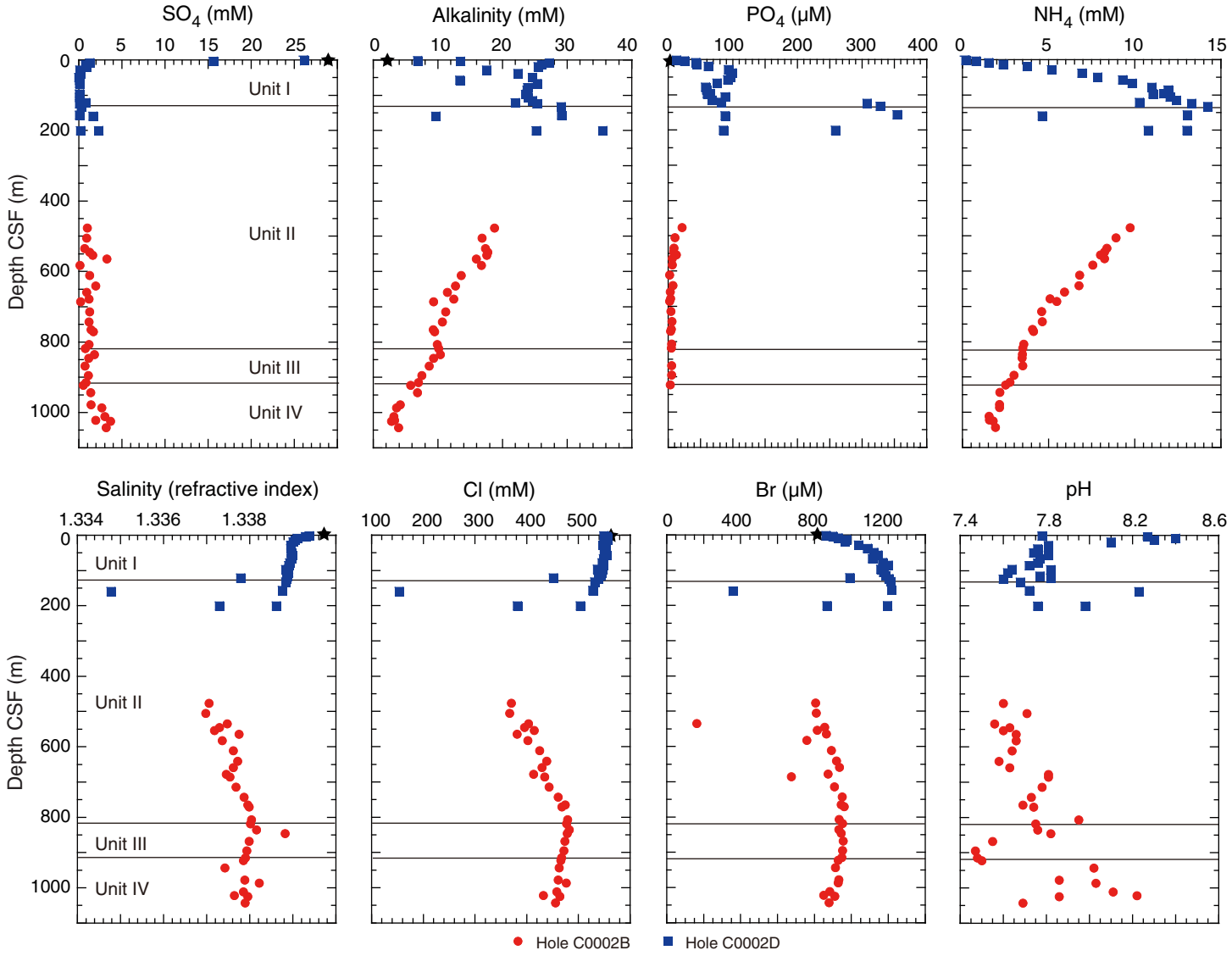

Figure F21. Concentrations of major (Na, K, Ca, and Mg) and minor (Si, B, Li, Mn, and Fe) cations in interstitial waters, Site C0002. Star = seawater value. CSF = core depth below seafloor.

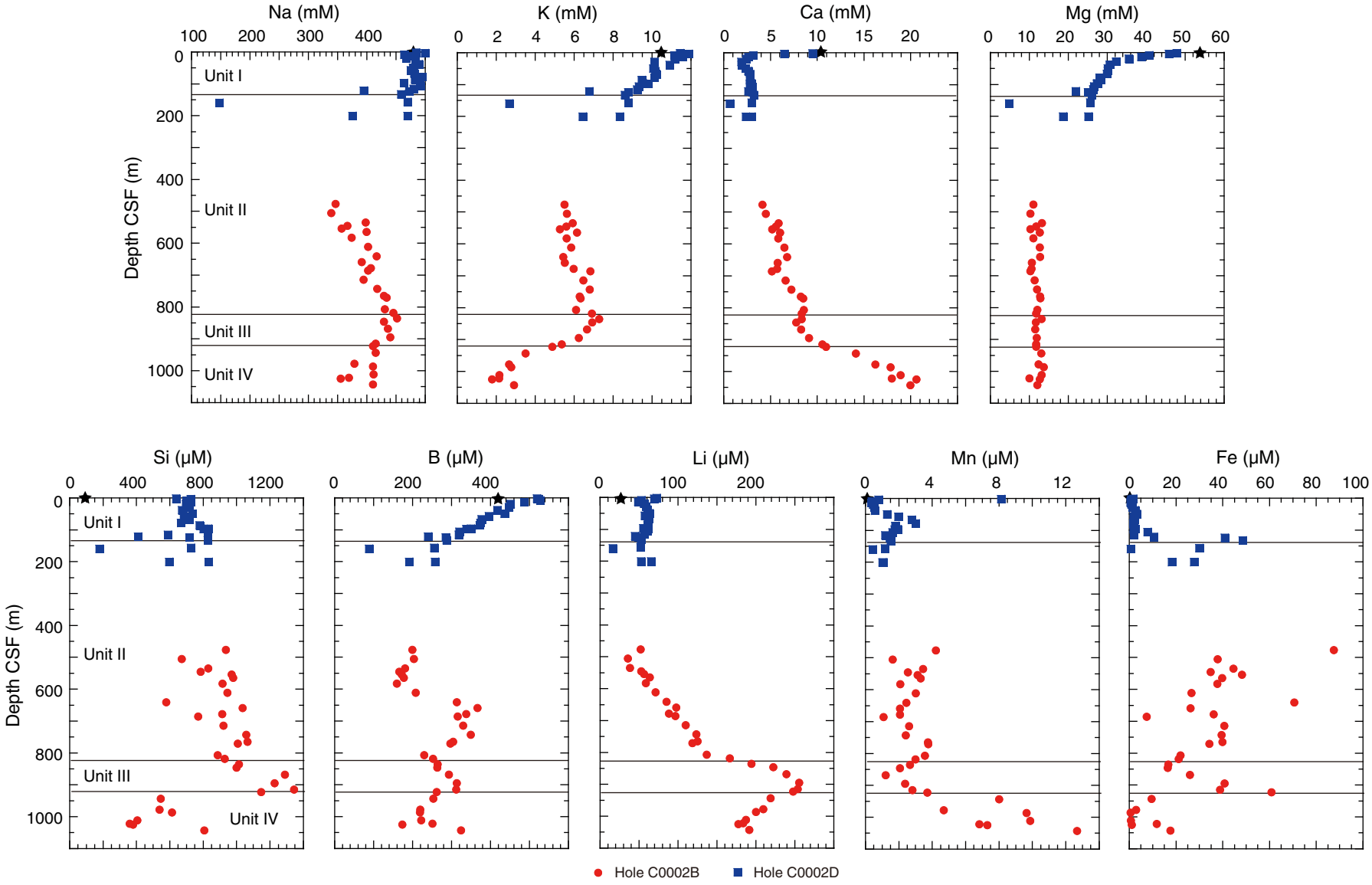

Figure F22. Concentrations of minor cations (Sr and Ba) and trace elements (Mo, V, Zn, Cu, Rb, Cs, Pb, and U) in interstitial waters, Site C0002. Star = seawater value. VSMOW = Vienna standard mean ocean water. CSF = core depth below seafloor.

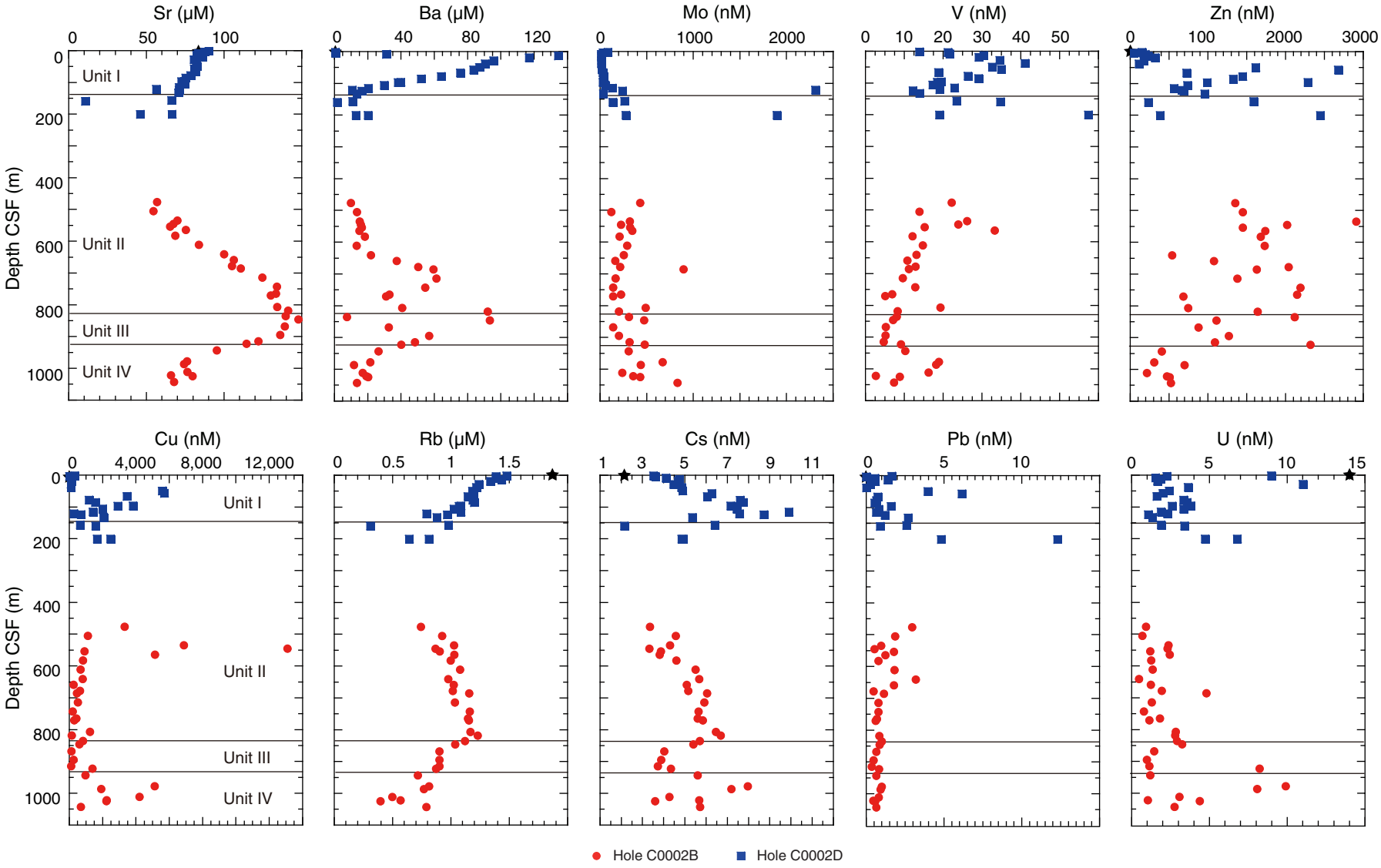

Figure F23. Concentration of Y and oxygen and hydrogen isotopic composition of interstitial water, Site C0002. Star = standard seawater value. CSF = core depth below seafloor.

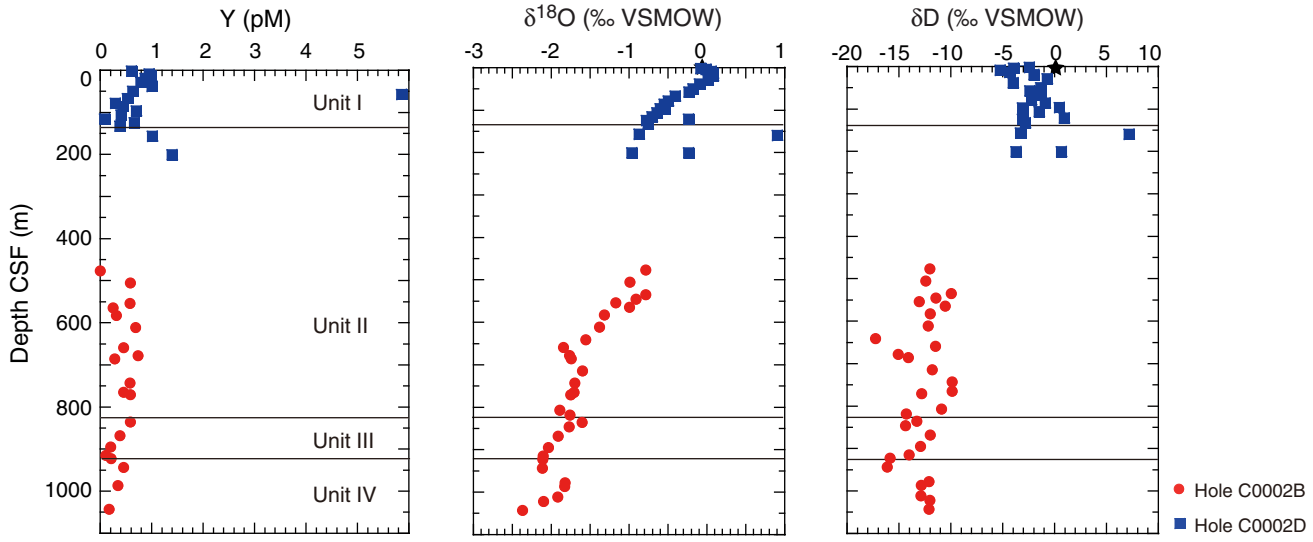

Figure F24. Methane, ethane, and propane concentrations in headspace samples, Site C0002. CSF = core depth below seafloor.

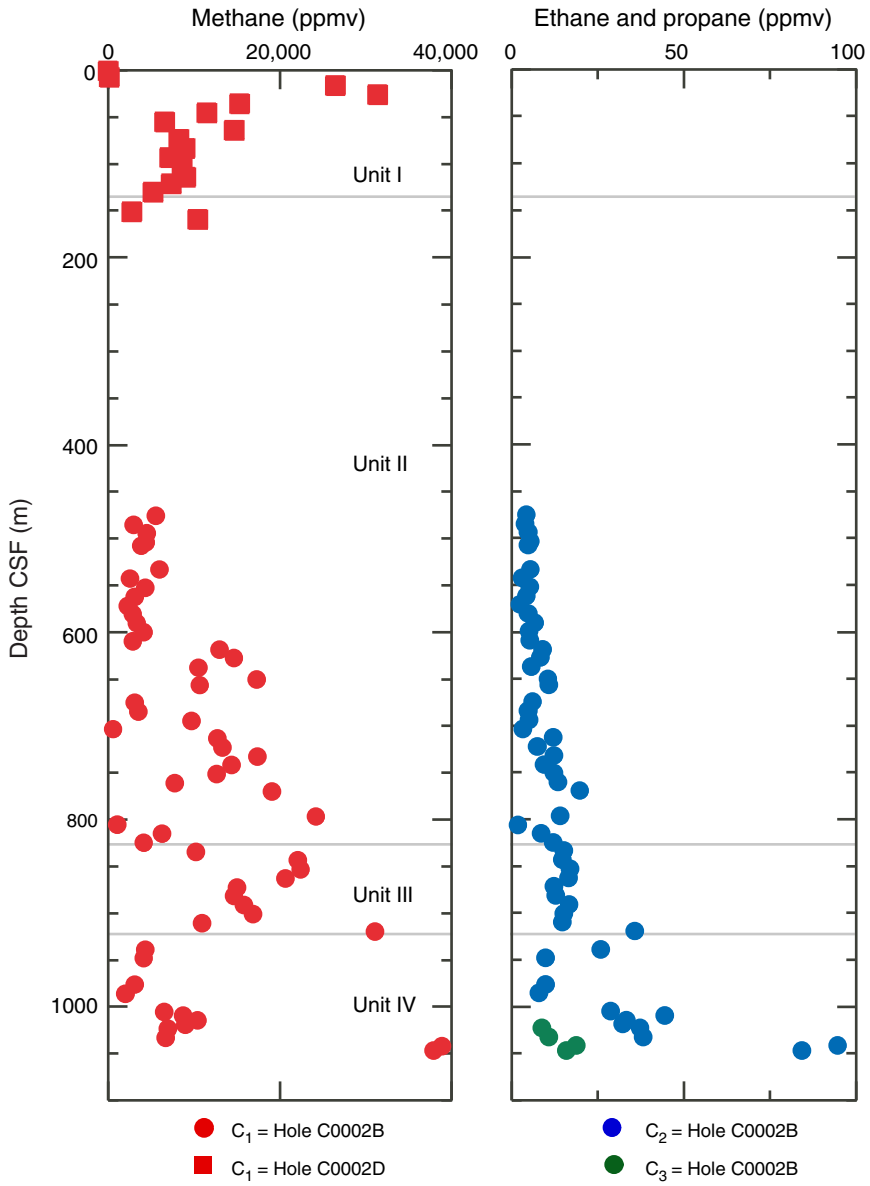

Figure F25. Methane to ethane ratio, Site C0002. CSF = core depth below seafloor.

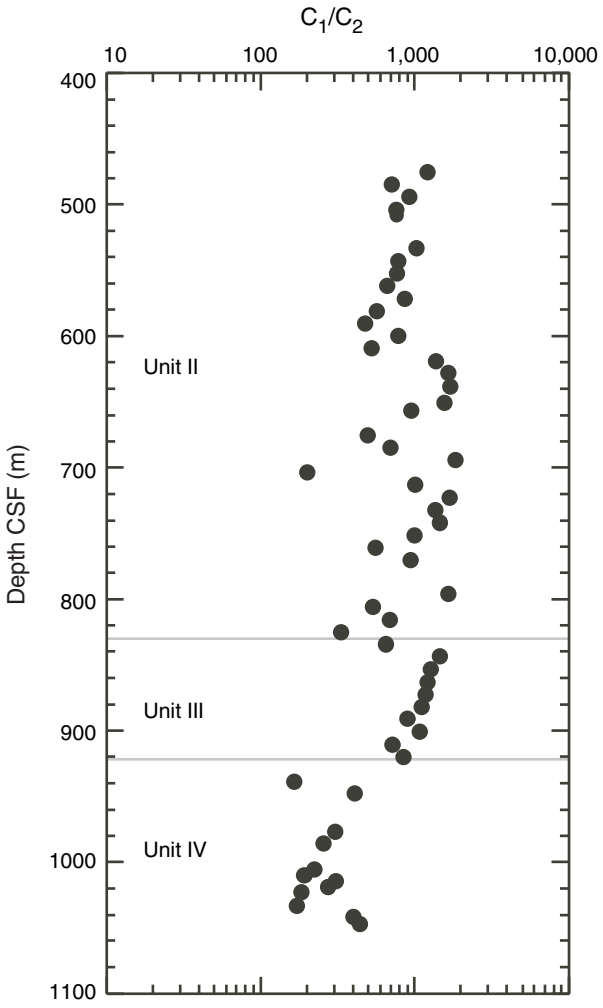

Figure F26. Inorganic carbon (IC), calcium carbonate ($CaCO_3$), total organic carbon (TOC), total nitrogen (TN), carbon to nitrogen (C/N) ratio, and total sulfur in sediments from Site C0002. CSF = core depth below seafloor.

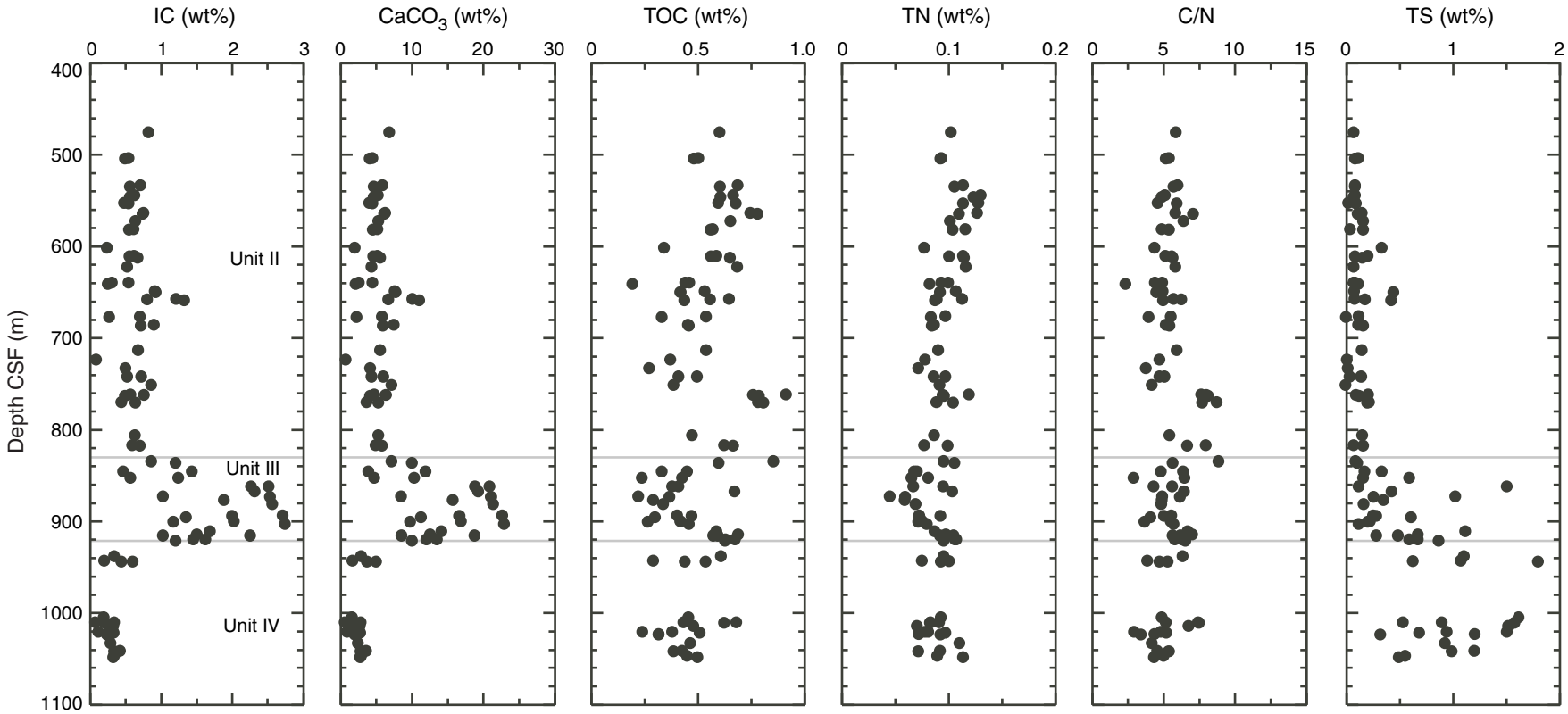

Figure F27. Epifluorescence image of SYBR Green I–stained sample of fixed cells (Section 315-C0002B-61R-1) (1020 m core depth below seafloor).

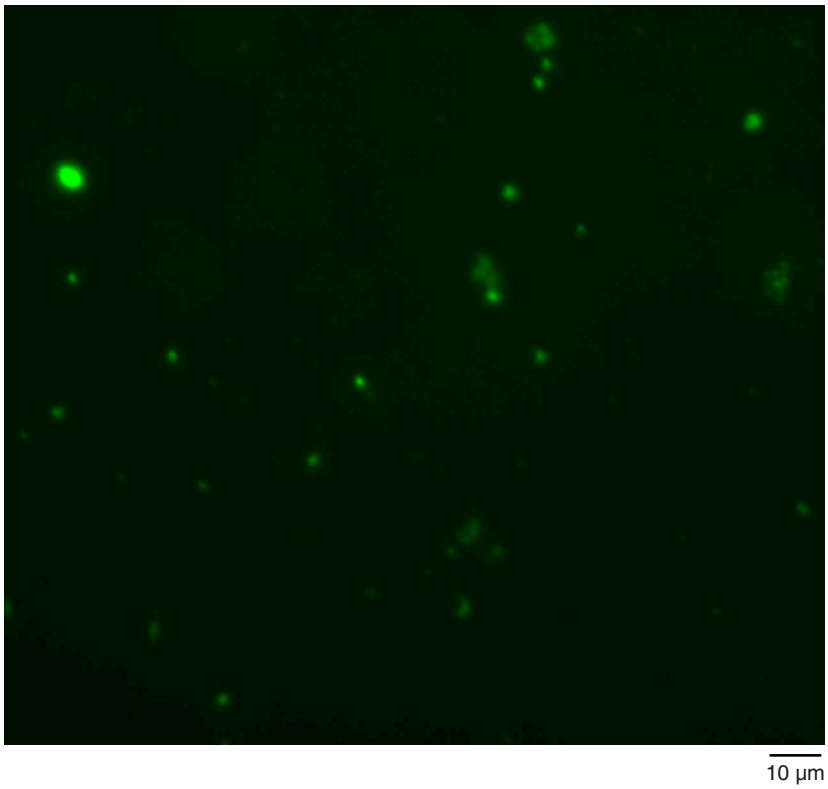

Figure F28. Moisture and density measurements, Site C0002. **A.** MAD porosity. **B.** MAD and multisensor core logger (MSCL) whole-round core (MSCL-W) bulk density. **C.** MAD grain density. CSF = core depth below seafloor.

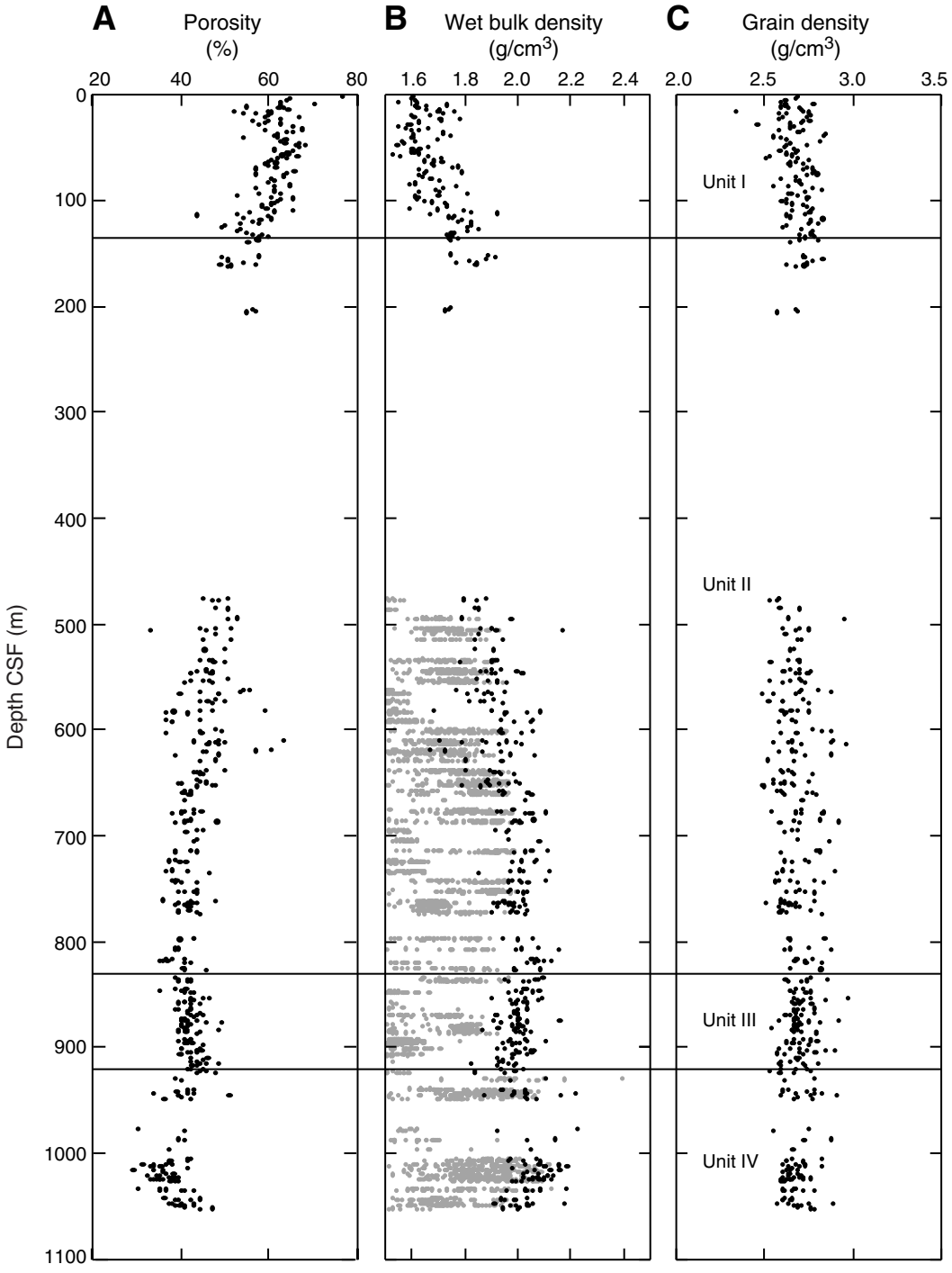

Figure F29. Physical property measurements, Site C0002. **A.** Undrained shear strength measured using a pocket penetrometer. **B.** Porosity profile. **C.** Thermal conductivity. CSF = core depth below seafloor.

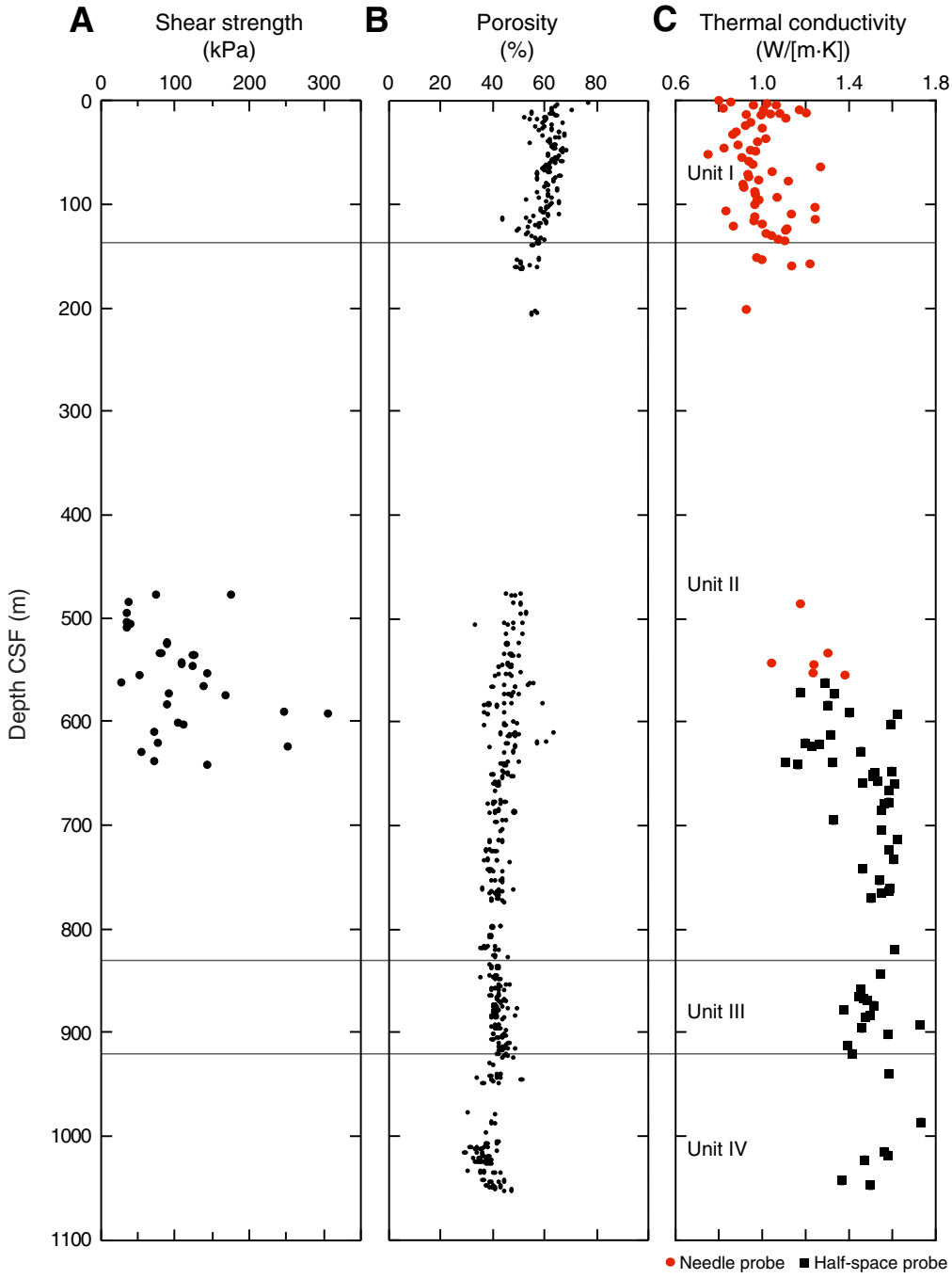

Figure F30. Values of L*, a*, and b*, Site C0002. CSF = core depth below seafloor.

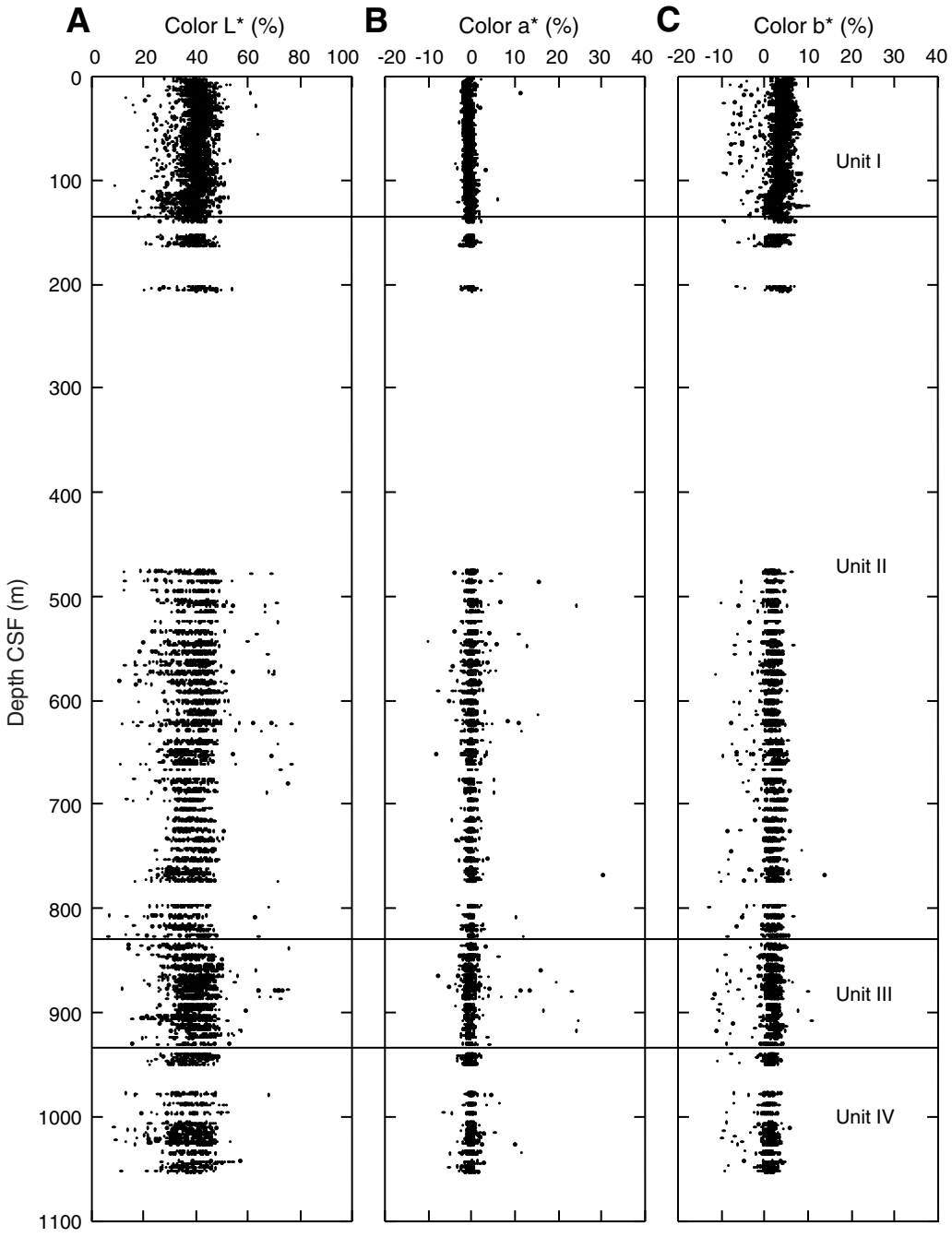

Figure F31. Downhole temperature, Site C0002. Gradient fit of measurements = 43°C/km. Heat flow determination and temperature extrapolation based on downhole temperature measurements. CSF = core depth below seafloor.

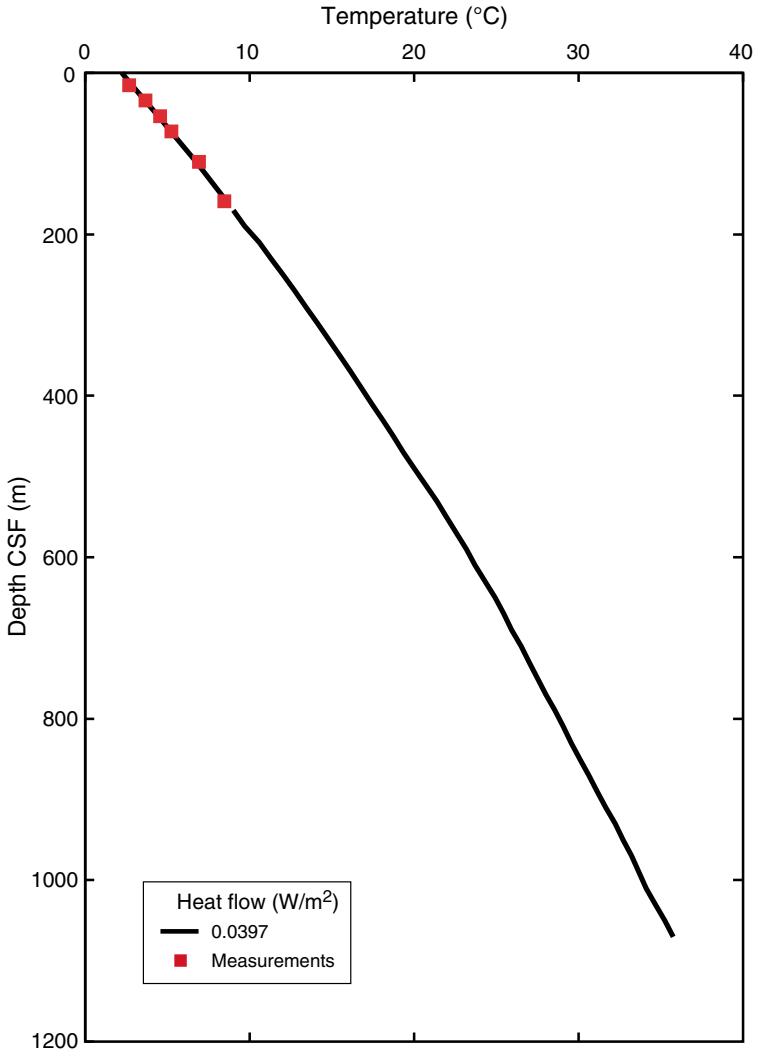

Figure F32. Electrical conductivity and *P*-wave velocity measurements on discrete samples in orthogonal directions (*x*, *y*, and *z*). CSF = core depth below seafloor.

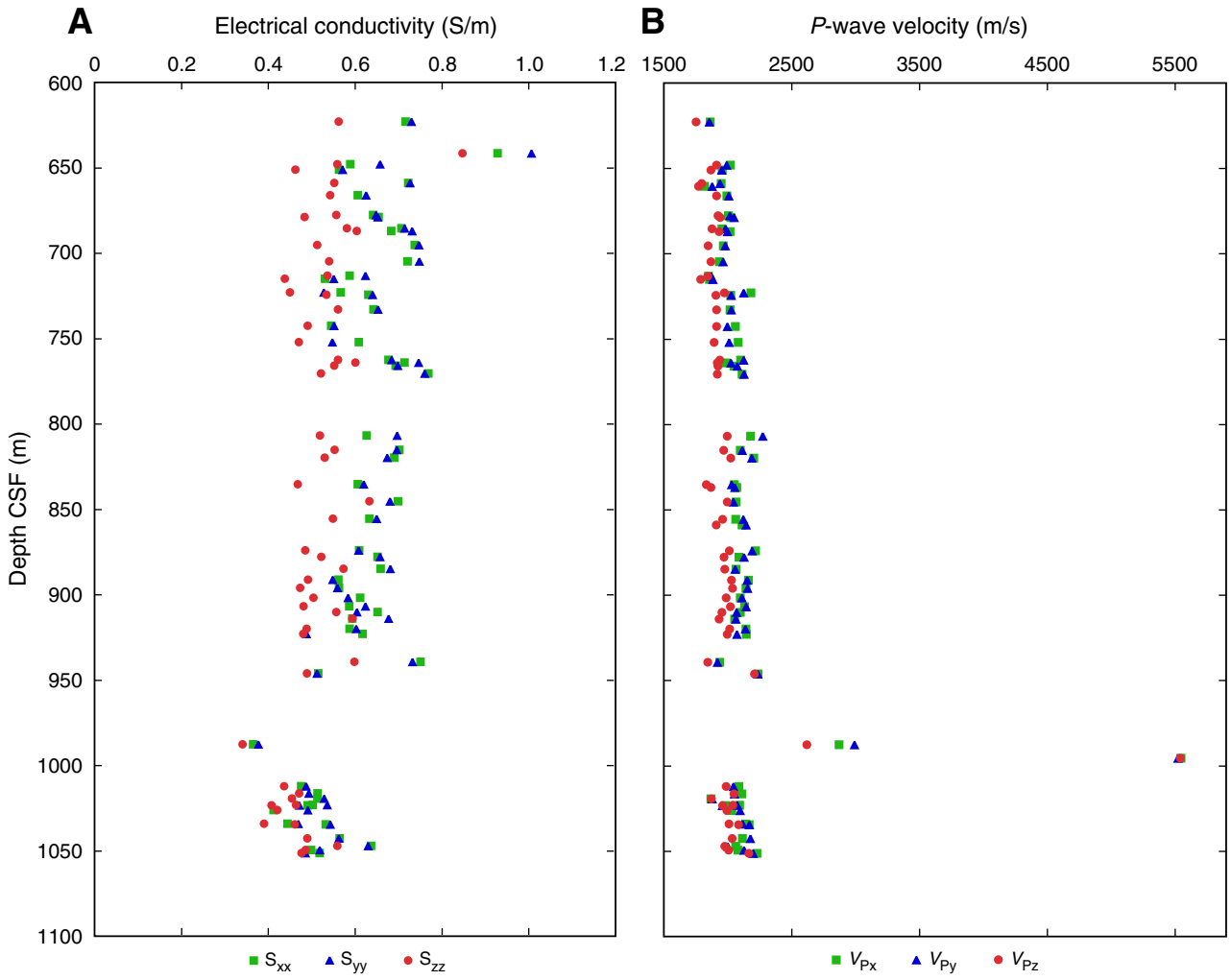

Figure F33. Location of drill holes on depth-corrected seismic profile (Inline 2529). CDP = common depth point.

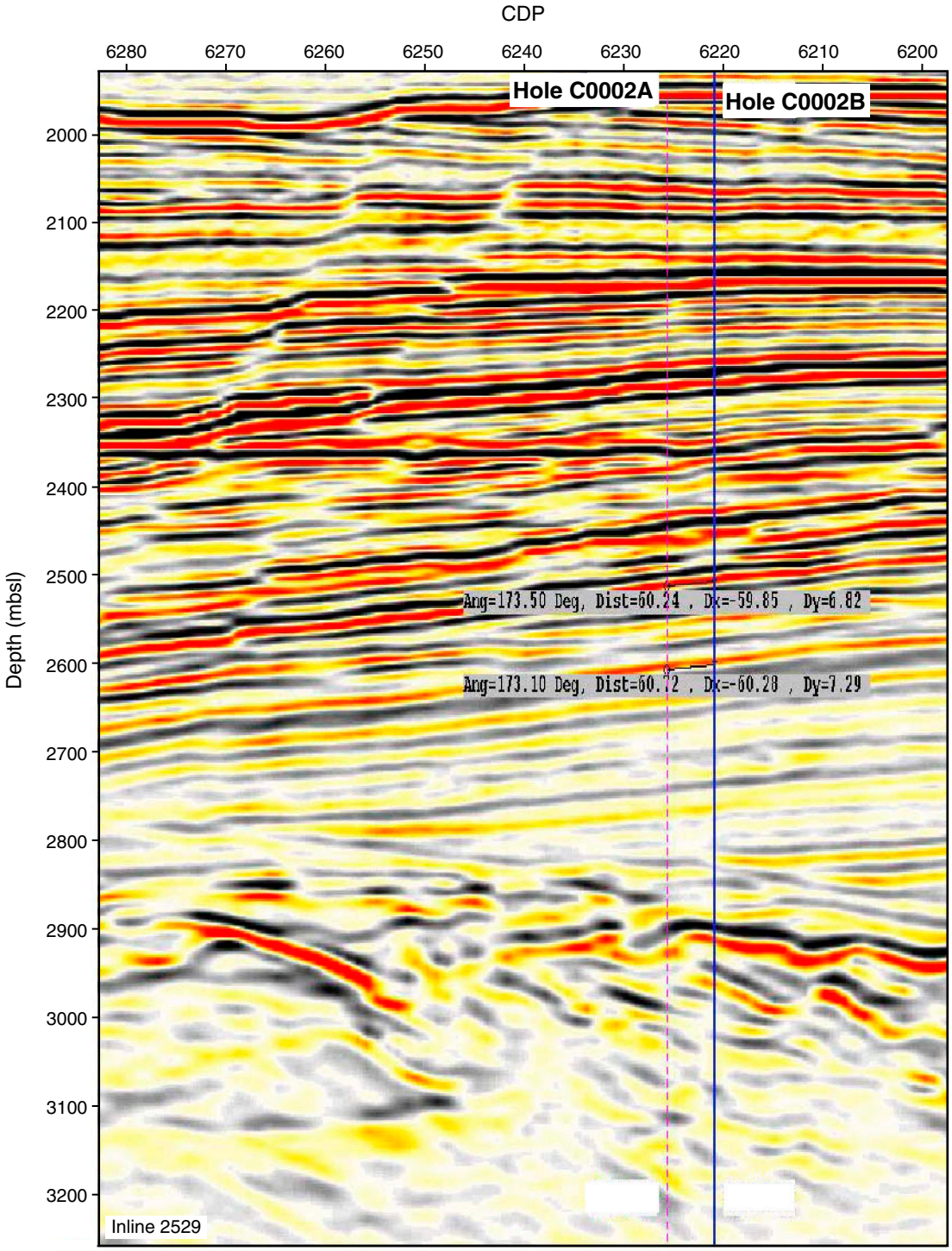

Figure F34. Natural gamma ray (NGR) data from logging-while-drilling (LWD) and cores. **A.** Logs as a function of depth. **B.** Core log fit to LWD, Hole C0001A. **C.** Zoom on fit proposed for the lower part of Hole C0001A. CSF = core depth below seafloor, LSF = LWD depth below seafloor. MSCL-W = multisensor core logger measurements on whole-round cores.

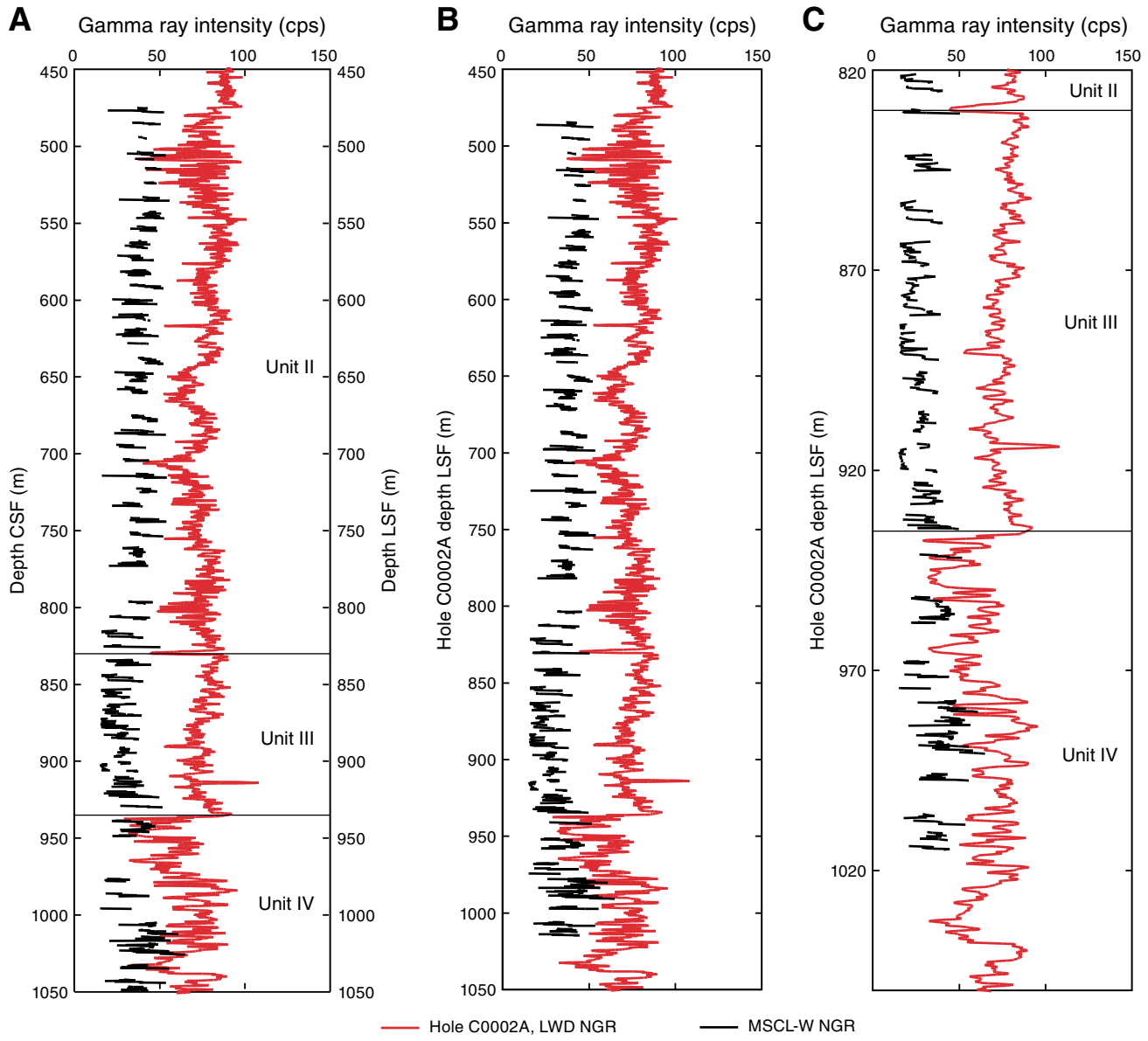

Figure F35. Density and resistivity obtained on discrete samples and from logging-while-drilling (LWD) in the lower part of Holes C0002A and C0002B. Density from gamma ray backscattering is represented only in intervals with a borehole average diameter of <9.5 inches. For comparison with LWD bit resistivity, which explores a volume around the drill bit, sample resistivity represented is the geometric mean of the horizontal and vertical resistivity measured on the samples. The resistivity of the samples is corrected for in situ temperature assuming a gradient of 35°C/km. CSF = core depth below seafloor.

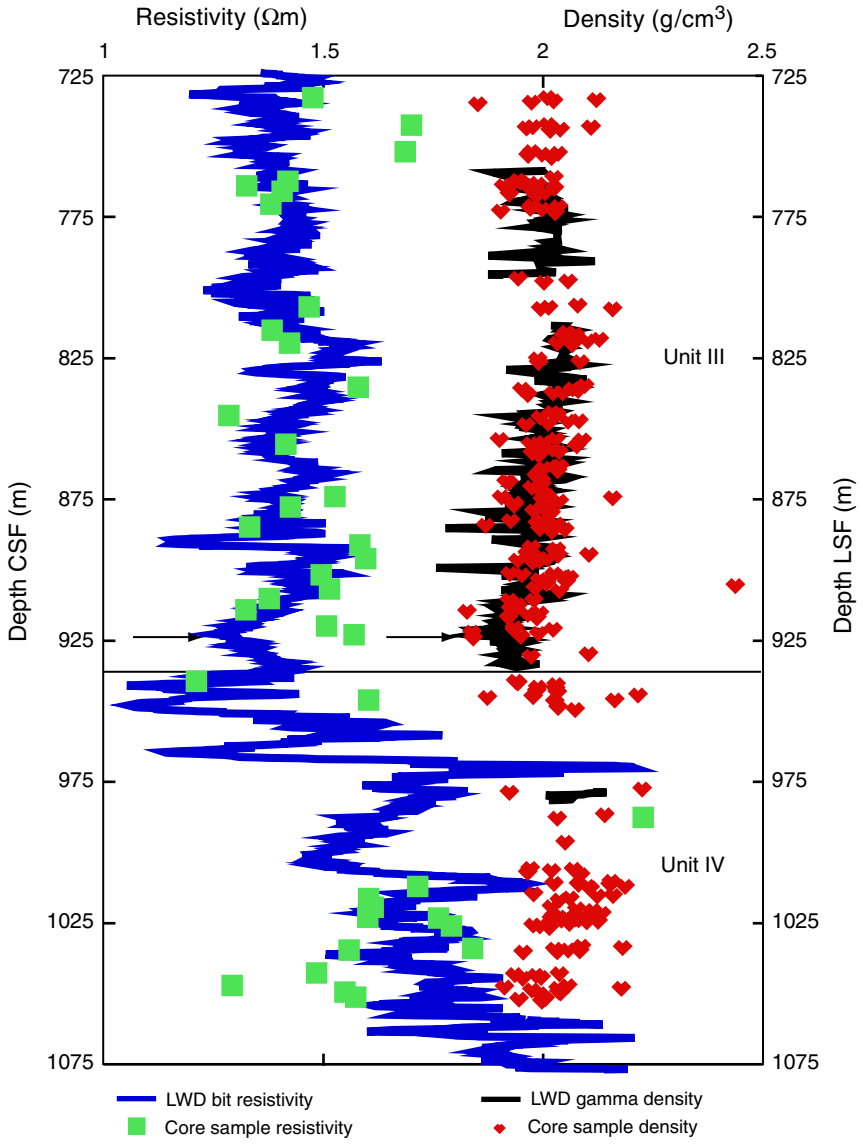

Figure F36. *P*-wave velocity in vertical direction (V_{Pz}) from logging while drilling (LWD) in Hole C0002A and from discrete samples from Hole C0002B. Values in blue were measured in the laboratory. CSF = core depth below seafloor.

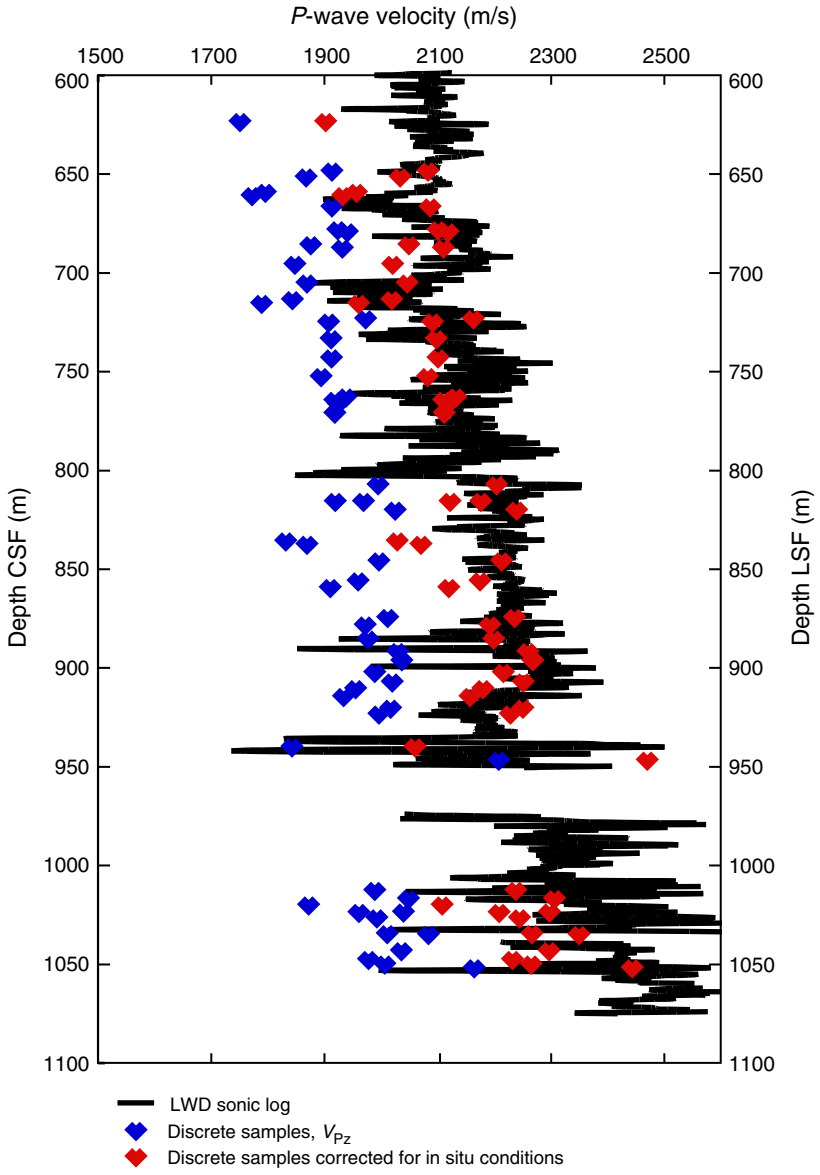

Figure F37. Core recovery around the main unconformity, Hole C0002B. Red line = Hole C0001A. Blue = LWD ring resistivity, black and white column = recovery. CSF = core depth below seafloor.

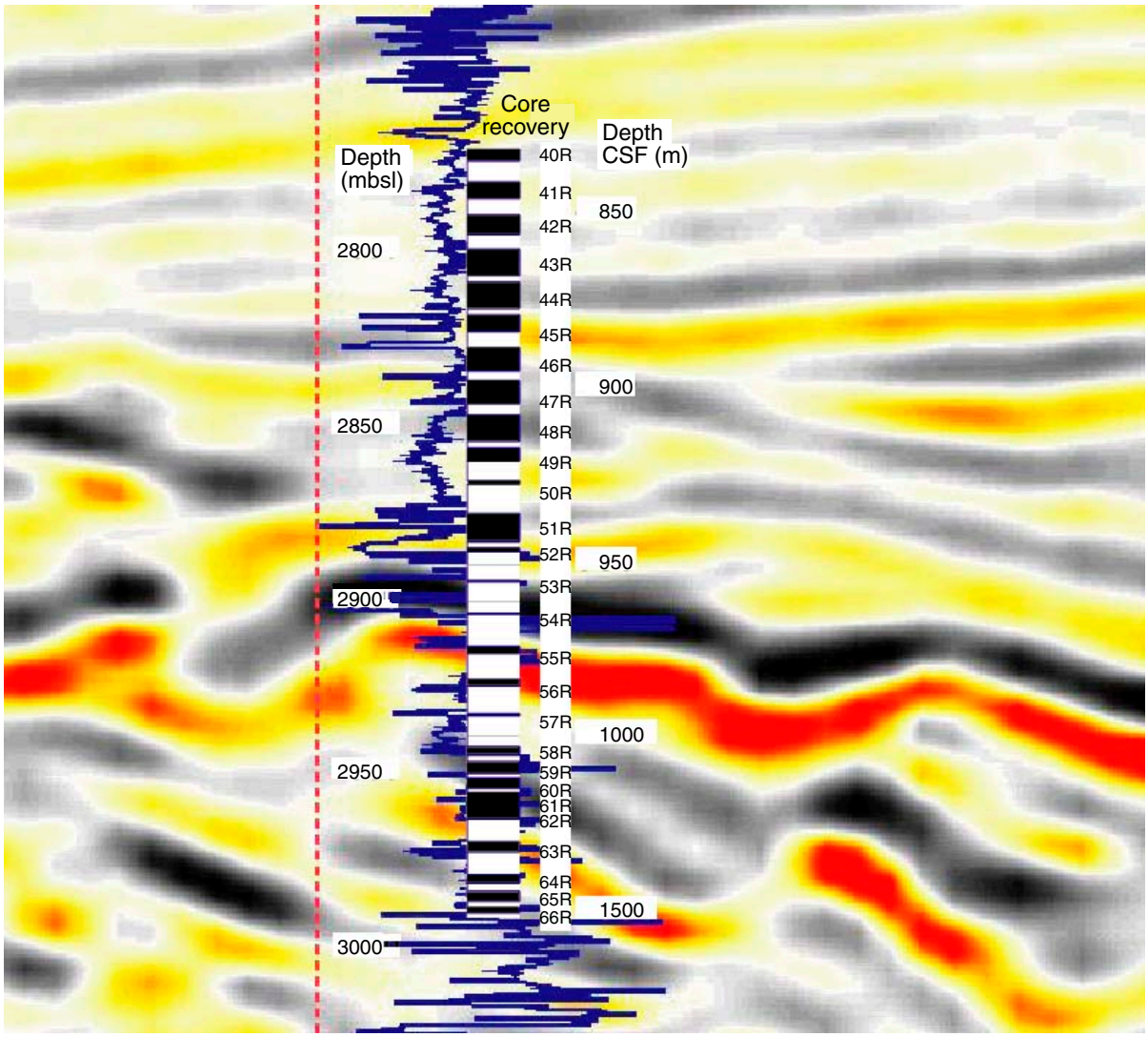

Table T1. Coring summary, Hole C0002B. (See table notes.) (Continued on next page.)

Hole C0002B
Latitude: 33°17.9928′N
Longitude: 136°38.2029′E
Time on hole (h): 183.5 (0530 h, 8 Dec 2007–2100 h, 15 Dec 2007)
Seafloor (drillers measurement from rig floor, m): 1966.0
Distance between rig floor and sea level (m): 28.5
Water depth (drillers measurement from sea level, m): 1937.5
Total depth (drillers depth below rig floor, m): 3023
Total penetration (core depth below seafloor, m): 1057
Total length of cored section (m): 582.0
Total core recovered (m): 208.3
Core recovery (%): 35.8
Total number of cores: 66

Core	Date (Dec 2007)	Local time (h)	Depth CSF (m) Top	Depth CSF (m) Bottom	Length (m) Cored	Length (m) Recovered	Recovery (%)	Comments
315-C0002B-								
1R	10	0616	475.0	484.5	9.5	3.1	32.9	
2R	10	0728	484.5	494.0	9.5	1.4	14.9	
3R	10	0834	494.0	503.5	9.5	1.2	12.7	
4R	10	0927	503.5	508.0	4.5	2.7	60.7	Change to advance-by-recovery to improve recovery
5R	10	1018	508.0	514.0	6.0	0.8	13.0	
6R	10	1112	514.0	523.5	9.5	1.0	10.6	
7R	10	1322	523.5	533.0	9.5	1.0	10.0	Increased bit rotation from 40 to 60 rpm
8R	10	1540	533.0	542.5	9.5	2.7	28.2	
9R	10	1614	542.5	552.0	9.5	4.2	44.6	
10R	10	1712	552.0	561.5	9.5	3.3	35.1	
11R	10	1801	561.5	571.0	9.5	4.9	51.8	Increased bit rotation from 60 to 80 rpm
12R	10	1857	571.0	580.5	9.5	3.5	36.3	
13R	10	1947	580.5	590.0	9.5	3.8	39.9	
14R	10	2029	590.0	599.5	9.5	2.8	29.8	
15R	10	2125	599.5	609.0	9.5	3.3	34.4	
16R	10	2215	609.0	618.5	9.5	4.6	48.0	
17R	11	0014	618.5	628.0	9.5	5.3	56.0	
18R	11	0100	628.0	637.5	9.5	0.8	8.1	
19R	11	0426	637.5	647.0	9.5	4.2	44.4	
20R	11	0520	647.0	656.5	9.5	5.9	62.3	
21R	11	0626	656.5	666.0	9.5	4.5	46.9	
22R	11	0730	666.0	675.0	9.0	0.2	2.3	
23R	11	1808	675.0	684.5	9.5	4.1	43.2	
24R	11	1904	684.5	694.0	9.5	3.3	34.6	
25R	11	1948	694.0	703.5	9.5	2.2	22.6	
26R	11	2232	703.5	713.0	9.5	1.3	13.6	
27R	12	0005	713.0	722.5	9.5	2.7	28.7	
28R	12	0111	722.5	732.0	9.5	3.0	31.7	
29R	12	0220	732.0	741.5	9.5	2.5	26.6	
30R	12	0355	741.5	751.0	9.5	2.9	30.3	
31R	12	0502	751.0	760.5	9.5	2.8	29.6	Decreased bit rotation from 90 to 60 rpm
32R	12	0604	760.5	770.0	9.5	6.6	69.9	
33R	12	1035	770.0	779.5	9.5	3.2	33.3	
34R	12	1157	779.5	789.0	9.5	0.0	0.0	
35R	12	1353	789.0	796.0	7.0	0.0	0.0	
36R	12	1558	796.0	805.5	9.5	1.7	17.8	
37R	12	1712	805.5	815.0	9.5	2.3	24.2	Radius of core decreased by washout at top portion of core (~2 m)
38R	12	1848	815.0	824.5	9.5	5.0	52.4	
39R	12	2016	824.5	834.0	9.5	1.5	15.9	
40R	12	2153	834.0	843.5	9.5	3.5	36.8	
41R	12	2316	843.5	853.0	9.5	4.8	50.7	
42R	13	0032	853.0	862.5	9.5	5.7	59.5	Changed pump rate from 60 to 50 gpm
43R	13	0141	862.5	872.0	9.5	7.9	83.4	Changed pump rate from 50 to 45 gpm
44R	13	0246	872.0	881.5	9.5	7.4	77.9	Changed pump rate from 45 to 40 gpm
45R	13	0446	881.5	891.0	9.5	4.6	48.8	Pump rate between 35 and 60 gpm
46R	13	0622	891.0	900.5	9.5	6.3	66.2	
47R	13	0806	900.5	910.0	9.5	6.3	66.6	
48R	13	0954	910.0	919.5	9.5	7.5	78.7	
49R	13	1142	919.5	929.0	9.5	4.0	42.2	
50R	13	1353	929.0	938.5	9.5	1.0	10.5	
51R	13	1719	938.5	948.0	9.5	7.6	80.4	
52R	13	2002	948.0	957.5	9.5	1.0	10.7	
53R	13	2105	957.5	967.0	9.5	0.0	0.0	

Table T1 (continued).

Core	Date (Dec 2007)	Local time (h)	Depth CSF (m) Top	Depth CSF (m) Bottom	Length (m) Cored	Length (m) Recovered	Recovery (%)	Comments
54R	13	2215	967.0	976.5	9.5	0.0	0.0	Deployed center bit after this core
55R	14	0332	976.5	986.0	9.5	1.8	19.4	Changed core catcher
56R	14	0556	986.0	995.5	9.5	1.9	20.3	
57R	14	0838	995.5	1005.0	9.5	0.8	8.6	
58R	14	0951	1005.0	1009.5	4.5	2.5	54.7	Changed to advance-by-recovery to improve recovery
59R	14	1117	1009.5	1014.0	4.5	3.2	70.6	
60R	14	1247	1014.0	1018.5	4.5	2.9	63.3	
61R	14	1428	1018.5	1023.0	4.5	5.3	117.1	
62R	14	1627	1023.0	1032.5	9.5	3.0	31.1	
63R	14	1847	1032.5	1042.0	9.5	2.5	26.1	
64R	14	2005	1042.0	1046.5	4.5	2.4	52.4	
65R	14	2111	1046.5	1051.0	4.5	2.8	62.7	
66R	14	2248	1051.0	1057.0	6.0	1.4	23.2	
			Cored totals:		582.0	208.3	35.8	

Notes: CSF = core depth below seafloor. rpm = revolutions per minute, gpm = gallons per minute.

Table T2. Coring summary, Hole C0002C. (**See table note.**)

Hole C0002C
Latitude: 33°18.0026′N
Longitude: 136°38.1869′E
Time on hole (h): 16.75 (0130 h, 16 Dec 2007–1815 h, 16 Dec 2007)
Seafloor (drillers measurement from rig floor, m): 1965.1
Distance between rig floor and sea level (m): 28.5
Water depth (drillers measurement from sea level, m): 1936.6
Total depth (drillers depth below rig floor, m): 1978.9
Total penetration (core depth below seafloor, m): 13.77
Total length of cored section (m): 13.80
Total core recovered (m): 13.77
Core recovery (%): 99.8
Total number of cores: 2

Core	Date (Dec 2007)	Local time (h)	Depth CSF (m) Top	Depth CSF (m) Bottom	Length (m) Cored	Length (m) Recovered	Recovery (%)
315-C0002C-							
1H	16	1723	0.0	6.90	6.90	6.90	100.0
2H	16	1839	6.9	13.77	6.87	6.87	100.0
				Cored totals:	13.77	13.77	100.0

Note: CSF = core depth below seafloor.

Table T3. Coring summary, Hole C0002D. (See table notes.)

Hole C0002D
Latitude: 33°18.0075′N
Longitude: 136°38.1910′E
Time on hole (h): 42.75 (1830 h, 16 Dec 2007–1345 h, 18 Dec 2007)
Seafloor (drillers measurement from rig floor, m): 1965.62
Distance between rig floor and sea level (m): 28.5
Water depth (drillers measurement from sea level, m): 1937.12
Total depth (drillers depth below rig floor, m): 2169.62
Total penetration (core depth below seafloor, m): 204
Total length of cored section (m): 204.0
Total core recovered (m): 161.9
Core recovery (%): 79.4
Total number of cores: 18

Core	Date (Dec 2007)	Local time (h)	Depth CSF (m) Top	Depth CSF (m) Bottom	Length (m) Cored	Length (m) Recovered	Recovery (%)	Comments
315-C0002D-								
1H	16	1952	0.0	5.9	5.9	5.9	100.0	
2H	16	2132	5.9	15.4	9.5	10.1	105.8	With APCT3
3H	16	2246	15.4	24.9	9.5	10.0	105.4	
4H	16	2359	24.9	34.4	9.5	10.6	111.8	With APCT3
5H	17	0044	34.4	43.9	9.5	10.4	109.2	
6H	17	0145	43.9	53.4	9.5	10.6	111.4	With APCT3
7H	17	0233	53.4	62.9	9.5	10.5	110.3	
8H	17	0339	62.9	72.4	9.5	10.5	110.2	With APCT3
9H	17	0425	72.4	81.9	9.5	10.2	107.2	
10H	17	0525	81.9	91.4	9.5	10.2	107.8	With APCT3
11H	17	0633	91.4	100.9	9.5	9.8	103.1	
12H	17	0750	100.9	110.4	9.5	10.3	108.6	With APCT3
13H	17	1046	110.4	119.9	9.5	10.1	105.9	
14H	17	1527	119.9	129.2	9.3	9.3	100.0	With APCT3
15X	17	1718	129.2	150.0	20.9	8.4	40.4	Wash core
16H	17	1901	150.0	159.0	9.0	9.0	100.0	With APCT3
17X	17	2339	159.0	200.0	41.0	2.2	5.3	Wash core
18H	18	0134	200.0	204.0	4.0	4.0	100.0	With APCT3
				Cored totals:	204.0	161.9	79.4	

Notes: CSF = core depth below seafloor. APCT3 = advanced piston corer temperature tool.

Table T4. Summary of lithologic units, Site C0002. (See table note.)

Depth CSF (m)	Unit	Lithology	Environmental interpretation
0.0–135.8	I	Clayey silt, sand and silt, volcanic ash	Distal basin plain (upper Kumano basin)
135.8–830.4	II	Clayey silt, abundant silt, and sand beds	Hemipelagic settling and frequent turbidites in distal basin plain
830.4–921.7	III	Silty clay, rare volcanic ash	Hemipelagic settling in starved basin
921.7–1052.5	IV	Clayey siltstone, sandstone, siltstone	Hemipelagic settling and turbidites in outer margin of trench wedge

Note: CSF = core depth below seafloor.

Table T5. Intervals of interest, Hole C0002B. (**Continued on next page.**)

Interval of interest	Core, section, interval (cm)	Comment
	315-C0002B-	
Unusual black and white fossils	51R-1, 10	
	51R-2, 74–80	
	51R-3, 119	Best in sample half
	65R-1, 60	Possible agglutinated worm tube
Unusual grains	31R-2, 82–88	Possible breccia?
	41R-1, 20	Possible synsedimentary clast
	41R-1, 52	Possible synsedimentary clast
	41R-2, 96	Possible synsedimentary clast
	42R-2, 75–77	Rounded clasts
	42R-3, 0–13	Black sand-sized particles
	42R-3, 40–85	Black sand-sized particles
	43R-1, 59–14	Possible synsedimentary clast
	44R-2, 82	
	44R-5, 113	
	45R-2, 86	
	45R-3, 10	
	48R-3, 50–112	Large green grains
	56R-1, 28–64	Possible synsedimentary clast
Carbonate nodules, clasts, cements	44R-5, 14	Carbonate clasts
	47R-1, 8	White concretion
	47R-3, 10	White concretion
	48R-4, 18	Gray nodule
	48R-4, 30	Gray nodule
	48R-4, 54	Gray nodule
	50R-1, 29	Carbonate nodule
	50R-1, 40–50	Carbonate nodule
	50R-1, 84	Carbonate nodule with yellow sparry calcite
	56R-3, 56–58	Carbonate nodules and cemented clasts
	56R-CC	Calcite localized in fracture
	57R-1, 61	Calcite nodule
	57R-CC, 6–25	Calcite nodule
	58R-1, 78–82	Carbonate zone (nodule?)
	59R-1, 45–52	Micritic interval
Possible firmgrounds	32R-1, 54–57	Green layer; notes indicate an increase in bioturbation
	32R-1, 144–147	Green layer
	32R-2, 22–23	Green layer
	32R-4, 15–16	Green layer
	32R-4, 35–36	Green layer
	32R-4, 74–75	Green layer
	32R-6, 62–64	Green layer
	32R-7, 28–29	Green layer
	32R-7, 49–51	Green layer
	32R-7, 90–91	Green layer
	33R-1, 14–16	Green layer
	33R-1, 64–65	Green layer
	42R-2, 40	Green crust
	42R-2, 84	Green crust
	42R-2, 105	Green crust
	42R-3, 47	Green crust
	42R-4, 70	Green crust
	43R-3, 60	Sharp green/gray contact
	57R-1, 61	Either calcite nodule or cemented zone; associated clast just above
Coal (vitrinite) fragments	40R-1, 107	Dark gray organic matter
	44R-1, 40	Pyritized organic matter
	51R-4, 26	Coal fragment
Sand beds	1R-3, 115.5–122.5	
	10R-3, 33–34	
	10R-4, 11–25	
	10R-CC, 13–25	
	12R-2, 124–130	
	12R-3, 12–16	
	12R-3, 54–58	
	14R-1, 80–92	
	17R-1, 47–49	
	17R-2, 71.5–82.5	
	24R-4, 43–45	

Table T5 (continued).

Interval of interest	Core, section, interval (cm)	Comment
	26R-1, 92–96	
	51R-2, 74–80	
	51R-2, 107–112	
	51R-3, 25–35	
	51R-3, 60–65	
	51R-4, 25–37	
	55R-1, 0–44	
	55R-1, 44–50	
	55R-1, 60–80	
	56R-1, 28–64	
	57R-1, 0–12	Well-sorted calcite-cemented sandstone; calcite fills vertical fractures
	59R-1, 23–36	
	63R-1, 46–85	
	63R-2, 0–15	

Table T6. Results of X-ray diffraction analysis, random bulk powder, Hole C0002B. (**See table notes.**) (**Continued on next page.**)

			Peak intensity (counts/step)				Integrated peak area (total counts)				Abundance calculated from SVD normalization factor: Absolute (wt%)					Normalized (wt%)			
Unit	Core, section, interval (cm)	Depth CSF (m)	Total clay	Quartz	Plagioclase	Calcite	Total clay	Quartz	Plagioclase	Calcite	Total clay	Quartz	Plagioclase	Calcite	Total	Total clay	Quartz	Plagioclase	Calcite
	315-C0002B-																		
II	1R-2, 0	476.43	43	1,096	181	151	4,038	39,931	13,664	6,896	48.3	22.3	15.6	4.3	90.5	53.4	24.6	17.3	4.7
	4R-1, 84	504.35	43	1,117	189	54	3,790	42,454	15,130	2,450	46.6	23.7	17.6	0.1	88.1	52.9	26.9	20.0	0.1
	4R-2, 0	504.61	41	1,294	220	64	3,529	46,824	17,372	2,155	45.4	26.2	20.6	0.1	92.3	49.2	28.4	22.3	0.1
	8R-2, 0	534.42	47	964	151	74	4,188	36,551	12,634	3,254	49.1	20.3	14.4	0.1	83.8	58.5	24.2	17.1	0.1
	8R-3, 73	535.47	37	1,211	209	94	3,393	43,038	15,791	4,331	43.2	24.1	18.6	1.2	87.2	49.6	27.6	21.3	1.4
	9R-3, 0	545.00	44	944	155	82	4,125	36,072	12,028	3,332	48.0	20.0	13.6	0.1	81.7	58.7	24.5	16.6	0.1
	9R-4, 123	546.55	44	1,022	173	57	4,445	37,235	11,907	2,493	51.0	20.7	13.3	0.1	85.0	60.0	24.3	15.6	0.1
	10R-2, 0	553.42	41	1,000	179	116	3,479	37,251	13,368	5,308	42.6	20.8	15.5	2.7	81.7	52.2	25.5	19.0	3.3
	10R-3, 23	553.96	36	1,152	240	78	3,261	43,268	16,426	3,351	42.3	24.2	19.5	0.1	86.2	49.1	28.1	22.6	0.1
	11R-3, 0	564.33	44	1,037	188	112	4,265	38,419	13,200	4,090	50.2	21.4	15.0	0.5	87.1	57.6	24.5	17.3	0.6
	11R-4, 84	565.48	28	1,117	207	185	2,570	39,792	16,524	7,932	35.9	22.3	20.0	6.6	84.8	42.3	26.3	23.6	7.8
	12R-2, 65	573.07	47	1,183	233	90	3,553	43,483	18,278	4,143	46.6	24.2	22.0	0.8	93.5	49.8	25.9	23.5	0.8
	13R-2, 0	581.92	42	1,211	227	91	3,267	44,768	14,982	3,988	41.3	25.2	17.5	0.9	84.8	48.7	29.7	20.6	1.0
	13R-3, 24	582.48	39	1,251	224	85	3,508	44,534	15,843	3,670	44.3	25.0	18.6	0.3	88.1	50.3	28.3	21.1	0.3
	15R-3, 32	602.66	38	1,645	313	46	2,642	56,053	22,987	1,182	40.3	31.5	28.1	0.1	100.0	40.3	31.5	28.1	0.1
	16R-3, 0	611.42	40	1,256	238	117	3,123	44,977	16,417	4,999	40.9	25.3	19.4	2.2	87.9	46.6	28.7	22.1	2.5
	16R-4, 9	611.92	34	1,403	292	91	2,852	50,868	20,148	3,589	40.6	28.6	24.4	0.3	93.9	43.3	30.5	26.0	0.3
	16R-4, 127	613.10	38	1,361	252	97	2,754	51,356	18,752	4,753	38.7	29.0	22.5	1.9	92.0	42.0	31.5	24.4	2.1
	17R-4, 27	623.01	33	1,348	240	98	3,146	48,218	17,726	4,134	41.9	27.1	21.1	0.9	91.1	46.0	29.8	23.2	1.0
	19R-2, 127	640.19	39	1,514	308	71	3,228	52,108	21,536	2,469	45.3	29.2	26.1	0.1	100.7	45.0	29.0	25.9	0.1
	19R-3, 0	640.32	51	1,240	232	33	4,130	43,826	17,836	1,542	51.8	24.3	21.2	0.1	97.5	53.2	25.0	21.7	0.1
	19R-4, 87	641.61	25	519	298	65	2,242	19,890	19,919	4,426	35.9	10.5	25.7	2.8	74.9	48.0	14.0	34.3	3.7
	20R-2, 125	649.68	48	1,238	202	170	3,440	44,752	15,126	7,437	43.3	25.1	17.6	5.2	91.2	47.4	27.6	19.3	5.7
	20R-3, 57	650.41	34	1,346	231	129	2,500	46,181	18,179	5,536	36.0	26.0	22.0	3.3	87.3	41.3	29.8	25.2	3.8
	21R-2, 43	658.35	34	1,259	262	190	2,622	45,299	17,147	8,317	36.6	25.5	20.6	6.9	89.6	40.9	28.5	22.9	7.7
	21R-3, 0	658.91	39	1,245	219	241	3,254	44,025	16,702	10,326	42.7	24.7	19.8	9.1	96.3	44.3	25.6	20.6	9.5
	21R-4, 28	659.60	25	1,475	247	251	1,602	51,599	19,726	10,201	28.2	29.3	24.1	9.8	91.4	30.9	32.0	26.4	10.8
	23R-2, 66	677.08	44	1,347	238	70	3,316	46,163	16,904	3,606	43.1	25.9	20.0	0.2	89.2	48.3	29.0	22.4	0.2
	23R-3, 0	677.83	38	1,242	222	49	3,725	44,760	16,029	1,739	46.5	25.0	18.8	0.1	90.4	51.4	27.7	20.8	0.1
	24R-2, 0	685.92	35	1,280	266	124	2,725	47,535	19,183	5,070	38.9	26.7	23.2	2.4	91.3	42.6	29.3	25.5	2.7
	24R-3, 71	687.05	33	1,452	285	114	2,609	52,627	19,777	4,691	37.9	29.7	23.8	1.9	93.3	40.6	31.8	25.6	2.0
	27R-2, 0	714.12	37	1,135	184	32	3,733	41,313	15,262	1,409	46.2	23.0	17.9	0.1	87.2	52.9	26.4	20.5	0.1
	28R-2, 30	724.22	37	1,437	272	44	2,854	52,383	21,236	1,379	41.3	29.4	25.8	0.1	96.6	42.7	30.5	26.7	0.1
	29R-2, 0	733.43	35	1,486	325	121	2,739	53,607	25,240	5,666	43.2	30.0	31.2	2.8	107.3	40.3	28.0	29.1	2.6
	30R-1, 124	742.75	30	1,091	247	75	2,483	52,719	23,998	4,022	39.7	29.6	29.7	0.9	99.9	39.8	29.6	29.7	0.9
	30R-2, 0	742.92	31	1,189	203	103	3,157	42,999	16,985	4,464	41.8	24.1	20.3	1.6	87.7	47.6	27.4	23.2	1.8
	31R-1, 127	752.28	40	1,257	232	151	2,974	44,129	16,362	6,376	39.5	24.8	19.5	4.2	87.9	44.9	28.2	22.1	4.7
	32R-2, 67	762.59	45	1,271	198	114	3,670	46,314	15,807	5,116	45.9	26.0	18.4	2.0	92.2	49.7	28.2	19.9	2.1
	32R-2, 89	762.81	40	1,222	222	155	3,160	45,308	17,195	6,172	41.9	25.4	20.5	3.7	91.5	45.8	27.8	22.4	4.0
	32R-5, 0	764.31	28	1,311	309	80	2,427	47,857	20,777	3,363	37.0	26.9	25.5	0.4	89.8	41.2	29.9	28.4	0.4

Table T6 (continued).

Unit	Core, section, interval (cm)	Depth CSF (m)	Peak intensity (counts/step)				Integrated peak area (total counts)				Abundance calculated from SVD normalization factor: Absolute (wt%)					Normalized (wt%)			
			Total clay	Quartz	Plagioclase	Calcite	Total clay	Quartz	Plagioclase	Calcite	Total clay	Quartz	Plagioclase	Calcite	Total	Total clay	Quartz	Plagioclase	Calcite
	33R-1, 85	770.86	37	1,118	279	82	3,142	40,974	18,894	3,585	43.1	22.8	23.0	0.4	89.3	48.2	25.5	25.8	0.5
	33R-2, 40	771.40	36	1,136	232	65	2,629	40,578	16,113	3,098	36.0	22.8	19.4	0.3	78.4	45.9	29.0	24.7	0.3
	37R-2, 0	806.92	36	1,410	339	117	2,695	50,509	23,646	4,949	41.7	28.3	29.2	2.1	101.3	41.2	27.9	28.9	2.0
	38R-3, 0	817.83	37	1,477	282	95	2,642	52,551	21,853	4,414	39.8	29.5	26.7	1.4	97.4	40.8	30.3	27.4	1.4
	38R-4, 13	818.38	34	1,249	194	69	3,058	45,028	15,011	3,925	39.2	25.4	17.5	0.9	83.1	47.2	30.5	21.1	1.1
															Average:	47.0	27.8	23.2	2.1
III	40R-2, 0	835.42	36	1,084	225	164	2,354	39,197	17,606	6,976	34.6	21.9	21.6	5.5	83.6	41.3	26.2	25.8	6.6
	40R-3, 98	836.82	32	900	173	256	2,909	32,780	14,583	12,583	38.4	18.2	17.5	12.8	86.9	44.2	21.0	20.2	14.7
	41R-3, 40	846.74	28	1,406	288	96	2,258	50,298	21,929	4,304	36.1	28.3	27.0	1.6	93.0	38.8	30.4	29.0	1.7
	41R-4, 8	846.83	35	785	222	264	3,183	29,420	15,769	14,003	42.2	16.2	19.3	14.5	92.1	45.8	17.6	20.9	15.7
	42R-1, 16	853.17	41	1,045	176	182	3,925	37,935	13,880	8,238	47.5	21.1	16.1	6.2	90.9	52.3	23.2	17.7	6.8
	42R-1, 31	853.32	41	726	142	152	3,580	25,838	12,224	6,393	43.4	14.1	14.5	4.5	76.4	56.7	18.5	18.9	5.8
	43R-1, 17	862.68	33	649	141	445	2,937	22,648	12,630	19,523	38.0	12.4	15.3	22.2	87.9	43.2	14.1	17.4	25.3
	43R-1, 40	862.91	43	618	148	497	3,071	22,478	13,362	21,192	39.9	12.2	16.3	24.3	92.7	43.1	13.2	17.6	26.2
	43R-5, 40	868.16	30	776	141	372	2,711	27,565	10,467	18,641	33.9	15.4	12.2	21.1	82.6	41.1	18.6	14.7	25.6
	44R-1, 124	873.25	31	1,057	170	246	3,315	37,315	14,809	9,240	42.2	20.8	17.5	7.9	88.5	47.7	23.5	19.8	9.0
	44R-2, 48	873.90	43	737	123	285	3,521	26,922	10,290	14,756	41.7	14.9	11.8	15.5	83.8	49.7	17.8	14.0	18.5
	44R-4, 125	877.49	32	1,015	178	396	3,040	35,449	13,279	16,539	38.8	19.8	15.6	17.8	92.0	42.2	21.6	16.9	19.3
	45R-1, 44	881.95	32	1,869	389	29	1,589	61,370	29,350	1,128	34.2	34.6	36.9	0.1	105.8	32.4	32.7	34.9	0.1
	46R-3, 8	893.92	36	939	131	511	2,650	33,640	10,634	21,884	33.3	19.0	12.1	25.2	89.6	37.2	21.2	13.5	28.1
	46R-4, 0	894.82	37	830	167	567	2,991	30,039	13,365	22,733	38.9	16.7	15.9	26.1	97.6	39.8	17.1	16.3	26.7
	46R-5, 94	896.17	35	935	163	307	3,061	33,400	14,508	12,983	39.8	18.6	17.4	13.1	88.9	44.8	20.9	19.5	14.8
	47R-1, 37	900.88	32	1,093	138	524	2,999	36,526	11,900	19,849	37.4	20.6	13.6	22.2	93.8	39.9	21.9	14.5	23.6
	47R-1, 61	901.12	40	863	141	309	2,829	31,713	11,408	14,382	35.4	17.8	13.3	15.3	81.7	43.3	21.7	16.2	18.7
	47R-3, 38	903.71	32	865	143	419	3,063	30,117	11,642	23,433	38.3	16.8	13.6	27.0	95.7	40.1	17.5	14.2	28.2
	48R-2, 35	911.77	34	896	139	324	3,293	31,614	12,629	14,929	40.9	17.6	14.8	15.6	88.9	46.0	19.8	16.6	17.6
	48R-5, 0	915.25	41	896	143	225	3,952	31,947	11,927	12,610	46.8	17.7	13.6	12.1	90.3	51.9	19.6	15.1	13.4
	48R-6, 65	916.32	36	814	130	221	3,579	29,965	12,373	9,932	43.4	16.5	14.5	9.0	83.4	52.1	19.8	17.3	10.7
	48R-6, 89	916.56	41	814	131	298	3,180	29,036	11,040	17,373	38.9	16.1	12.8	19.1	86.8	44.8	18.6	14.7	21.9
	49R-1, 96	920.47	39	798	132	222	3,497	29,366	9,830	13,709	41.0	16.3	11.0	14.1	82.4	49.7	19.8	13.4	17.1
	49R-1, 121	920.72	42	815	121	290	4,058	29,328	10,605	13,829	47.1	16.2	11.9	13.8	89.0	52.9	18.2	13.4	15.5
															Average:	44.8	20.6	18.1	16.5
IV	49R-3, 0	921.91	43	868	156	231	3,991	32,084	11,780	9,635	47.0	17.8	13.4	8.2	86.4	54.4	20.6	15.6	9.5
	51R-1, 34	938.85	41	960	132	469	3,516	34,472	11,509	19,827	42.4	19.3	13.0	21.8	96.5	43.9	20.0	13.5	22.6
	51R-5, 0	943.72	43	875	222	66	4,039	31,369	19,175	3,120	52.6	17.0	23.6	0.1	93.3	56.4	18.2	25.3	0.1
	51R-6, 26	944.39	44	1,125	214	100	3,812	39,343	17,877	4,385	49.1	21.8	21.5	1.0	93.4	52.5	23.3	23.0	1.1
	51R-6, 51	944.64	44	552	163	91	4,708	20,780	14,695	4,602	56.5	10.9	17.8	1.4	86.5	65.3	12.5	20.6	1.6
	58R-1, 46	1,005.47	40	956	258	38	3,413	33,943	21,871	1,499	48.2	18.5	27.4	0.1	94.1	51.2	19.6	29.1	0.1
	59R-1, 121	1,010.72	57	982	152	35	5,077	36,399	13,997	1,881	58.8	20.0	16.0	0.1	94.9	62.0	21.1	16.9	0.1
	59R-2, 0	1,010.92	46	1,046	201	107	4,080	38,681	18,562	4,992	52.3	21.3	22.4	1.6	97.6	53.5	21.8	23.0	1.7
	59R-3, 23	1,011.57	35	1,464	263	65	3,188	50,557	23,845	2,303	46.6	28.2	29.4	0.1	104.3	44.7	27.0	28.2	0.1
	60R-1, 69	1,014.70	35	1,392	278	66	3,053	48,604	23,175	2,529	44.9	27.1	28.6	0.1	100.7	44.6	26.9	28.4	0.1
	61R-2, 121	1,021.13	54	1,027	177	35	5,707	36,525	17,152	1,731	67.3	19.8	20.1	0.1	107.4	62.7	18.5	18.7	0.1
	61R-3, 0	1,021.33	51	1,040	202	69	4,658	39,214	14,991	3,162	55.3	21.7	17.3	0.1	94.4	58.6	23.0	18.4	0.1
	61R-4, 22	1,021.97	60	729	109	52	5,664	27,294	10,526	2,047	62.5	14.7	11.5	0.1	88.8	70.4	16.6	12.9	0.1
	62R-1, 50	1,023.51	39	1,041	286	69	3,330	35,424	23,778	3,766	48.7	19.3	30.0	0.5	98.5	49.5	19.6	30.4	0.5
	62R-2, 0	1,024.01	57	1,163	172	62	5,322	40,580	15,530	2,418	62.2	22.4	17.8	0.1	102.4	60.7	21.8	17.4	0.1
	63R-1, 120	1,033.71	51	1,143	163	53	4,885	40,340	13,959	3,130	56.7	22.3	15.8	0.1	95.0	59.7	23.5	16.6	0.1
	64R-1, 39	1,042.40	40	1,046	160	69	4,152	37,829	14,396	3,667	49.9	21.0	16.7	0.1	87.7	56.9	23.9	19.1	0.1
	64R-2, 0	1,043.01	36	1,549	386	57	2,908	50,806	28,102	2,023	46.9	28.2	35.3	0.1	110.5	42.5	25.5	31.9	0.1
	65R-1, 105	1,047.56	43	1,134	265	62	3,257	40,282	20,994	3,493	45.8	22.3	25.9	0.2	94.1	48.6	23.7	27.5	0.2
	65R-2, 125	1,049.18	52	994	168	36	4,952	37,941	14,351	1,847	57.7	20.9	16.4	0.1	95.2	60.7	22.0	17.3	0.1
															Average:	54.9	21.5	21.7	1.9

Notes: CSF = core depth below seafloor. SVD = singular value decomposition.

Table T7. Nannofossil events, Site C0002. (See table notes.)

Zone	Age (Ma)	Event	Top		Bottom		Mean depth CSF (m)	Range (±m)
			Core, section, interval (cm)	Depth CSF (m)	Core, section, interval (cm)	Depth CSF (m)		
	<0.063	X *Gephyrocapsa* spp. (>3.5 µm)–*Emiliania huxleyi*	315-C0002C- 1H-CC, 0–5	6.47	315-C0002C-			
	0.063	X *Gephyrocapsa* spp. (>3.5 µm)–*Emiliania huxleyi*	315-C0002D- 1H-CC, 27–32	5.85	315-C0002D-		5.85	
NN21	0.291	FO *Emiliania huxleyi*	4H-CC, 0–5	34.10	5H-CC, 0–5	43.52	38.81	4.71
NN20	0.436	LO *Pseudoemiliania lacunosa*	4H-CC, 0–5	34.10	5H-CC, 0–5	43.52	38.81	4.71
	0.9	LCO *Reticulofenestra asanoi*	10H-CC, 0–5	91.06	11H-CC, 0–5	100.70	96.41	4.82
	1.04	RE *Gephyrocapsa* spp. (≥4 µm)	15X-CC, 19–24	137.46			137.46	
	1.078	FCO *Reticulofenestra asanoi*	16H-CC, 0–5	158.91			158.91	
	1.24	LO *Gephyrocapsa* spp. (>5.5 µm)	315-C0002B-		315-C0002B- 1R-CC, 0–23.5	478.28		
	1.34	LO *Helicosphaera sellii*	2R-CC, 0–5	485.98	3R-CC, 11.5–16.5	495.37	490.68	4.69
	1.46	FCO *Gephyrocapsa* spp. (>5.5 µm)	13R-CC, 0–5	584.35	14R-CC, 0–5	592.88	588.62	4.26
	1.56–1.62	FO *Gephyrocapsa* spp. (>5.5 µm)	20R-CC, 8–13	653.08	21R-CC, 5.5–10.5	661.06	657.07	3.99
	1.60	LO *Calcidiscus macintyrei* (≥11 µm)	40R-CC, 0–5	837.56	41R-CC, 0–5	848.38	842.97	5.41
	1.67	FO *Gephyrocapsa* spp. (>3.5 µm)	40R-CC, 0–5	837.56	41R-CC, 0–5	848.38	842.97	5.41
NN19	2.06	LO *Discoaster brouweri*	41R-CC, 0–5	848.38	42R-CC, 0–5	859.11	853.75	5.37
NN18	2.39–2.51	LO *Discoaster pentaradiatus*	42R-CC, 0–5	859.11	43R-CC, 0–5	870.52	864.81	5.71
NN17	2.52	LO *Discoaster surculus*	45R-CC, 0–5	886.20	46R-CC, 0–5	897.36	891.78	5.58
	2.87	LO *Discoaster tamalis*	42R-CC, 0–5	859.11	43R-CC, 0–5	870.52	864.81	5.71
	3.65	LO *Sphenolithus* spp.	47R-CC, 0–5	906.91	48R-CC, 0–5	916.77	911.84	4.93
NN16	3.79	LO *Reticulofenestra pseudoumbilicus* (>7 µm)	48R-CC, 0–5	916.77	49R-CC, 13–18	923.71	920.24	3.47
	5.04	LO *Ceratolithus acutus*	48R-CC, 0–5	916.77	49R-CC, 13–18	923.71	920.24	3.47
NN13	5.12	FO *Ceratolithus rugosus*	48R-CC, 0–5	916.77	49R-CC, 13–18	923.71	920.24	3.47
NN12	5.59	LO *Discoaster quinqueramus*	49R-CC, 13–18	923.71	50R-CC, 0–5	930.10	926.91	3.20
	5.90	LO *Nicklithus amplificus*	65R-CC, 0–5	1049.38	66R-CC, 6–11	1052.40	1050.89	1.51

Notes: CSF = core depth below seafloor. X = crossover in abundance, FO = first occurrence, LO = last occurrence, LCO = last consistent occurrence, RE = reentrance, FCO = first consistent occurrence.

Table T8. Calcareous nannofossil range chart, Hole C0002B. This table available in an oversized format.

Table T9. Calcareous nannofossil range chart, Holes C0002C and C0002D. (See table notes.)

Epoch	Zone	Core, section, interval (cm)	Depth CSF (m)	Abundance	Preservation	*Calcidiscus leptoporus*	*Calcidiscus macintyrei*	*Coccolithus pelagicus* (without bar)	*Discoaster surculus*	*Emiliania huxleyi*	*Florisphaera profunda*	*Gephyrocapsa* spp. medium (>3.5–4 µm)	*Gephyrocapsa* spp. medium II (>4–5.5 µm)	*Gephyrocapsa* spp. smaller (3.5 µm)	*Helicosphaera ampliaperta*	*Helicosphaera carteri*	*Helicosphaera* sp.	*Helicosphaera wallichii*	*Oolithotus fragilis*	*Pontosphaera japonica*	*Pontosphaera multipora*	*Pseudoemiliania lacunosa*	*Pseudoemiliania ovata*	*Reticulofenestra asanoi*	*Reticulofenestra minutula*	*Reticulofenestra pseudoumbilicus* (>7 µm)	*Rhabdosphaera clavigera*	*Scapholithus fossilis*	*Scyphosphaera apsteinii*	*Sphenolithus grandis*	*Sphenolithus* spp.	*Syracosphaera pulchra*	*Syracosphaera* spp.	*Umbellosphaera irregularis*	*Umbellosphaera tenuis*	*Umbilicosphaera foliosa*	*Umbilicosphaera hulburtiana*	*Umbilicosphaera sibogae*
Pleistocene	NN21	315-C0002C- 1H-CC, 0–5	6.47	A	M	C				A	A	A	C	C		F		F																F		F
		315-C0002D- 1H-CC, 27–32	5.85	A	G	R				C	A	A	C	A		F		F									R				R				C		F
		2H-CC, 32–37	15.38	A	G	F				C	A	A	C	D		F											F					F	F	F		F		F
		3H-CC, 0–5	23.37	A	G	F				C	C	A	C	A		F	F																	F		F		
		4H-CC, 0–5	34.10	A	G	R				C	C	A	C	A		F																F			F		F	
	NN19	5H-CC, 0–5	43.52	A	G						A	C		D		F		F				R	C							F				F			
		6H-CC, 0–5	52.83	A	G						A		A	D		F							C								F	F		F			
		7H-CC, 9–14	62.68	A	G						A	A	C	D		C						C	C					F				F		F	C		
		8H-CC, 0–5	71.94	C	G	F					A	C	C	D					R		R	F	C										R	F			F
		9H-CC, 0–5	81.64	A	G	F					A	C	F	A			F					C	C									F			C		C
		10H-CC, 0–5	91.06	A	G	C					A	C	F	D			F			R		C	C									F		F			
		11H-CC, 0–5	100.70	A	G	C					A	C	C	D		F						F	C	R					R			F	F	F	F		
		12H-CC, 7–12	110.20	A	G	F	R				A	C		D		F	F		F		R	C	C	F			R				R			F	C		F
		13H-CC, 6–11	119.77	A	G	F			F		A	F	F	D								C	C	F										F	C		F
		14H-CC, 0–5	129.02	F	M	C					A			D								C	A	F													
		15X-CC, 19–24	137.46	C	M	C					A	C	C	A		F							C	C	C													
		16H-CC, 0–5	158.91	C	M						A	C		D		C							C	C														
		17X-CC, 4–9	161.04	F	M	C					A	C		D									C	C		C						C						
		18H-CC, 0–5	203.57	A	M	C				R	A	C		D		R				R		R	C	C	C							F			R		

Notes: CSF = core depth below seafloor. Abundance: D = dominant, A = abundant, C = common, F = few, R = rare. Preservation: G = good, M = medium.

Table T10. Planktonic foraminifer events, Site C0002. (See table notes.)

Zone	Age (Ma)	Event	Top		Bottom		Mean depth CSF (m)	Range (±m)
			Core, section, interval (cm)	Depth CSF (m)	Core, section, interval (cm)	Depth CSF (m)		
			315-C0002B-		315-C0002B-			
	1.3	LO *Globoturborotalita obliquus*			2R-CC, 0.0–5.0	485.98	<485.98	
	1.8	LO *Neogloboquadrina asanoi*	41R-CC, 0.0–5.0	848.38	42R-CC, 0.0–5.0	859.11	853.75	5.37
N.22	1.93	FO *Truncorotalia truncatulinoides*	31R-CC, 0.0–5.0	753.86	32R-CC, 0.0–5.0	767.20	760.53	6.67
	2.3–2.5	FO *Globoconella inflata* modern form	42R-CC, 0.0–5.0	859.11	43R-CC, 0.0–5.0	870.52	864.82	5.70
N.21	3.35	FO *Truncorotalia tosaensis*	42R-CC, 0.0–5.0	859.11	43R-CC, 0.0–5.0	870.52	>870.52	
	3.47	LO *Dentoglobigerina altispira*			49R-CC, 13.0–18.0	923.71	<923.71	
	3.59	LO *Sphaeroidinellopsis seminulina*	47R-CC, 0.0–5.0	906.91	48R-CC, 0.0–5.0	916.77	911.84	4.93
	3.85	LO *Hirsutella margaritae*			52R-CC, 0.0–5.0	949.06	<949.06	
	4.08	SD1 *Pulleniatina* spp.	46R-CC, 0.0–5.0	897.36	49R-CC, 13.0–18.0	923.71	910.54	13.17
	4.31	FO *Truncorotalia crassaformis*	48R-CC, 0.0–5.0	916.77	49R-CC, 13.0–18.0	923.71	920.24	3.47
	4.37	LO *Globoturborotalita nepenthes*	51R-CC, 0.0–5.0	946.24	52R-CC, 0.0–5.0	949.06	947.65	1.41
	5.57	FO *Globorotalia tumida*	49R-CC, 13.0–18.0	923.71	50R-CC, 0–5	930.10	926.91	3.20
	6.2	FO *Globigerinoides conglobatus*	57R-CC, 0–5	996.35	58R-CC, 0–5	1007.50	1001.93	5.58
>N.17b	<6.6	FO *Pulleniatina primalis*	66R-CC, 6.0–11.0	1052.40			>1052.40	

Notes: CSF = core depth below seafloor. FO = first occurrence, LO = last occurrence, SD = change in coiling direction from sinistral to dextral.

Table T11. Planktonic foraminifer range chart, Site C0002. (See table notes.) (Continued on next page.)

Epoch	Zone	Core, section, interval (cm)	Depth CSF (m)	Abundance	Preservation	*Dentoglobigerina altispira*	*Globigerina bulloides*	*Globigerina falconensis*	*Globigerinella obesa*	*Globigerinella siphonifera*	*Globigerinita glutinata*	*Globigerinoides bolii*	*Globigerinoides conglobatus*	*Globigerinoides ruber*	*Globigerinoides sacculifer*	*Globoconella* cf. *conoidea*	*Globoconella conomiozea*	*Globoconella inflata* modern form	*Globoconella inflata* transitional form	*Globoconella puncticulata*	*Globoconella sphericomiozea*	*Globoquadrina venezuelana*	*Globorotalia scitula*	*Globorotalia tumida*	*Globoturborotalita decoraperta*	*Globoturborotalita extremus*	*Globoturborotalita nepenthes*	*Globoturborotalita obliquus*	*Globoturborotalita woodi*	*Hirsutella margaritae*	*Menardella menardii*	*Menardella pseudomiocenica*	*Neogloboquadrina acostaensis* dextral form	*Neogloboquadrina asanoi*	*Neogloboquadrina dutertrei*	*Neogloboquadrina humerosa*	*Neogloboquadrina incompta*	*Neogloboquadrina kagaensis*	*Neogloboquadrina pachyderma* dextral form	*Neogloboquadrina pachyderma* sinistral form	*Neogloboquadrina praehumerosa*	*Orbulina universa*	*Pulleniatina finalis*	*Pulleniatina* spp. dextral	*Pulleniatina* spp. sinistral	*Sphaeroidinella dehiscens*	*Sphaeroidinellopsis seminulina*	*Sphaeroidinellopsis subdehiscens*	*Truncorotalia crassaformis*	*Truncorotalia tosaensis*	*Truncorotalia truncatulinoides*	*Turborotalita quinqueloba*
		315-C0002B-																																															
		1R-CC, 0–23.5	478.28	R	G																																												
		2R-CC, 0–5	485.98	C	G		+	+			+			+	+			+	+															+														
		3R-CC, 11.5–16.5	495.37	B	B																																												
		4R-CC, 0–5	506.29	B	B																																												
		5R-CC, 11.5–16.5	508.93	B	B																																												
		6R-CC, 18.5–23.5	515.22	C	G		C	+			A			R				R	C															C		A	+											
		7R-CC, 17–22	524.57	R	M			+										+	+															+														
		8R-CC, 17–22	535.90	R	M		+	+			+			+	+			+	+				+											+		+	+											
		9R-CC, 25.5–35	547.39	B	B																																												
		10R-CC, 0–5	555.27	B	B																																												
		11R-CC, 0–5	566.48	A	G		C	C		+	A		+	C	+			C	+	+			+	+	+						+			R		R		+										
		12R-CC, 0–5	574.50	A	M		C	+			+		+	R	+			R	+				+	+							+			A		C	+	+										
		13R-CC, 0–5	584.35	B	B																																												
		14R-CC, 0–5	592.88	B	B																																												
	N.22	15R-CC, 0–5	602.83	R	P		C	+			A			R	+																+			C		C										A	
		16R-CC, 14.5–19.5	613.76	C	G		A	C	+		C			C	+			+	+				+			+									A		+	+									+	+
		17R-CC, 3–8	623.91	A	G		A	R			R			R	+			R	R							+									C		C										+	+
Pleistocene		18R-CC, 16.5–21.5	628.97	A	G		C	C			C		+	C	+			A	C					+					+			+			R		R	+									+	+
		19R-CC, 0–5	641.76	R	P		C	R			A			+	+				+	+			+			+									C		A	+										C
		20R-CC, 8–13	653.08	R	P		A	+			A			R											R										C		A										+	
		21R-CC, 5.5–15	661.06	R	P						+			+				+																															
		22R-CC, 0–5.5	666.24	A	M		+	R			C			+				C	C													+			A		A	+									+	
		23R-CC, 19–24	679.34	B	B																																												
		24R-CC, 25–25.5	688.05	C	P		C	+			A			C	R			+	+	+			+	+						+							C	+									R	
		25R-CC, 11–16	696.31	B	B																																												
		26R-CC, 0–5	704.83	A	M		+	+			C			+	+			A	C	+			+	+											A		R	+									C	
		27R-CC, 0–5	715.79	R	M		R	+			A			R				+	+	R						+									C		A										+	+
		28R-CC, 0–5	725.55	R	M		+	+			R			+	+			A	A	C				+							+				C		C					R			+		+		
		29R-CC, 18–23	734.76	C	M		C	+			R			+	+			C	A	A			+	+											C	+									+		+		
		30R-CC, 24–29	744.65	R	P		+	+			+			+				+	+	+															+		+									+			
		31R-CC, 0–5	753.86	R	P		+	+			+							+	+				+											+		+	+											
		32R-CC, 0–5	767.20	B	B																																												
		33R-CC, 0–5	773.07	R	P			+			+			+	+	+							+											+		+											
	N.21	36R-CC, 0–5	797.70	C	M		+				A			C	+			+	+	+			+						+					C		C	+		+								C	
		37R-CC, 21–26	808.05	R	P																																											+
		38R-CC, 0–5	820.04	R	M		+	+			+			+	+			+	+	+															+		+										+	

Table T11 (continued).

Epoch	Zone	Core, section, interval (cm)	Depth CSF (m)	Abundance	Preservation	*Dentoglobigerina altispira*	*Globigerina bulloides*	*Globigerina falconensis*	*Globigerina obesa*	*Globigerinella siphonifera*	*Globigerinita glutinata*	*Globigerinoides bolii*	*Globigerinoides conglobatus*	*Globigerinoides ruber*	*Globigerinoides sacculifer*	*Globoconella* cf. *conoidea*	*Globoconella conomiozea*	*Globoconella inflata* modern form	*Globoconella inflata* transitional form	*Globoconella puncticulata*	*Globoconella sphericomiozea*	*Globoquadrina venezuelana*	*Globorotalia scitula*	*Globorotalia tumida*	*Globoturborotalita decoraperta*	*Globoturborotalita extremus*	*Globoturborotalita nepenthes*	*Globoturborotalita obliquus*	*Globoturborotalita woodi*	*Hirsutella margaritae*	*Menardella menardii*	*Menardella pseudomiocenica*	*Neogloboquadrina acostaensis* dextral form	*Neogloboquadrina asanoi*	*Neogloboquadrina dutertrei*	*Neogloboquadrina humerosa*	*Neogloboquadrina incompta*	*Neogloboquadrina kagaensis*	*Neogloboquadrina pachyderma* dextral form	*Neogloboquadrina pachyderma* sinistral form	*Neogloboquadrina praehumerosa*	*Orbulina universa*	*Pulleniatina finalis*	*Pulleniatina* spp. dextral	*Pulleniatina* spp. sinistral	*Sphaeroidinella dehiscens*	*Sphaeroidinellopsis seminulina*	*Sphaeroidinellopsis subdehiscens*	*Truncorotalia crassaformis*	*Truncorotalia tosaensis*	*Truncorotalia truncatulinoides*	*Turborotalita quinqueloba*
Pleistocene	N.21	39R-CC, 0–5	826.05	R	P			+			+			+	+			+																														
		40R-CC, 0–5	837.56	R	M		+							+	+			+	+	+				+											+	+		+									
		41R-CC, 0–5	848.38	R	M		+	+						+	+			+	+	+				+	+										+	+		+									
		42R-CC, 0–5	859.11	C	P		+	+			C			+	+			C	C	C													R			+		A	+								
	N.18–?N.17b	43R-CC, 0–5	870.52	C	P		R				A			+	R					R				+	+										+	C		A	+		R						
		44R-CC, 0–5	879.48	R	P		C	+		+	A			R	R					+				+				+							+		R	C	+	+	R				R		
		45R-CC, 0–5	886.20	R	P		+	R			C			+	+				C	A				+			+						+					+	+	+	R						
		46R-CC, 0–5	897.36	A	M		+	+			A		+	R	+				+	A				+				+							+	A		+	+	+	+			+			
		47R-CC, 0–5	906.91	R	P		+				+				+					+		+													+		+	+				+				+
		48R-CC, 0–5	916.77	C	M		R		+	+	A				R		+			+				+				+	+		+					C		A	+		+	+	+	+			+
		49R-CC, 13–18	923.71	C	M	+	+	+			C	R	+		+	+				+	+			+	+			+					+				+		R	A				+				+
		50R-CC, 0–5	930.10	R	P		+								+													+			+							+									
		51R-CC, 0–5	946.24	R	P																																		+									
		52R-CC, 0–5	949.06	A	M	+	R	+					+	+	C									+				R	C		+					R	+			A	+	R	C					+
		55R-CC, 0–5	978.38	R	P		+				+	+		+													+				+								A	+	+							
		56R-CC, 0–5	987.97	R	P			+			+															+	+	+												+	+			+					
		57R-CC, 0–5	996.35	R	P						+		+			+														+										+									
		58R-CC, 0–5	1007.50	R	P																																												
		59R-CC, 4.5–9.5	1012.75	R	M	+	+	+				+			+											+	+	+												+		+							
		60R-CC, 0–5	1016.92	B	B																																												
		61R-CC, 29–34	1024.06	R	M						+				+												+	+												+	+								
		62R-CC, 31–36	1026.32	R	P		+	+			+				+													+							+			+	+								
		63R-CC, 25.5–35	1035.28	C	M		+	R			A	+			C	+									+	+		R	R	+			+					C	R	+	+				+	+			
?Miocene		64R-CC, 0–5	1044.40	R	P		+	+			+	+			+														+										+									
		65R-CC, 0–5	1049.38	B	B																																												
		66R-CC, 6–11	1052.40	R	M			+	+		+					+											+	+		+										+	+					+			

Notes: CSF = core depth below seafloor. Abundance: A = abundance, C = common, R = rare, B = barren, + = present. Preservation: G = good, M = medium, P = poor, B = barren.

Table T12. Remanent magnetization, Hole C0002D. (See table notes.) (Continued on next page.)

Core, section, interval (cm)	Demag (mT)	Declination (°)	Inclination (°)	α95	*N*	*k*
315-C0002D-						
20R-1, 90–125	30	**95.50**	**–51.40**	17.8	8	10.7
20R-2, 15–100	30	**61.20**	**–51.40**	17.4	18	4.9
21R-4, 40–60	30	**247.60**	**–49.40**	8.7	5	77.9
23R-1, 115–125	30	**253.40**	**–54.40**	52.0	3	6.7
24R-1, 40–60	30	**270.20**	**–17.30**	41.8	5	4.3
26R-1, 70–85	30	**331.00**	**–48.20**	9.4	4	96.4
27R-1, 50–65	30	**143.60**	**–66.70**	22.6	4	17.5
28R-2, 70–80	30	**122.70**	**–60.60**	33.8	3	14.3
30R-1, 25–40	30	**323.10**	**–59.40**	8.8	4	109.5
31R-1, 15–100	30	**267.90**	**–68.50**	13.8	18	7.3
31R-2, 60–80	30	**280.90**	**–60.30**	14.0	5	30.8
32R-3, 15–30	30	**356.90**	**–50.60**	11.4	4	65.4
32R-4, 25–40	30	**167.90**	**–36.30**	13.3	4	48.5
32R-6, 70–90	30	**302.50**	**–39.30**	11.9	5	42.3
32R-6, 100–115	30	**188.60**	**–19.50**	12.6	4	54.4
33R-1, 50–60	30	**301.90**	**–43.30**	20.5	3	37.1
41R-1, 75–90	30	**331.20**	**–33.70**	86.9	4	2.1
41R-2, 55–70	30	**195.90**	**–9.00**	20.5	4	21.0
41R-4, 65–75	30	218.10	52.30	74.0	3	3.9
42R-2, 15–120	30	161.40	60.40	4.1	21	60.6
42R-3, 0–80	30	263.90	78.30	6.1	11	56.1
42R-3, 100–135	30	94.00	76.50	10.6	3	135.5
43R-2, 0–60	30	273.60	65.40	6.0	7	101.6
43R-3, 40–70	30	336.50	73.70	7.1	6	89.7
43R-6, 0–20	30	345.50	61.40	2.8	4	1090.4
43R-6, 50–70	30	15.00	61.30	13.8	5	31.3
43R-7, 10–35	30	309.40	64.30	4.6	5	278.1
44R-1, 10–70	30	80.10	68.00	6.0	12	53.2
44R-1, 70–100	30	42.10	74.40	6.0	7	101.2
44R-2, 90–140	30	271.40	70.70	4.7	8	139.5
44R-4, 2–32	30	234.20	66.70	15.0	4	38.7
44R-4, 32–62	30	226.40	67.00	9.3	7	43.3
44R-6, 5–41	30	226.30	67.90	12.4	3	99.9
45R-1, 5–35	30	251.40	62.50	8.1	4	130.6
45R-2, 0–26	30	119.20	56.60	31.2	3	16.7
45R-2, 75–100	30	289.20	65.70	26.9	3	22.0
45R-3, 0–20	30	3.00	22.40	62.1	3	13.3
46R-1, 10–100	30	288.40	67.50	3.4	18	102.6
46R-2, 40–95	30	94.30	69.90	3.6	12	143.8
46R-5, 0–40	30	219.60	69.40	9.0	5	72.2
46R-5, 0–70	30	48.00	69.90	7.7	6	77.1
47R-1, 82–128	30	184.80	65.60	6.7	6	101.5
47R-3, 53–85	30	333.60	73.80	4.0	4	527.9
47R-3, 100–135	30	66.00	75.70	3.0	6	510.2
47R-5, 0–73	30	148.30	78.30	4.3	10	128.7
48R-1, 20–120	30	289.20	61.70	3.6	20	82.9
48R-2, 50–139	30	191.70	55.30	7.5	13	31.3
48R-3, 10–40	30	306.00	56.90	17.5	6	15.6
48R-3, 50–65	30	270.60	49.50	18.2	3	47.0
48R-3, 100–140	30	241.80	70.50	11.7	6	33.9
48R-4, 0–80	30	229.20	70.30	5.9	14	46.9
48R-6, 0–58	30	178.30	64.60	8.8	6	59.0
49R-1, 20–88	30	320.70	67.70	7.8	8	51.2
49R-2, 20–60	30	314.70	67.50	5.2	7	136.6
49R-2, 70–100	30	42.80	65.90	10.5	4	78.3
49R-4, 10–40	30	159.50	64.10	9.2	3	181.5
49R-4, 50–80	30	282.90	67.20	7.7	3	255.3
51R-1, 70–110	30	235.80	61.20	10.9	7	31.8
51R-4, 45–100	30	358.30	70.40	8.4	12	22.7
51R-6, 65–85	30	211.30	69.20	10.9	5	50.2
51R-6, 100–120	30	171.50	72.10	12.1	5	41.3
51R-7, 8–15	30	44.99	59.33	—	Discrete	—
51R-7, 15–23	30	32.75	72.10	—	Discrete	—
51R-7, 23–33	30	109.80	78.71	—	Discrete	—
51R-7, 33–43	30	207.06	74.76	—	Discrete	—
51R-7, 43–54	30	319.45	73.38	—	Discrete	—
57R-1, 60–65	30	355.87	82.32	—	Discrete	—
61R-1, 20–47	30	336.90	47.90	11.7	6	33.9

Table T12 (continued).

Core, section, interval (cm)	Demag (mT)	Declination (°)	Inclination (°)	α95	*N*	*k*
61R-2, 0–25	30	9.70	60.80	21.4	4	19.5
62R-1, 15–35	30	0.60	75.10	8.2	4	125.7
63R-1, 15–35	25	208.30	78.50	20.7	3	36.4
64R-1, 40–100	30	94.30	73.90	7.3	7	69.8

Notes: Demag = demagnetization. Measurements made on archive halves, where +*x* = vertical upward direction when core is sitting with single line at the bottom, +*y* = direction to the left along split-core surface when looking upcore, and +*z* = downcore. If inclination is positive (plain text), then the declination needs to be restored to the north (360°); if inclination is negative (bold text), then the declination needs to be restored to the south (180°). α95 = radius of the 95% confidence cone centered around the mean paleomagnetic direction, *N* = number of measurements (= intervals), *k* = Fisher or precision parameter; — = not applicable to discrete measurements.

Table T13. Depth and age of identified paleomagnetic transitions, Holes C0002B and C0002D. (**See table notes.**)

Chron/ Subchron	Event	Depth CSF (m)	Age (Ma)
B C1n	Brunhes/Matuyama boundary	86.24 ± 0.6(?)	0.781
T C1r.1n	Top of Jaramillo	118.8 ± 0.7	0.988
T C2n	Top of Olduvai	842.30 ± 5.3	1.778

Notes: CSF = core depth below seafloor. T = top, B = bottom.

Table T14. Interstitial water geochemistry, Site C0002. (See table notes.) (Continued on next page.)

Core, section	Depth CSF (m)	pH	Alkalinity (mM)	Salinity (refractive index)	Cl (mM)	Br (µM)	SO_4 (mM)	PO_4 (µM)	NH_4 (mM)	Na (mM)	K (mM)	Mg (mM)	Ca (mM)	Li (µM)	B (µM)	Mn (µM)
315-C0002B-																
1R-2	476.58	7.60	18.74	1.33706	370.2	807	0.98	21.2	9.73	347	5.50	11.0	4.14	51.9	200	4.22
4R-2	504.76	7.71	16.85	1.33698	366.9	809	0.89	10.7	8.91	339	5.62	10.3	4.49	35.6	203	1.63
8R-2	534.57	7.56	17.36	1.33748	403.8	162	0.66	8.92	8.38	398	5.92	13.2	5.87	38.5	181	3.44
9R-3	545.15	7.63	17.72	1.33730	395.5	855	1.26	8.25	8.25	367	5.60	11.8	5.59	52.7	166	2.54
10R-2	553.56	7.60	17.55	1.33718	414.4	815	1.62	12.7	8.00	357	5.27	10.3	5.19	56.3	172	3.11
11R-3	564.47	7.66	15.98	1.33775	381.5	864	3.25	6.46	8.25	400	6.14	12.7	6.01	63.7	178	3.31
13R-2	582.07	7.66	16.73	1.33736	402.4	759	0.14	6.46	7.57	374	5.61	11.0	5.83	58.6	160	2.07
16R-3	611.61	7.64	13.61	1.33762	425.3	892	1.25	2.20	6.79	402	5.85	12.7	6.47	71.3	208	3.02
19R-3	640.52	7.58	12.70	1.33772	438.6	919	1.96	7.13	6.76	417	5.44	12.8	6.78	85.2	313	2.44
21R-3	659.10	7.63	11.45	1.33762	429.4	935	0.91	3.32	5.93	391	5.51	10.7	5.76	97.7	367	2.07
23R-3	678.03	7.81	12.48	1.33745	413.4	874	1.19	3.99	5.09	407	5.97	10.6	5.72	88.5	338	2.06
24R-2	686.12	7.81	9.35	1.33754	434.7	675	0.21	2.20	5.47	402	6.82	10.3	5.13	96.7	316	1.07
27R-2	714.27	7.78	11.20	1.33768	443.3	909	1.25	4.44	4.60	394	6.48	11.4	6.63	110	330	2.61
29R-2 (GRIND)	733.52	7.92	8.06	1.33706	385.4	840	0.60	2.87	4.01	363	5.71	8.49	5.18	94.1	255	1.53
30R-2	743.07	7.73	10.68	1.33787	460.4	949	1.17	5.78	4.63	418	6.81	11.9	7.24	124	349	2.40
32R-5	764.50	7.69	9.30	1.33795	474.8	945	1.40	4.89	4.07	429	6.28	12.8	8.23	125	304	3.74
33R-2	771.20	7.74	9.50	1.33799	467.7	962	1.67	3.77	4.13	434	6.32	12.8	8.50	118	297	3.75
37R-2	807.12	7.95	9.88	1.33804	479.3	933	1.18	5.03	3.55	431	6.10	12.1	8.58	137	230	3.56
38R-3	818.03	7.75	10.13	1.33802	477.0	953	0.76	4.79	3.51	445	6.91	11.8	8.33	166	253	3.00
40R-2	835.62	7.76	10.38	1.33816	482.1	932	1.81	ND	3.49	452	7.29	13.2	8.33	194	264	2.66
41R-3	846.53	7.82	9.33	1.33882	478.1	945	1.14	ND	3.47	429	6.92	11.7	7.77	222	263	2.06
43R-5	867.95	7.55	8.67	1.33799	474.1	955	0.71	5.27	3.51	436	6.65	11.5	8.28	239	293	1.20
46R-4	895.01	7.47	7.53	1.33793	472.1	952	1.09	5.27	2.99	440	6.23	11.9	9.13	256	313	2.37
48R-5	915.45	7.48	6.99	1.33790	467.1	948	0.82	ND	2.76	415	5.37	11.7	10.6	254	312	2.81
49R-3	922.11	7.50	5.80	1.33785	465.9	928	0.50	3.34	2.51	410	4.87	11.8	11.0	248	262	3.71
51R-5	943.91	8.02	6.82	1.33742	462.8	913	1.39	ND	2.17	415	3.50	13.1	14.1	219	253	8.01
55R-2	977.70	7.86	4.19	1.33788	460.4	932	1.40	ND	2.16	379	2.65	12.3	16.2	209	220	4.68
56R-2	986.85	8.03	3.58	1.33822	476.0	928	2.64	ND	2.16	410	2.77	13.7	17.8	200	219	9.65
59R-2	1011.12	8.11	3.19	1.33785	457.9	882	3.02	ND	1.55	411	2.17	13.1	18.9	187	222	9.87
61R-3	1021.53	8.22	3.30	1.33764	432.5	850	1.97	ND	1.56	369	2.15	10.0	18.0	184	251	6.81
62R-2	1024.21	7.86	2.85	1.33795	464.0	910	3.70	ND	1.78	356	1.78	12.7	20.6	178	173	7.29
64R-2	1043.20	7.69	3.90	1.33789	455.5	878	3.16	ND	1.92	411	2.92	12.0	20.0	192	325	12.7
315-C0002D-																
1H-2	1.52	7.78	6.90	1.33938	548.9	862	26.2	12.9	0.19	485	11.4	47.9	9.50	72.9	520	8.14
1H-5	4.35	8.27	13.49	1.33930	554.6	898	15.6	25.2	0.78	500	11.9	45.9	6.48	69.6	523	0.80
2H-3	8.81	8.40	27.27	1.33910	556.9	928	1.25	42.9	1.53	464	11.1	40.8	3.15	53.1	528	0.39
2H-7	13.06	8.30	26.05	1.33906	557.1	973	0.78	44.3	2.36	470	11.6	38.8	2.64	48.9	487	0.35
3H-4	19.54	8.10	25.53	1.33901	552.7	966	0.86	62.1	3.75	468	11.1	35.5	2.40	56.2	451	0.46
4H-4	29.20	7.81	17.58	1.33895	547.4	1040	0.13	93.5	5.18	483	10.1	32.3	1.88	59.2	448	0.53
5H-4	38.71	7.76	22.40	1.33895	553.3	1090	0.15	98.9	6.93	489	10.9	30.6	1.93	60.6	418	0.57
6H-5	49.43	7.74	24.65	1.33896	549.8	1120	0.01	96.2	7.86	479	10.1	30.2	2.35	63.1	436	1.30
7H-4	57.74	7.81	13.38	1.33899	554.3	1140	0.09	92.1	9.30	476	10.2	30.2	2.64	57.4	396	1.97
8H-4	66.92	7.77	25.37	1.33896	548.7	1110	0.09	75.7	9.85	481	10.2	29.9	2.83	62.6	378	2.78
9H-5	78.10	7.76	23.92	1.33893	546.0	1170	ND	58.0	11.0	494	10.1	28.1	2.85	61.3	375	3.01
10H-4	86.21	7.72	23.82	1.33891	548.0	1200	ND	59.3	11.9	483	9.47	28.3	2.80	61.1	373	1.80
11H-5	96.72	7.64	23.80	1.33890	536.8	1180	0.09	64.8	11.7	491	9.54	27.5	2.96	55.4	350	1.94
11H-6	98.06	7.82	23.58	1.33884	547.6	1160	0.11	60.7	11.0	464	9.81	27.4	2.80	61.8	339	1.75
12H-5	106.41	7.62	23.99	1.33890	544.7	1170	0.10	88.0	12.0	492	9.33	26.6	3.03	60.2	320	1.63
13H-5	115.81	7.77	24.66	1.33887	542.5	1190	0.11	67.5	12.4	480	9.24	26.5	3.10	56.6	319	1.18
14H-3	121.92	7.82	21.97	1.33779	451.9	992	0.77	82.5	10.3	395	6.78	22.0	2.65	45.2	240	1.47
14H-5	124.74	7.60	25.33	1.33886	539.0	1200	0.08	308	13.3	473	8.79	25.1	3.10	49.0	285	1.46
15X-5	133.18	7.68	29.07	1.33884	532.1	1220	0.28	328	14.2	459	8.61	26.0	3.22	52.2	288	1.51
16H-6	157.09	7.72	29.12	1.33876	528.1	1220	0.09	354	13.1	470	8.79	25.6	2.99	51.8	256	1.17
17X-4	159.77	8.23	9.69	1.33478	153.8	359	1.65	88.0	4.64	148	2.68	4.9	0.65	16.5	88.5	0.45
18H-1	200.42	7.98	25.22	1.33730	503.6	868	2.31	85.3	10.8	376	6.44	18.7	2.38	52.8	191	1.02
18H-2	200.60	7.76	35.52	1.33862	382.2	1200	0.19	259	13.0	470	8.35	25.2	2.96	65.7	258	1.08

Notes: CSF = core depth below seafloor. * = data from shore-based analyses. VSMOW = Vienna standard mean ocean water. ND in SO_4 column = <0.01 mM, ND in PO_4 column = <3.3 µM, ND in Cu column = <35 nM, ND in Pb column = <0.4 nM, NA = not analyzed.

Table T14 (continued).

Core, section, interval (cm)	Depth (mbsf)	Fe (μM)	Si (μM)	Sr (μM)	Ba* (μM)	V* (nM)	Cu* (nM)	Zn* (nM)	Rb* (μM)	Mo* (nM)	Cs* (nM)	Pb* (nM)	U* (nM)	Y* (pM)	$\delta^{18}O$ (‰ VSMOW)*	δD (‰ VSMOW)*
315-C0002B-																
1R-2	476.58	87.6	936	56.8	9.78	44	3320	1350	0.74	430	3.35	2.95	0.92	0.00	–0.79	–12
4R-2	504.76	37.8	671	54.6	13.5	28	1120	1450	0.93	119	4.57	1.86	0.68	0.59	–0.99	–12
8R-2	534.57	44.5	830	69.9	15.1	52	6870	2910	1.03	319	4.30	0.97	2.37	NA	–0.78	–10
9R-3	545.15	34.8	785	67.5	15.9	48	13100	2020	0.87	226	3.32	0.54	2.31	NA	–0.91	–11
10R-2	553.56	48.1	969	65.3	16.5	30	918	1450	0.90	322	3.87	1.79	1.20	0.58	–1.17	–13
11R-3	564.47	39.7	979	75.4	15.0	67	5140	1740	1.03	347	3.81	1.23	2.44	0.25	–1.00	–11
13R-2	582.07	37.7	915	68.6	18.2	24	822	1680	1.00	209	4.60	0.78	1.26	0.32	–1.32	–12
16R-3	611.61	26.6	944	83.9	13.3	30	684	1730	1.08	290	5.50	1.81	1.35	0.69	–1.38	–12
19R-3	640.52	70.7	578	100	21.9	26	802	538	0.98	253	5.67	3.19	0.47	NA	–1.56	–17
21R-3	659.10	26.2	1040	106	37.4	22	251	1080	1.02	162	5.09	1.78	1.24	0.45	–1.84	–11
23R-3	678.03	36.1	913	105	50.4	26	646	2040	1.02	215	5.16	0.47	1.94	0.73	–1.77	–15
24R-2	686.12	7.44	770	111	59.4	22	458	1630	1.16	897	6.04	1.13	4.82	0.28	–1.74	–14
27R-2	714.27	40.7	921	125	61.3	19	514	1380	1.03	168	5.92	0.79	1.29	NA	–1.60	–12
29R-2 (GRIND)	733.52	18.4	900	97.0	59.6	5.8	249	1180	1.01	321	6.94	0.94	1.01	NA	NA	NA
30R-2	743.07	39.5	1060	134	54.6	26	207	2190	1.16	140	5.65	0.78	0.78	0.58	–1.69	–9.9
32R-5	764.50	39.8	1070	134	33.0	14	419	2150	1.15	225	5.60	0.68	1.82	0.46	–1.71	–9.9
33R-2	771.20	34.3	1010	130	31.1	10	294	685	1.16	140	5.85	0.60	1.13	0.59	–1.75	–13
37R-2	807.12	21.9	887	134	40.6	39	1240	747	1.17	489	6.45	NA	2.83	NA	–1.89	–11
38R-3	818.03	21.1	927	141	92.1	17	148	1640	1.23	200	6.68	0.85	2.80	NA	–1.76	–14
40R-2	835.62	16.6	1010	140	7.47	16	818	2120	1.12	311	5.71	1.00	2.91	0.59	–1.60	–13
41R-3	846.53	16.4	999	148	93.4	14	600	1110	1.04	473	5.40	0.86	3.26	NA	–1.77	–14
43R-5	867.95	26.0	1290	139	32.7	11	128	880	0.90	139	4.03	0.64	1.45	0.38	–1.91	–12
46R-4	895.01	40.7	1230	136	57.0	10	256	1270	0.90	203	3.88	0.48	0.97	0.20	–2.03	–13
48R-5	915.45	38.8	1340	122	48.3	9.5	106	1090	0.90	317	3.73	0.36	1.15	0.11	–2.10	–14
49R-3	922.11	60.8	1150	114	40.1	18	1390	2320	0.87	478	4.34	0.81	8.22	0.21	–2.11	–16
51R-5	943.91	9.49	546	95.4	26.4	21	975	406	0.72	305	5.60	0.64	1.20	0.45	–2.11	–16
55R-2	977.70	2.81	539	76.3	21.4	38	5130	310	0.81	673	7.96	1.01	9.90	NA	–1.82	–12
56R-2	986.85	0.54	613	74.3	11.8	36	1920	702	0.77	435	7.19	0.93	8.07	0.34	–1.83	–13
59R-2	1011.12	0.68	405	76.5	17.0	33	4210	214	0.50	237	4.27	0.80	3.06	NA	–1.92	–13
61R-3	1021.53	11.7	359	65.8	19.1	5.4	2240	472	0.57	356	5.67	0.45	1.04	NA	–2.10	–12
62R-2	1024.21	1.11	379	79.7	20.2	18	2220	509	0.40	431	3.59	0.56	4.38	NA	NA	NA
64R-2	1043.20	17.6	805	67.8	13.6	15	698	523	0.79	832	5.72	0.64	2.75	0.17	–2.37	–12
315-C0002D-																
1H-2	1.52	1.76	639	90.2	0.45	28	325	154	1.48	84.7	3.53	1.65	8.99	0.61	–0.08	–2.4
1H-5	4.35	0.94	726	87.6	0.68	43	ND	51.3	1.39	32.6	3.60	ND	2.27	NA	–0.01	–3.9
2H-3	8.81	0.69	700	83.5	31.3	44	151	196	1.39	14.4	4.11	0.56	1.54	0.95	0.06	–5.2
2H-7	13.06	0.54	726	82.3	135	61	146	233	1.44	12.6	4.73	1.39	1.86	1.00	0.09	–4.3
3H-4	19.54	0.96	697	85.9	117	59	154	319	1.34	17.9	4.69	0.59	1.66	0.88	0.08	–2.0
4H-4	29.20	1.33	715	80.7	95.8	69	88.1	174	1.24	16.8	4.47	0.28	11.0	0.79	0.02	–0.7
5H-4	38.71	2.50	674	82.1	90.6	82	116	114	1.22	15.0	4.84	0.03	3.63	1.01	–0.09	–4.0
6H-5	49.43	3.29	737	82.6	87.2	65	5570	1620	1.19	21.5	4.89	3.97	2.42	0.64	–0.18	–1.3
7H-4	57.74	1.88	685	81.0	83.6	70	5700	2680	1.19	21.7	6.27	6.16	2.01	5.9	–0.23	–2.4
8H-4	66.92	2.22	717	81.6	75.7	38	3470	727	1.15	29.3	6.06	0.74	1.62	0.53	–0.40	–1.3
9H-5	78.10	1.67	668	78.4	64.2	53	1190	1450	1.19	40.9	7.61	0.68	3.35	0.30	–0.50	–2.2
10H-4	86.21	2.04	779	75.5	52.1	58	1580	1330	1.20	39.9	7.75	0.55	3.58	0.44	–0.55	–0.9
11H-5	96.72	2.49	830	74.4	39.9	39	3840	2290	1.09	33.7	7.16	1.61	3.82	0.70	–0.60	0.5
11H-6	98.06	1.90	802	72.7	38.4	37	2920	995	1.07	34.7	7.45	ND	2.60	NA	–0.54	–3.1
12H-5	106.41	7.80	827	74.6	30.0	35	2010	737	1.03	56.0	7.45	0.81	3.34	0.41	–0.64	–1.5
13H-5	115.81	1.94	589	71.2	20.5	46	1420	568	1.09	131	9.91	0.65	1.89	0.09	–0.70	–3.0
14H-3	121.92	10.5	411	56.4	10.8	38	285	665	0.79	2310	7.58	ND	2.31	NA	–0.23	1.0
14H-5	124.74	41.0	718	71.1	16.5	25	712	693	0.97	241	8.72	1.22	1.08	0.67	–0.78	–3.1
15X-5	133.18	48.6	828	70.7	13.4	28	2060	959	0.88	36.0	5.35	2.70	1.34	0.38	–0.75	–2.8
16H-6	157.09	29.9	728	66.2	10.9	47	664	1590	0.98	265	6.41	2.60	1.89	1.02	–0.87	–3.3
17X-4	159.77	0.71	178	10.7	1.61	70	1590	235	0.31	137	2.15	0.89	3.41	NA	0.90	7.2
18H-1	200.42	27.8	597	46.1	13.0	115	2480	386	0.64	1900	4.86	4.82	6.80	NA	–0.23	0.7
18H-2	200.60	18.3	833	66.7	20.2	38	1680	2450	0.81	277	4.93	12.3	4.72	1.40	–0.96	–3.7

Table T15. Headspace gas analysis, Holes C0002B and C0002D. (See table note.) (Continued on next page.)

Core, section, interval (cm)	Depth CSF (m)	Headspace gas (ppmv)			C_1/C_2
		Methane	Ethane	Propane	
315-C0002D-					
1H-1, 137–141	1.37	16.7	ND	ND	—
2H-1, 137–141	7.25	96.0	ND	ND	—
3H-1, 137–141	16.75	26,449.5	ND	ND	—
4H-1, 144.5–148.5	26.33	31,389.7	ND	ND	—
5H-1, 137–141	35.75	15,361.3	ND	ND	—
6H-1, 137–140.5	45.25	11,540.6	ND	ND	—
7H-1, 137–141	54.75	6541.5	ND	ND	—
8H-1, 137–141	64.25	14,682.7	ND	ND	—
9H-1, 137–140.5	73.75	8,264.3	ND	ND	—
10H-1, 137–140.5	83.25	8,932.2	ND	ND	—
11H-1, 136.5–140.5	92.75	7,220.4	ND	ND	—
12H-1, 136.3–140.3	102.24	8,608.3	ND	ND	—
13H-3, 132.7–136.7	114.45	9,022.6	ND	ND	—
14H-1, 134.5–138.5	121.23	7,342.2	ND	ND	—
15X-1, 120.5–124.5	130.36	5,253.6	ND	ND	—
16H-1, 136.5–140.5	151.37	2,790.8	ND	ND	—
17X-1, 43–47	159.40	10,466.4	ND	ND	—
315-C0002B-					
1R-1, 137.5–141.5	476.38	5,704.1	4.6	ND	1,238
2R-1, 139–143	485.89	3,094.3	4.2	ND	730
3R-1, 119–123	495.19	4,644.2	5.0	ND	936
4R-1, 105.5–109.5	504.56	4,476.3	5.8	ND	776
5R-1, 74.5–78.5	508.75	3,992.8	5.1	ND	778
8R-1, 137–141	534.37	6,091.3	5.8	ND	1,049
9R-1, 136–140	543.86	2,643.5	3.3	ND	802
10R-1, 136.5–140.5	553.37	4,439.8	5.7	ND	783
11R-1, 137–141	562.87	3,166.0	4.7	ND	679
12R-1, 137–141	572.37	2,441.2	2.8	ND	886
13R-1, 137–141	581.87	3,014.6	5.2	ND	585
14R-1, 137–141	591.37	3,446.3	7.1	ND	484
15R-1, 137–141	600.87	4,258.4	5.3	ND	799
16R-1, 137–141	610.37	3,015.1	5.6	ND	540
17R-1, 137.5–141.5	619.88	13,139.3	9.4	ND	1,402
18R-1, 73.5–77.5	628.74	14,752.1	8.7	ND	1,703
19R-1, 137–140.5	638.87	10,677.0	6.1	ND	1,745
20R-3, 137–141	651.20	17,487.6	11.0	ND	1,593
21R-1, 136.5–140.5	657.87	10,810.1	11.1	ND	970
23R-1, 137–141	676.37	3,245.7	6.4	ND	507
24R-1, 137–141	685.87	3,665.4	5.1	ND	718
25R-1, 137–141	695.37	9,848.8	5.3	ND	1,868
26R-1, 125–130	704.75	702.3	3.5	ND	204
27R-1, 105.5–109.5	714.06	12,825.2	12.4	ND	1,030
28R-1, 136.5–140.5	723.87	13,434.5	7.8	ND	1,730
29R-1, 137–141	733.37	17,545.6	12.6	ND	1,396
30R-1, 137–141	742.87	14,525.4	9.8	ND	1,487
31R-1, 137–141	752.37	12,790.8	12.6	ND	1,018
32R-1, 136.7–140.7	761.87	7,894.8	13.8	ND	573
33R-1, 95–99	770.95	19,260.8	20.1	ND	959
36R-1, 136–140	797.36	24,361.6	14.4	ND	1,692
37R-1, 137–141	806.87	1,203.4	2.2	ND	550
38R-1, 137–141	816.37	6,406.9	9.0	ND	710
39R-1, 136–140	825.86	4,238.7	12.4	ND	341
40R-1, 137–141	835.37	10,364.5	15.5	ND	668
41R-1, 137–141	844.87	22,175.6	15.0	ND	1,479
42R-1, 137.5–141.5	854.38	22,533.1	17.3	ND	1,304
43R-1, 137–141	863.87	20,799.8	16.8	ND	1,238
44R-1, 137–141	873.37	15,165.6	12.7	ND	1,196
45R-1, 137–141	882.87	14,803.2	13.0	ND	1,137
46R-1, 136.5–140.5	892.37	15,898.7	17.2	ND	923
47R-1, 137–141	901.87	17,044.1	15.5	ND	1,099
48R-1, 136.5–140.5	911.37	11,065.2	15.0	ND	735
49R-1, 137–141	920.87	31,308.4	36.1	ND	868
51R-1, 135.5–139.5	939.86	4,431.4	26.2	ND	169
52R-1, 99–103	948.99	4,228.9	10.2	ND	415
55R-1, 94.5–98.5	977.45	3,157.0	10.2	ND	311
56R-1, 60–64	986.60	2,145.0	8.3	ND	260
58R-1, 137–141	1006.37	6,669.8	28.9	ND	230

Table T15 (continued).

Core, section, interval (cm)	Depth CSF (m)	Headspace gas (ppmv)			C_1/C_2
		Methane	Ethane	Propane	
59R-1, 137–141	1010.87	8,824.7	44.8	ND	197
60R-1, 137–141	1015.37	10,576.1	33.7	ND	313
61R-1, 136.5–140.5	1019.87	9,130.7	32.6	ND	280
62R-1, 96–100	1023.96	7,085.2	37.6	9.1	188
63R-1, 137–141	1033.87	6,800.0	38.6	11.1	176
64R-1, 95.5–99.5	1042.96	39,006.7	95.0	19.1	411
65R-1, 138–142	1047.88	38,058.1	84.5	16.2	451

Note: ND = none detected, — = not applicable.

Table T16. Carbon, nitrogen, and sulfur, Hole C0002B. (See table notes.) (Continued on next page.)

Core, section, interval (cm)	Depth CSF (m)	Carbon (wt%)				TN (wt%)	TS (wt%)	C/N
		Total	Inorganic	$CaCO_3$	Organic			
315-C0002B-								
1R-2, 0–1	476.42	1.44	0.83	6.93	0.61	0.10	0.07	5.90
4R-1, 84–85	504.35	1.06	0.55	4.62	0.51	0.09	0.12	5.42
4R-2, 0–1	504.60	0.99	0.51	4.22	0.49	0.09	0.09	5.22
8R-2, 0–1	534.42	1.41	0.72	5.99	0.69	0.11	0.09	6.05
8R-3, 73–74	535.46	1.18	0.57	4.76	0.61	0.11	0.09	5.74
9R-3, 0–1	545.00	1.31	0.64	5.29	0.67	0.13	0.09	5.13
9R-4, 123–124	546.54	1.18	0.57	4.78	0.61	0.12	0.08	4.93
10R-2, 0–1	553.41	1.09	0.49	4.12	0.60	0.13	0.03	4.67
10R-3, 23–24	553.96	1.24	0.55	4.60	0.68	0.11	0.10	5.98
11R-3, 0–1	564.32	1.51	0.76	6.35	0.75	0.13	0.15	5.88
11R-4, 84–85	565.48	1.53	0.75	6.26	0.78	0.11	0.12	7.10
12R-2, 65–66	573.07	1.31	0.65	5.41	0.66	0.10	0.17	6.44
13R-2, 0–1	581.92	1.20	0.63	5.23	0.57	0.12	0.04	4.92
13R-3, 24–25	582.48	1.12	0.56	4.66	0.56	0.10	0.16	5.40
15R-3, 32–33	602.65	0.59	0.24	2.04	0.35	0.08	0.34	4.44
16R-3, 0–1	611.41	1.22	0.63	5.27	0.59	0.11	0.21	5.17
16R-4, 9–10	611.91	1.13	0.57	4.72	0.57	0.10	0.09	5.62
16R-4, 127–128	613.09	1.33	0.68	5.65	0.66	0.12	0.16	5.69
17R-4, 27–28	623.00	1.22	0.53	4.45	0.69	0.12	0.08	5.89
19R-2, 127–128	640.18	1.02	0.55	4.61	0.47	0.09	0.07	4.94
19R-3, 0–1	640.32	0.77	0.32	2.68	0.45	0.10	0.09	4.46
19R-4, 87–88	641.60	0.46	0.26	2.17	0.20	0.08	0.12	2.38
20R-2, 125–126	649.67	1.46	0.92	7.68	0.54	0.11	0.08	4.98
20R-3, 57–58	650.40	1.36	0.94	7.84	0.42	0.09	0.45	4.57
21R-2, 43–44	658.34	1.87	1.22	10.17	0.65	0.11	0.08	5.76
21R-3, 0–1	658.90	1.38	0.82	6.80	0.56	0.09	0.18	6.28
21R-4, 28–29	659.60	1.77	1.33	11.10	0.44	0.09	0.43	5.00
23R-2, 66–67	677.08	1.26	0.71	5.95	0.54	0.10	0.12	5.56
23R-3, 0–1	677.83	0.61	0.28	2.32	0.33	0.08	0.01	3.98
24R-2, 0–1	685.92	1.37	0.91	7.60	0.46	0.09	0.12	5.24
24R-3, 71–72	687.05	1.19	0.72	6.03	0.46	0.08	0.17	5.45
27R-2, 0–1	714.12	1.23	0.68	5.68	0.54	0.09	0.15	5.98
28R-2, 30–31	724.21	0.47	0.09	0.79	0.37	0.08	0.01	4.76
29R-2, 0–2	733.42	0.79	0.51	4.29	0.28	0.07	0.02	3.81
30R-1, 124–125	742.75	0.95	0.53	4.46	0.41	0.09	0.15	4.76
30R-2, 0–1	742.92	1.23	0.73	6.10	0.50	0.10	0.04	5.11
31R-1, 127–128	752.28	1.26	0.87	7.26	0.39	0.09	0.00	4.23
32R-2, 67–68	762.58	1.50	0.58	4.84	0.92	0.12	0.21	7.67
32R-2, 89–90	762.80	1.54	0.77	6.45	0.76	0.09	0.10	8.04
32R-5, 0–2	764.30	1.30	0.51	4.24	0.79	0.10	0.13	8.18
33R-1, 85–86	770.86	1.23	0.45	3.75	0.78	0.09	0.22	8.77
33R-2, 40–41	771.40	1.46	0.65	5.41	0.81	0.10	0.20	7.75
37R-2, 0–1	806.92	1.12	0.64	5.37	0.48	0.09	0.16	5.45
38R-3, 0–1	817.83	1.23	0.60	5.01	0.63	0.08	0.08	8.01
38R-4, 13–14	818.37	1.38	0.71	5.91	0.67	0.10	0.17	6.71
40R-2, 0–1	835.42	1.73	0.87	7.24	0.86	0.10	0.10	8.91
40R-3, 98–99	836.81	1.81	1.21	10.11	0.60	0.11	0.11	5.67
41R-3, 40–41	846.73	0.93	0.48	4.00	0.45	0.07	0.18	6.41
41R-4, 8–9	846.83	1.78	1.44	12.02	0.33	0.07	0.34	4.85
42R-1, 16–17	853.17	1.69	1.25	10.46	0.43	0.07	0.17	6.51

Table T16 (continued).

Core, section, interval (cm)	Depth CSF (m)	Carbon (wt%)				TN (wt%)	TS (wt%)	C/N
		Total	Inorganic	$CaCO_3$	Organic			
42R-1, 31–32	853.32	0.82	0.58	4.83	0.24	0.08	0.60	2.97
43R-1, 17–18	862.68	2.69	2.28	18.97	0.42	0.10	0.13	4.34
43R-1, 40–41	862.91	2.90	2.52	21.00	0.38	0.07	1.51	5.64
43R-5, 40–41	868.15	3.00	2.32	19.37	0.68	0.10	0.43	6.49
44R-1, 124–125	873.25	1.26	1.03	8.61	0.22	0.05	1.03	4.95
44R-2, 48–49	873.90	2.91	2.54	21.17	0.37	0.06	0.26	6.17
44R-4, 125–126	877.48	2.19	1.90	15.80	0.29	0.06	0.35	4.93
45R-1, 44–45	881.95	2.92	2.57	21.45	0.34	0.07	0.17	4.87
46R-3, 8–9	893.91	3.13	2.72	22.69	0.41	0.07	0.26	5.58
46R-4, 0–1	894.81	2.48	2.01	16.74	0.47	0.09	0.29	5.09
46R-5, 94–95	896.17	1.67	1.37	11.38	0.30	0.07	0.61	4.13
47R-1, 37–38	900.88	2.45	2.03	16.92	0.42	0.08	0.23	5.54
47R-1, 61–62	901.12	1.45	1.18	9.85	0.27	0.07	0.21	3.73
47R-3, 38–39	903.71	3.22	2.76	22.98	0.46	0.08	0.13	5.76
48R-2, 35–36	911.76	2.29	1.70	14.20	0.59	0.09	1.13	6.72
48R-5, 0–1	915.25	2.20	1.51	12.60	0.69	0.10	0.68	7.05
48R-6, 65–66	916.31	1.64	1.04	8.66	0.60	0.11	0.49	5.67
48R-6, 89–90	916.55	2.84	2.27	18.87	0.57	0.09	0.29	6.22
49R-1, 96–97	920.47	2.31	1.63	13.62	0.68	0.11	0.60	6.35
49R-1, 121–122	920.72	2.09	1.46	12.17	0.63	0.11	0.68	5.86
49R-3, 0–1	921.91	1.85	1.22	10.13	0.63	0.10	0.87	6.59
51R-1, 34–35	938.85	0.97	0.36	2.97	0.61	0.10	1.11	6.37
51R-5, 0–1	943.71	0.51	0.21	1.76	0.30	0.08	1.08	3.92
51R-6, 26–27	944.39	1.15	0.61	5.09	0.54	0.10	0.63	5.37
51R-6, 51–52	944.64	0.90	0.45	3.79	0.44	0.09	1.80	4.76
58R-1, 46–47	1005.47	0.67	0.21	1.74	0.46	0.09	1.62	4.93
59R-1, 121–122	1010.72	0.76	0.08	0.66	0.69	0.09	0.54	7.48
59R-2, 0–1	1010.92	0.79	0.35	2.92	0.44	0.08	0.90	5.21
59R-3, 23–24	1011.56	0.85	0.22	1.85	0.63	0.08	1.58	7.52
60R-1, 69–70	1014.70	0.82	0.34	2.82	0.48	0.07	1.53	6.81
61R-2, 121–122	1021.12	0.37	0.12	1.04	0.24	0.08	0.95	2.99
61R-3, 0–1	1021.33	0.66	0.28	2.30	0.38	0.08	1.51	4.85
61R-4, 22–23	1021.96	0.86	0.35	2.88	0.51	0.10	0.69	5.24
62R-1, 50–51	1023.51	0.62	0.30	2.50	0.32	0.07	1.21	4.42
62R-2, 0–1	1024.01	0.57	0.25	2.05	0.32	0.09	0.33	3.45
63R-1, 120–121	1033.71	0.77	0.30	2.53	0.47	0.11	0.94	4.24
64R-1, 39–40	1042.40	0.87	0.44	3.63	0.43	0.09	1.21	4.63
64R-2, 0–1	1043.00	0.74	0.36	2.96	0.39	0.07	0.99	5.40
65R-1, 105–106	1047.56	0.81	0.36	2.97	0.45	0.09	0.56	5.06
65R-2, 125–126	1049.18	0.84	0.34	2.84	0.50	0.11	0.50	4.39

Notes: CSF = core depth below seafloor. TN = total nitrogen, TS = total sulfur, C/N = carbon to nitrogen ratio.

Table T17. Whole-round core sections, Site C0002. (See table notes.)

WRC type	Core, section	Depth CSF (m)	Sampling method
	315-C0002D-		
A	1H-3	2.00	Syringe
A	1H-5	4.83	Syringe
A	2H-4	9.30	Syringe
A	2H-8	13.54	Syringe
A	3H-5	20.33	Syringe
A	5H-5	39.75	Syringe
A	7H-5	57.98	Syringe
A	9H-6	78.92	Syringe
A	11H-4	95.94	Syringe
A	13H-6	116.98	Syringe
A	14H-1	120.26	Syringe
A	16H-4	155.50	Syringe
A	18H-4	203.10	Syringe
	315-C0002B-		
A	11R-4	565.65	Intact piece
A	17R-2	620.86	Intact piece
A	21R-1	657.53	Intact piece
A	32R-1	760.84	Intact piece
A	38R-2	817.54	Intact piece
A	43R-3	866.23	Intact piece
A	48R-2	911.68	Intact piece
A	51R-1	939.09	Intact piece
A	61R-1	1019.73	Intact piece
	315-C0002D-		
B	1H-3	1.88	Syringe
B	1H-6	4.71	Syringe
B	2H-4	9.17	Syringe
B	2H-8	13.42	Syringe
B	3H-5	20.21	Syringe
B	4H-5	29.96	Syringe
B	6H-6	50.14	Syringe
B	8H-3	66.61	Syringe
B	10H-6	88.71	Syringe
B	12H-2	102.53	Syringe
B	13H-6	117.11	Syringe
B	14H-1	120.13	Syringe
B	16H-4	155.38	Syringe
B	18H-4	202.69	Syringe
	315-C0002B-		
B	11R-2	564.26	Intact piece
B	21R-1	657.65	Intact piece
B	32R-1	761.17	Intact piece
B	43R-3	866.36	Intact piece
B	61R-1	1019.85	Intact piece
	315-C0002D-		
C	1H-3	1.73	Syringe
C	1H-6	4.56	Syringe
C	2H-4	9.02	Syringe
C	2H-8	13.27	Syringe
C	3H-5	20.06	Syringe
C	4H-5	29.81	Syringe
C	6H-6	49.99	Syringe
C	8H-3	66.46	Syringe
C	10H-6	88.56	Syringe
C	12H-2	102.38	Syringe
C	13H-6	117.26	Syringe
C	14H-1	119.98	Syringe
C	16H-4	155.23	Syringe
C	18H-4	202.54	Syringe
	315-C0002B-		
C	11R-2	563.95	Intact piece
C	17R-2	620.90	Intact piece
C	21R-1	657.55	Intact piece
C	32R-1	760.86	Intact piece
C	38R-2	817.56	Intact piece
C	43R-3	866.26	Intact piece
C	48R-2	911.71	Intact piece
C	61R-4	1022.98	Intact piece

Notes: CSF = core depth below seafloor. WRC = whole-round core. WRC type: A = subsampled on board for cell fixing, DNA and RNA extraction, and cultivation studies; B = stored at +4°C for cultivation experiments to be conducted on shore; C = subsampled on board for cell fixing and thereafter stored at –80°C for molecular analysis.

Table T18. Cell abundance in sediments, Site C0002. (See table note.)

Core, section, interval (cm)	Sample depth CSF (m)	Cell abundance (cells/cm^3)
315-C0002D-		
1H-3, 0.30–0.45	2.00	3.4E+09
1H-6, 0.30–0.46	4.83	1.2E+09
2H-4, 0.30–0.47	9.30	1.5E+09
2H-8, 0.30–0.48	13.54	1.5E+09
3H-5, 0.61–0.76	20.33	1.3E+09
5H-5, 0.85–1.00	39.75	1.5E+09
7H-5, 0.06–0.21	57.98	1.1E+09
9H-6, 0.64–0.79	78.92	1.9E+07
11H-4, 0.46–0.61	95.94	2.2E+07
13H-6, 1.00–1.15	116.98	1.5E+07
14H-1, 0.30–0.45	120.26	1.1E+07
16H-4, 1.22–1.37	155.50	5.6E+07
18H-4, 0.99–1.14	203.10	1.0E+09
315-C0002B-		
11R-4, 0.94–1.09	565.65	6.5E+08
17R-2, 0.90–0.99	620.86	1.8E+07
21R-1, 0.95–1.10	657.53	4.0E+07
32R-1, 0.26–0.41	760.84	2.4E+07
38R-2, 1.05–1.20	817.54	1.5E+07
43R-3, 0.82–0.97	866.23	2.4E+07
48R-2, 0.20–0.35	911.68	4.5E+07
51R-1, 0.51–0.66	939.09	9.9E+06
61R-1, 1.15–1.30	1019.73	4.8E+08

Note: CSF = core depth below seafloor.

Table T19. APCT3 temperature measurements, Hole C0002D. (See table notes.)

Core	Depth CSF (m)	Temperature (°C)	RMS misfit (°C)
315-C0002D-			
2H	15.38	2.670	3.00E–02
4H	34.38	3.671	3.00E–03
6H	53.38	4.541	3.00E–03
8H	72.38	5.241	2.00E–03
12H	110.38	6.934	1.70E–02
16H	158.97	8.450	1.10E–02

Notes: APCT3 = advanced piston corer temperature tool. CSF = core depth below seafloor, RMS = root mean square.

Table T20. Core-log depth correlation, Holes C0002A and C0002B. (See table note.)

Core depth CSF (m)	Logging depth LSF (m)	Depth shift (m)
315-C0002B	314-C0002A	
475	484.5	9.5
535.56	547.57	12.01
592.55	607.16	14.61
615	628.34	13.34
640	652	12
772.87	781.81	8.94
825.93	831	5.07
848.146	858.16	10.014
853.16	862.88	9.72
858.53	868.68	10.15
862.82	871.58	8.76
878.862	891.84	12.978
885.642	900.5	14.858
901.46	914.1	12.64
906.712	920.496	13.784
913.36	925.37	12.01
923.5	934.7	11.2
942.5	956	13.5
1012	980	–32
1025.9	990.9	–35
1036.2	998.5	–37.7
1044.24	1008.58	–35.66
1052.5	1015	–37.5

Note: CSF = core depth below seafloor, LSF = logging-while-drilling depth below seafloor.